Railway track support condition assessment: from onboard measurement to maintenance decision support

Unsiwilai, S.

DOI
10.4233/uuid:9c4e228d-d15d-4583-a594-b91e3efade68

Publication date
2024

Document Version
Final published version

Citation (APA)
Unsiwilai, S. (2024). *Railway track support condition assessment: from onboard measurement to maintenance decision support* . [Dissertation (TU Delft), Delft University of Technology]. https://doi.org/10.4233/uuid:9c4e228d-d15d-4583-a594-b91e3efade68

Important note
To cite this publication, please use the final published version (if applicable).
Please check the document version above.

RAILWAY TRACK SUPPORT CONDITION ASSESSMENT

FROM ONBOARD MEASUREMENT TO MAINTENANCE DECISION SUPPORT

RAILWAY TRACK SUPPORT CONDITION ASSESSMENT

FROM ONBOARD MEASUREMENT TO MAINTENANCE DECISION SUPPORT

Dissertation

for the purpose of obtaining the degree of doctor
at Delft University of Technology
by the authority of the Rector Magnificus prof. dr. ir. T.H.J.J. van der Hagen
chair of the Board for Doctorates
to be defended publicly on
Monday 25 November 2024 at 15:00 o'clock

by

Siwarak UNSIWILAI

Master of Engineering in Civil Engineering
Chulalongkorn University, Thailand
Born in Khon Kaen, Thailand

This dissertation has been approved by the promotors.

Composition of the doctoral committee:

Rector Magnificus	chairperson
Prof. dr. Z. Li	Delft University of Technology, promotor
Dr. A.A. Núñez Vicencio	Delft University of Technology, copromotor

Independent members:

Prof. dr. ir. R.P.B.J. Dollevoet	Delft University of Technology
Prof. dr. ir. B.H.K. De Schutter	Delft University of Technology
Prof. dr. D. Sáez Hueichapan	Universidad de Chile, Chile
Prof. dr. I. Škrjanc	University of Ljubljana, Slovenia
Dr. ir. A. Zoeteman	ProRail

CONTENTS

SUMMARY

The railway track is the most critical element that infrastructure managers have to ensure satisfactory health conditions to provide safe, sustainable, and adequate service quality. The condition of railway tracks is managed through maintenance strategies that benefit enormously from the availability of accurate and updated information from measurement devices. This thesis focuses on estimating the track support condition using Axle Box Acceleration (ABA) measurements. The ABA characteristics under different track support conditions are evaluated, effects of influential parameters in the measurements are analyzed, key performance indicators (KPIs) for condition monitoring of ballast and substructure layers are proposed, and results with traditional techniques such as impact tests are compared. Finally, an enhanced track quality index is proposed to improve the effectiveness of maintenance decision-making. Case studies in The Netherlands, Sweden, and Norway are considered. The dissertation is divided into five chapters, as follows.

Chapter 1 discusses the need for efficient maintenance planning for the ballasted track. Maintenance decision-making benefits from updated information on the condition of the tracks, which can be efficiently obtained from onboard measurements. Current standard methods based on track geometry measurement provide results for track condition assessment; however, its effectiveness in indicating locations with poor train-track interaction is limited. This motivates this thesis to investigate how to extract the knowledge from ABA measurements and embed it into decision-making support tools for ballast and substructure condition assessment.

In Chapter 2, characteristics of ABA signals with respect to changes in the substructure conditions are analyzed. ABA signals measured at railway bridge transition zones are considered since drastic changes in track support conditions occur at these locations. The analysis of ABA signals corresponding to long wavelength track irregularities between 3 to 25 meters is conducted. The repeatability and consistency of the responses in the analyzed wavelengths, which are found in various analyzed transition zones, suggest the potential to

utilize ABA signals for assessing track support conditions. Then, a framework for designing KPIs based on ABA signals is proposed for track support condition assessment at railway bridge transition zones. Four KPIs are established to quantify local ABA energy differences at various locations of the transition zones, including abutments, tracks, entrance and exit sides, and inner and outer rails. In the evaluated case study, KPIs suggest that the locations with the highest degradation do not always occur at a specific abutment, track (inbound or outbound), side (entrance or exit), or rail (inner or outer). Further, we report locations where track geometry did not show drastic variations while ABA indicated stronger responses, which motivates further analysis of the interpretability of these ABA responses (Chapter 3) and creating a new track quality index (Chapter 4).

Chapter 3 presents an investigation into track vertical dynamics at transition zones, aiming to find additional support for the physical interpretation of ABA measurements using hammer and falling weight impact tests. Correlations between the impact tests and ABA measurements are analyzed in the frequency range related to track support conditions. Hammer tests provide information on two resonances related to the condition of the ballast layer (full track resonance, FT) and the components above it, while falling weight tests provide FT and one additional resonance lower than FT. The operating deflection shape (ODS) analysis from falling weight tests indicates a highly deflected zone at the same location indicated by ABA responses. From the analysis, ABA responses in the spatial frequency range of 1.05 m^{-1} to 2.86 m^{-1} are related to the FT resonance features, indicating a relationship with the ballast layer condition.

Chapter 4 presents a framework for designing an enhanced vertical track quality index, called EnVTQI, by integrating features from track longitudinal levels, a conventional track quality index (TQI), and dynamic responses from ABA measurements to represent train-track interaction. ABA signals in two wavelength ranges, 3 m - 25 m (the substructure layer related) and 0.4 m - 0.8 m (the ballast layer related), are considered. The performance of EnVTQI is evaluated under different measurement conditions. In the evaluated case study, high-energy ABA responses are found in locations with low variation in longitudinal levels, showing the capability of EnVTQI in distinguishing track segments that cause poor train-track interaction. In addition, the framework allows users in the railway industry to tune

parameters to be matched with specific use cases, particularly to highlight the locations where conventional TQI does not indicate track quality problems.

This thesis is concluded in Chapter 5. ABA measurements can be utilized to enhance track support condition assessment, which can support infrastructure managers in planning maintenance activities. The thesis provides analysis and experimental evidence that can help standardize ABA measurements to support maintenance decision-making in railway networks worldwide. Further research is recommended to understand the characteristics of ABA signals under different sources of uncertainties and variations due to load and speed and to further develop advanced physical models that capture the track dynamics in the lowest frequency range.

SAMENVATTING

De spoorbaan is het meest cruciale onderdeel van de railinfrastructuur waarvan de verantwoordelijke infrabeheerders een afdoende conditie moeten garanderen om zo veilig, duurzaam en adequaat railvervoer te kunnen bieden. Bij de uitvoering van onderhoudsstrategieën van spoorlijnen worden nauwkeurige en actuele gegevens uit meet- en registratiesystemen zoveel mogelijk benut. Dit proefschrift betreft de bepaling van de conditie van de dragende delen van het spoor met behulp van aspotversnellingen of Axle Box Acceleration (ABA) metingen. De ABA-gegevens met specifieke kenmerken van deze dragende delen worden geëvalueerd en de effecten van bepalende parameters in de metingen worden geanalyseerd. Tevens worden key performance indicators (KPI's) voorgesteld voor conditiemonitoring van ballastlagen en andere delen van de onderbouw van spoorbanen en vindt vergelijking plaats van ABA-resultaten met traditionele technieken zoals impacttesten. Ten slotte wordt een verbeterde spoorkwaliteitsindex voorgesteld om de doeltreffendheid van besluitvorming over onderhoud van het spoor te verbeteren. Hierbij worden casestudies in Nederland, Zweden en Noorwegen in beschouwing genomen. Het proefschrift is in vijf hoofdstukken verdeeld:

Hoofdstuk 1 gaat in op de noodzaak van een efficiënte onderhoudsplanning voor ballastspoor. Bij de besluitvorming over onderhoud wordt gebruik gemaakt van actuele informatie over de conditie van spoorbanen, die efficiënt kan worden verkregen uit metingen vanuit treinen. De huidige standaardmethoden, gebaseerd op bepaling van de spoorgeometrie, leiden tot resultaten voor de beoordeling van de conditie van het spoor. De doeltreffendheid ervan bij het signaleren van locaties met een slechte interactie tussen trein en spoorbaan is echter beperkt. Dit is een drijfveer voor dit proefschrift om te onderzoeken hoe de betreffende kennis uit ABA-registraties kan worden geëxtraheerd en kan worden ingebed in systemen en processen voor de ondersteuning van besluitvorming bij de beoordeling van de conditie van ballast en de rest van de onderbouw van spoorlijnen.

In Hoofdstuk 2 worden eigenschappen van ABA-signalen met betrekking tot veranderingen in de omstandigheden van de onderbouw geanalyseerd. ABA-signalen vastgelegd bij overgangszones van spoorbruggen (transitiezones) worden nader beschouwd, aangezien op deze locaties drastische veranderingen in de ondersteuning van spoorbanen optreden. ABA-signalen met een lange golflengte tussen 3 en 25 meter die overeenkomen met oneffenheden in de onderbouw worden geanalyseerd. Het herhaalpatroon en de consistentie van de responses in de geanalyseerde golflengten, die worden aangetroffen in verschillende geanalyseerde transitiezones, zijn een stimulans om de potentie van ABA-data in te zetten voor de beoordeling van de conditie van spoorbanen met de dragende delen. Vervolgens wordt een raamwerk voorgesteld voor de definitie van KPI's op basis van ABA-data voor de beoordeling van de conditie van de spoorbaan in transitiezones bij spoorbruggen. Hierbij zijn vier KPI's vastgesteld om lokale ABA-energieverschillen te kwantificeren op verschillende locaties van de transitiezones, waaronder landhoofden, de spoorbaan, op- en afritten en de binnen- en buitenrails. In de uitgevoerde casestudy geven KPI's aan dat de locaties met de hoogste degradatie niet altijd voorkomen op een specifiek landhoofd, rijrichting (afgaand en opgaand), zijkant (op- en afrit) of spoor (binnen- of buitenzijde). Verder worden locaties beschreven waar de spoorgeometrie geen drastische variaties vertoonde, terwijl ABA-registraties sterke responses lieten zien, wat aanleiding geeft tot verdere analyse van de interpreteerbaarheid van de betreffende ABA-responsies (hoofdstuk 3) en het creëren van een nieuwe spoorkwaliteitsindex (hoofdstuk 4).

Hoofdstuk 3 beschrijft onderzoek naar de verticale dynamica van spoorbanen in overgangszones, met als doel extra aanknopingspunten te vinden voor de fysieke interpretatie van ABA-metingen aan de hand van uitkomsten van hamertesten en impacttest met valgewichten. Correlaties tussen de resultaten van de testen en ABA-metingen worden geanalyseerd in het frequentiebereik dat gerelateerd is aan de conditie van de dragende delen van spoorbanen. De hamertesten geven informatie over twee resonanties die verband houden met de toestand van de ballastlaag (volledige spoorresonantie of full track resonances, FT) en de componenten erboven, terwijl de impacttesten met valgewichten FT opleveren en één extra resonantie lager dan FT. De analyse van de operation deflction shape (ODS) van vallende gewichtstests geeft op dezelfde locatie die wordt aangegeven door

ABA-reacties een sterk afgebogen zone aan. Uit de analyse blijkt dat ABA-responsen in het ruimtelijke frequentiebereik van 1,05 m^{-1} tot 2,86 m^{-1} gerelateerd zijn aan de FT-resonantiekenmerken, wat een relatie aangeeft met de conditie van de ballastlaag.

Hoofdstuk 4 beschrijft een raamwerk voor de ontwikkeling van een verbeterde verticale spoorkwaliteitsindex of enhanced vertical track quality index (EnVTQI). Dit door kenmerken van longitudinale spoorbaanniveaus, een conventionele spoorkwaliteitsindex (Track Quality Index of TQI) en dynamische reacties van ABA-metingen samen te voegen om zo de interactie tussen trein en spoor weer te geven. Hierbij worden ABA-signalen in twee golflengtebereiken, 3 m - 25 m (gerelateerd aan de onderbouwlaag) en 0,4 m - 0,8 m (gerelateerd aan de ballastlaag) in beschouwing genomen. De prestaties van EnVTQI worden geëvalueerd onder verschillende omstandigheden van registratie. In de betreffende casestudy worden hoogenergetische ABA-reacties aangetroffen op locaties met weinig variatie in longitudinale niveaus, wat het vermogen van EnVTQI aantoont bij het onderscheiden van spoorsegmenten die een slechte interactie tussen trein en spoor veroorzaken. Bovendien stelt het raamwerk gebruikers in de railsector in staat parameters af te stemmen op specifieke use cases om zo vooral locaties te signaleren waar de conventionele TQI geen problemen met de spoorkwaliteit aangeeft.

Dit proefschrift wordt afgesloten met hoofdstuk 5 waarin wordt aangegeven dat ABA-registraties kunnen worden toegepast voor de verbetering van de beoordeling van conditie van de dragend delen van spoorlijnen, hetgeen railinfrastructuurbeheerders kan helpen bij het plannen van onderhoud. Het proefschrift levert met analyses en experimenteel onderzoek bewijsmateriaal aan dat kan helpen bij het standaardiseren van ABA-metingen ter ondersteuning van de besluitvorming over onderhoud in spoorwegnetwerken wereldwijd. Verder onderzoek wordt aanbevolen om de kenmerken van ABA-signalen onder verschillende oorzaken van onzekerheden en variaties als gevolg van belasting en snelheid beter te begrijpen om zo geavanceerde fysieke modellen verder te ontwikkelen voor de beschrijving van de spoorbaandynamica in het laagste frequentiebereik.

ABBREVIATIONS

ABA	Axle box acceleration
AUC	Area under the curve
BBMS	Dutch railway infrastructure monitoring system (from Dutch name Branche Breed Monitoring Systeem)
CoSD	Combined standard deviation
CWT	Continuous wavelet transform
EN	European standard (from the German name Europäische Norm)
EnVTQI	Enhanced vertical track quality index
FRF	Frequency response function
FT	Full track resonance
FWD	Falling weight deflectometer
GPS	Global positioning system
GWPS	Global wavelet power spectrum
IRJ	Insulated rail joint
KPI	Key performance indicator
LL	Longitudinal level
ODS	Operating deflection shape
SAWP	Scale average wavelet power
SD	Standard deviation
TQI	Track quality index
TR	Track resonance
VAL	Vibration acceleration level
WPS	Wavelet power spectrum

1

INTRODUCTION

1

1.1. BACKGROUND

1.1.1. IMPORTANCE OF TRACK MAINTENANCE PLANNING

Railway is an essential mode of transportation that can be considered a core of sustainable transportation because, among other benefits, it provides low CO_2 emissions and effectiveness in energy consumption [1–3]. However, due to time, weather and the use, the degradation of the track infrastructure threatens the normal operation of railway services. Controlling track defects to avoid failures is a complex task that railway infrastructure managers perform. As the railway infrastructure is a complex system with multiple sources of uncertainties, there is a need for effective and systematic approaches that facilitate tasks such as maintenance decision-making.

Railway infrastructure asset management, as defined by the International Union of Railways (UIC), is a framework that aims to optimize performance, mitigate risks, and control expenditure on assets to achieve business objectives while minimizing life cycle costs [4]. The effective allocation of limited resources is one of the major challenges. In the Netherlands, approximately 48% of the operational expenditure by ProRail, the Dutch infrastructure manager, accounts for maintenance operations. In addition, railway tracks are one of the most concerning assets since it has been reported that track failures are the majority of asset failures in the Dutch railway network, which accounts for approximately 40% of total asset failures in 2021 [5].

Ballasted track is a type of railway track structure extensively utilized worldwide. For example, the Dutch railway network consists of approximately 7,000 kilometers of track, most of which is ballasted [6]. The primary factors contributing to the widespread appeal of ballasted tracks include their simple design and construction processes, cost-effectiveness, and simplicity in maintenance. However, a ballasted track has a notable drawback in that it needs more inspections and more frequent maintenance activities in comparison to a ballastless track [7].

Maintenance strategies can be classified into two main types, according to the European Standard EN 13306:2019 [8]. The first type is corrective maintenance, in which maintenance activities are carried out after track defects have been found or safety limits

have been reached. For example, maintenance activities or speed regulations must be immediately implemented when track geometry parameters exceed the immediate action limit. For a track with a maximum operation speed of 160 km/h, the immediate action limit of the track longitudinal level is about ± 23 mm, corresponding to track irregularities in the wavelength between 3 m to 25 m [9].

The second type is preventive maintenance, in which maintenance activities are carried out in advance regarding desired criteria to prevent track failure. For example, ballast tamping is typically performed when the track usage reaches 40 – 70 mega gross tonnage (MGT) of cumulative load passing [10]. Also, the standard practice for track maintenance planning relies on the Track Quality Index (TQI). Several TQIs have been developed based on the experience of railway authorities to fit local requirements [11], and those TQIs share the same principle in development by relying on statistical analysis of track geometry parameters [10].

In recent years, condition-based maintenance, a part of preventive maintenance, has received considerable attention in the railway industry [12–15]. Condition-based maintenance aims to correct incipient, moderate, or severe defects based on sensing data from the track. Historical data from monitoring activities allow us to predict railway track conditions, have an overview of the different types of defects and failures registered in the railway line, and estimate the time that a defect will reach a severe or failure condition. Thus, condition-based maintenance allows the focus of activities on those locations where a significant impact can be expected [16].

1.1.2. TRACK SUPPORT CONDITION

1.1.2.1. DEFINITION OF TRACK SUPPORT CONDITION

As shown in Figure 1.1, the ballast and substructure are crucial structures for supporting the track superstructure, transferring traffic loads, facilitating drainage, and ensuring track alignment [17,18]. In this thesis, we define the condition of ballast and substructure as track support condition, which is an important property for characterizing the health of the railway track and a key input for implementing maintenance plans for the ballasted track.

Conventionally, track geometry parameters are considered indicators of track support condition in standard practices [19]. Besides, a physical parameter that can be considered is the track stiffness, which describes how the track deforms and recovers when subjected to a load. Previous studies have mainly focused on the track behavior as a whole, i.e., the global track stiffness [20–22]. Recent works have shown the possibility of analyzing different layers of stiffness parameters to estimate railpad and ballast stiffness [23,24]. In this thesis, the health condition of ballast and substructure layers is estimated by measuring the energy content obtained from the dynamic responses of moving trains. Axle box acceleration (ABA) measurements are considered for quantifying and assessing the track support condition.
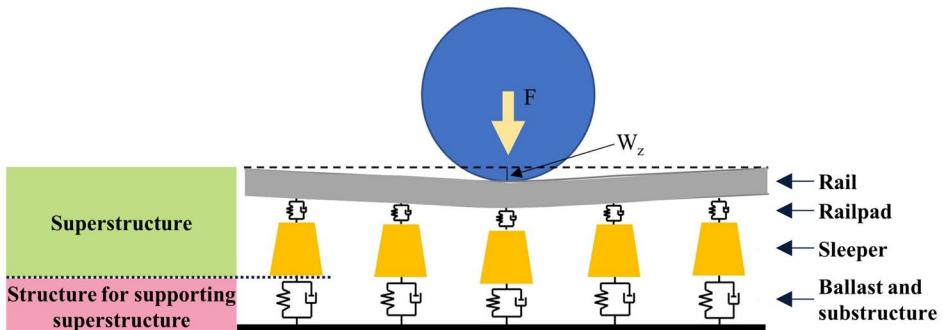
Figure 1.1: Track superstructure components and their supporting structure.

1.1.2.2. CONSEQUENCES REGARDING POOR TRACK SUPPORT CONDITION

The degradation of the ballast and substructure layers due to use and time results in poor track support conditions, see Figure 1.2. Broken ballast, mud pumping, and excessive track settlement are some examples. Furthermore, vegetation and excessive undrained water on the track surface suggest a high moisture content in the substructure layer, resulting in a lower bearing capacity of materials [10]. These degraded track segments can cause abrupt changes in train-track interaction, which increases risks and safety concerns, as well as reduces the service quality of train operations. Besides, degradations from usage, disasters, soft subgrade, and fluctuations in groundwater level are external factors that contribute to degradation in track support conditions, especially in the Netherlands, where railway embankment stability is a major challenge [25].

1
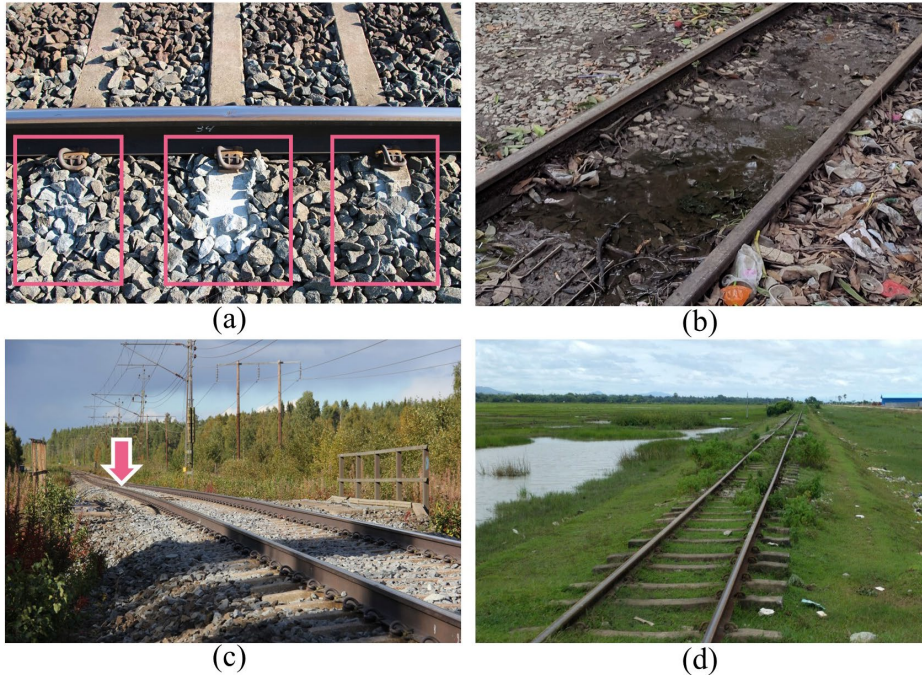
Figure 1.2: Degraded track segments regarding poor conditions of ballast and substructure layers:
(a) ballast breakage; (b) mud pumping and excessive undrained water; (c) excessive track settlement
as indicated by the arrow; and (d) vegetation in the track.

Additionally, railway transition zones, the segments between the conventional track and rigid structures, such as bridges, tunnels, and culverts, have been reported to suffer degradation more rapidly than conventional tracks [22,26–32]. The fast degradation at transition zones is mainly attributed to the variation in track support [20,26,33–37]. For example, in the Netherlands, it has been reported that the maintenance frequency at transition zones can be 2-8 times that for conventional tracks [38], leading to costly maintenance activities and largely reducing track availability. Those consequences have attracted extensive worldwide attention from the railway community and motivated studies in various approaches for understanding the transition zone behaviors, such as modeling [39–46] and monitoring [33,47–52].

Degradation of the transition zones can occur from a poor ballast layer, an insufficient rail constraint, an embankment foundation that is too soft, train speeds higher than the design speed, and an excessively heavy train axle load, among other reasons [26,34].

1

Therefore, a particular transition zone needs customized solutions because of its specific designs, structures, bearing capacity, and soil conditions. Each country has regulations for designing and constructing railway transition zones [34]. The maintenance solutions for transition zones are ballast tamping or stone blowing [53], the use of under sleeper pads [54], ballast glue with polymers [55], auxiliary rails [56], and adjustable fasteners [57]. In this thesis, transition zones are selected as a case study because of their sharp change in track support conditions. When ABA measurements are able to observe their behavior in the train-track interaction response, the next step is to verify how sensitive the signals are to track support condition at conventional track segments.

1.1.3. MEASUREMENTS FOR TRACK SUPPORT CONDITION

Different techniques have been proposed in the literature for assessing the condition of the ballast and substructure layers. In this section, some of the techniques and principles behind trackside and onboard measurements for track support conditions are reviewed as follows.

1.1.3.1. TRACKSIDE MEASUREMENTS

Several trackside measurement techniques have been developed for evaluating track conditions [58]. They can be grouped into two categories: 1) those that do not require excitation from train passages and 2) those that require excitation from train passages.

For the first category, example techniques are the dynamic cone penetrometer (DCP) for evaluating the strength and variability of the soil layers [59,60], the falling weight deflectometer (FWD) for estimating the elastic modulus of the underlying material layers [61,62], the impact hammer tests for identifying track dynamic characteristics from frequency response functions (FRFs) [48,63] and estimating track component parameters, such as the railpad and ballast stiffness [23].

Regarding the second category, various sensors are employed to monitor track responses due to the excitation from train passages. Subsequently, the monitored responses are interpreted into track conditions. Example use cases of those sensors are summarized in Table 1.1. Recently, the latest sensing techniques and the Internet of Things (IoT) have been applied to enhance the ability to monitor railway tracks and automate the processing of

frequent measurements [64–66]. These techniques provide valuable insights and information about the track condition at particular testing locations.

Despite these advancements, comprehensive instrumentation of railway tracks across a large-scale network is challenging and might not be practical in real-life applications. The costs associated with equipment, installation, and maintenance of the measurement system are relatively high. The difficulty of accessing remote areas further complicates extensive trackside measurement campaigns. Therefore, most trackside measurement techniques provide track condition information at selected locations, meaning that not every location in the network is effectively monitored.

Table 1.1: Sensors for trackside measurements that required train passage excitation

Types of sensor	Instrumented location and objective
Accelerometers	• Soil, for measuring ground acceleration [47] • Sleeper, for measuring the acceleration [48] [67] [68]
Geophone	• Sleeper, for measuring the displacement [47]
Piezometer	• Embankment, for measuring the pore water pressure [47]
Strain gage	• Rail, for calculating the wheel load [33] [48]
Linear variable differential transformer (LVDT)	• Rail, for measuring the displacement [48] • Sleeper, for measuring the displacement [33] [48] [67] • Various layers of the substructure, using a set of LVDTs called Multidepth deflectometers (MDDs), for measuring the settlement of a particular layer [33,69,70]
Laser-based position detector	• Rail, for measuring the displacement [48]
Digital image correlation (DIC)	• Rail, for measuring the displacement [71,72] • Sleeper, for measuring the displacement [71,72]

1.1.3.2. ONBOARD MEASUREMENTS

Onboard and continuous measurement techniques for identifying problematic track sections are essential for maintenance planning at the network level. Several measurement techniques have been developed by using dedicated vehicles. For example, track geometry parameters using track recording vehicles [19], and track stiffness measurement vehicles, either deflection-based measurement techniques [20,73–76], or vibration-based measurement techniques [73,77]. Those mentioned techniques rely on a dedicated, tailor-

1

developed system. Consequently, the frequency of measurement campaigns covering the whole network might be limited due to the availability of the measurement systems.

Onboard sensing using in-service trains has been a focus of the railway industry to overcome the limitations of dedicated measurement systems. Several studies have been conducted to find solutions to use vehicle responses for assessing track conditions. For example, estimating track irregularities from vehicle responses, i.e., car body accelerations [78,79], bogie acceleration [78,80–84], axle box acceleration [83], wheelset acceleration, and yaw angular velocity [84].

Besides, some studies develop indicators for track condition assessment derived from measured vehicle responses. For instance, a damage indicator derived from wavelet coefficients of vehicle body acceleration [85], a simplified bump pattern derived from vehicle body acceleration [86], and track change detection based on extracted features from vehicle body acceleration [87], track quality and ride comfort based on accelerations inside the passenger wagon measured by smartphones [88]. In this thesis, the focus is on assessing the capabilities of ABA measurements to estimate track support conditions and to develop indicators that facilitate a systematic evaluation of the condition of transition zones and conventional straight tracks.

1.1.4. TRACK SUPPORT CONDITION INDICATORS

1.1.4.1. STANDARD PRACTICE INDICATORS BASED ON TRACK GEOMETRY PARAMETERS

The measurement of track geometry [89] using track recording vehicles [19] is the standard practice in the railway industry for track inspection at the network level. Various track quality indices (TQIs) have been developed based on statistical analyses of track geometry parameters and combined using mathematical methods. TQIs are then used by railway authorities or infrastructure managers to standardize track quality and define maintenance requirements. Examples of conventional TQIs are the combined standard deviation (CoSD) of the European standard [90], the Q index of the Swedish national railway [91,92], the Chinese TQI [93], the US track roughness index [91,94], and the FRA track geometry index [95].

1.1.4.2. CHALLENGES IN USING TRACK GEOMETRY-BASED INDICATORS

Conventional TQIs have some limitations. Results in [96] indicate that the US track roughness index and FRA Track Geometry Index (TGI) show high sensitivity due to changes in geometry parameters, which might be easily influenced by noise or errors in measurement. In [97], the characteristics of 14 TQIs have been studied. The results show that the standard deviation-based TQIs perform well but are biased in some cases, such as track gauge widening in the curved track segments. Therefore, data-driven and machine-learning approaches have been studied to extract information from track geometry parameters. Some applications based on these approaches are track geometry degradation predictions [98,99], TQIs from dimension reduction [11,100] and from the Bayesian analysis [101] of track geometry parameters, and finding a relationship between track geometry parameters and the wheel load ratio using neural network models [102]. Nevertheless, further understanding of the physical meaning of the results is required by including the physical interpretability of the results.

Additionally, track geometry measurements cannot always capture abrupt changes in train-track interaction [102,103]. Moreover, measurement frequency might be limited due to the availability of track-recording vehicles. Thus, measurement techniques using in-service trains are becoming the focus in the railway industry since vehicle responses, reflecting train-track interaction, are frequently obtained as inputs for track quality assessment. Outcomes from vehicle response measurements can be used separately or supplementary to conventional TQIs for more effective track maintenance planning rather than relying solely on track geometry information from dedicated track recording vehicles. In this thesis, the focus is on systematizing the extraction of useful information from ABA measurements and providing experimental evidence to support the efforts towards standardization of such a type of measurement system. It is thus to make it possible for an almost continuous estimation of the support condition of the railway tracks just by using the same trains in operation.

1

1.1.4.3. ENHANCING STANDARD PRACTICE INDICATORS WITH DYNAMIC RESPONSES OF MOVING TRAINS

Information from dynamic responses of moving trains, representing train-track interaction, can be considered as information to make track condition assessment comprehensive and more informative. A train passage excites the track system and simultaneously can acquire such information. In particular, sensors mounted on the train capture vehicle dynamic responses corresponding to the whole track system. With the current know-how in railway engineering, it is possible to identify some of the track components and their conditions from the measured dynamic responses.

This thesis considers the ABA measurement as the dynamic responses. The ABA measurement system was initially developed for rail defects detection and condition monitoring of superstructure components [13,104–114], where ABA signals in the high-frequency range, corresponding to short wave irregularities, are fundamental. However, it has been reported that the substructure mainly responds in the low-frequency range [23,115–117], corresponding to long wave irregularities. According to the literature, longitudinal irregularities in the wavelength from 3 m to 25 m are dominated by substructure variations [118,119]. Measurements in the low-frequency range are used as one of the criteria for the decision of tamping [18] and for the analysis of track settlements [120]. Therefore, analyzing ABA signals corresponding to wavelengths from 3 m to 25 m is the initial step for track support condition assessment.

Still, additional support for the physical interpretation of ABA measurements is required. In this thesis, hammer and falling weight impact tests are conducted, and correlations with ABA measurements are analyzed. The correct characterization of ABA responses at track segments with various track support conditions is a fundamental input required for maintenance planning for the ballast and substructure layers.

1.2. RESEARCH QUESTIONS

The main objective of this thesis is to provide infrastructure managers with insights into the track support condition derived from ABA measurements. Later, this information can

facilitate decision-making processes in track maintenance at the network level. Hence, the main research question is formulated as follows.

How can the track support condition be quantified using ABA signals and leverage this information to support maintenance decision-making?

The following sub-research questions are formulated to address the main research question comprehensively.

Sub-question 1: *What are the important characteristics of ABA signals, under different measurement conditions, regarding changes in track support condition?*

This sub-question is addressed in Chapter 2: Multiple-ABA measurements at railway transition zones.

Understanding the characteristics of ABA signals with respect to various track support conditions is crucial. In addition, the ABA measurement system is implemented with in-service trains, which have different operating conditions (such as different speeds). Thus, the findings in the chapter are essential for the foremost step in quantifying the substructure condition. We consider railway transition zones as case studies since abrupt changes in track support conditions can be frequently found.

Sub-question 2: *What method can be used to quantify the track support condition utilizing ABA signals?*

This sub-question is addressed in Chapter 2: Multiple-ABA measurements at railway transition zones.

Once ABA signals are evaluated regarding the repeatability and consistency of the responses in the low-frequency range, a framework is needed to quantify and compare the track support condition. The method that is proposed in this thesis relies on the energy density of ABA responses in the low-frequency range. Then, a method based on the design of key performance indicators (KPIs) for transition zones is investigated for the systematic evaluation of track support conditions.

Sub-question 3: *Can impact tests provide insights into the physical interpretability of the ABA signals?*

This sub-question is addressed in Chapter 3: Framework for physical interpretation of ABA signals.

While consistent low-frequency responses of ABA are obtained, containing responses from ballast and substructure, a question could also be raised about whether the signals can reflect the condition of each component separately. Thus, by answering this question, we can evaluate whether or not additional information to understand the ABA signals can be obtained from the frequency response function of impact tests. When the resonances identified in the impact tests can be related to changes in the ABA responses, we can provide additional physical interpretability of the onboard measurement system.

Sub-question 4: *How can ABA-based track support conditions be leveraged in supporting track maintenance decision-making?*

This sub-question is addressed in Chapter 4: Enhanced vertical track quality index with ABA Signals.

Conventional track quality indices (TQIs), the standard practice for track maintenance planning, have limitations in indicating track segments that provide poor train-track interaction. Hence, a framework for designing an enhanced vertical track quality index, called EnVTQI, is proposed. It combines a conventional TQI with vehicle dynamic responses from ABA measurements, aiming to provide an informative indicator for supporting maintenance decision-making.

1.3. DISSERTATION OUTLINE

The structure of this dissertation consists of 5 chapters, as shown in Figure 1.3. Chapter 1 presents the background of this thesis and the problem statement. The first part of Chapter 2 presents the characteristics of ABA signals from various perspectives, such as repeatability, speed dependency, and sensitivity in local change detection. Then, the later part of Chapter 2 proposes a framework for designing ABA energy-based KPIs for track support condition quantification and assessment. Chapter 3 discusses the relationship

between responses of ABA and track dynamics due to impact excitation. Then, by combining knowledge from the previous chapters, the framework for utilizing ABA signals to enhance the standard practice TQI is described in Chapter 4. Finally, conclusions and recommendations for further research are presented in Chapter 5.
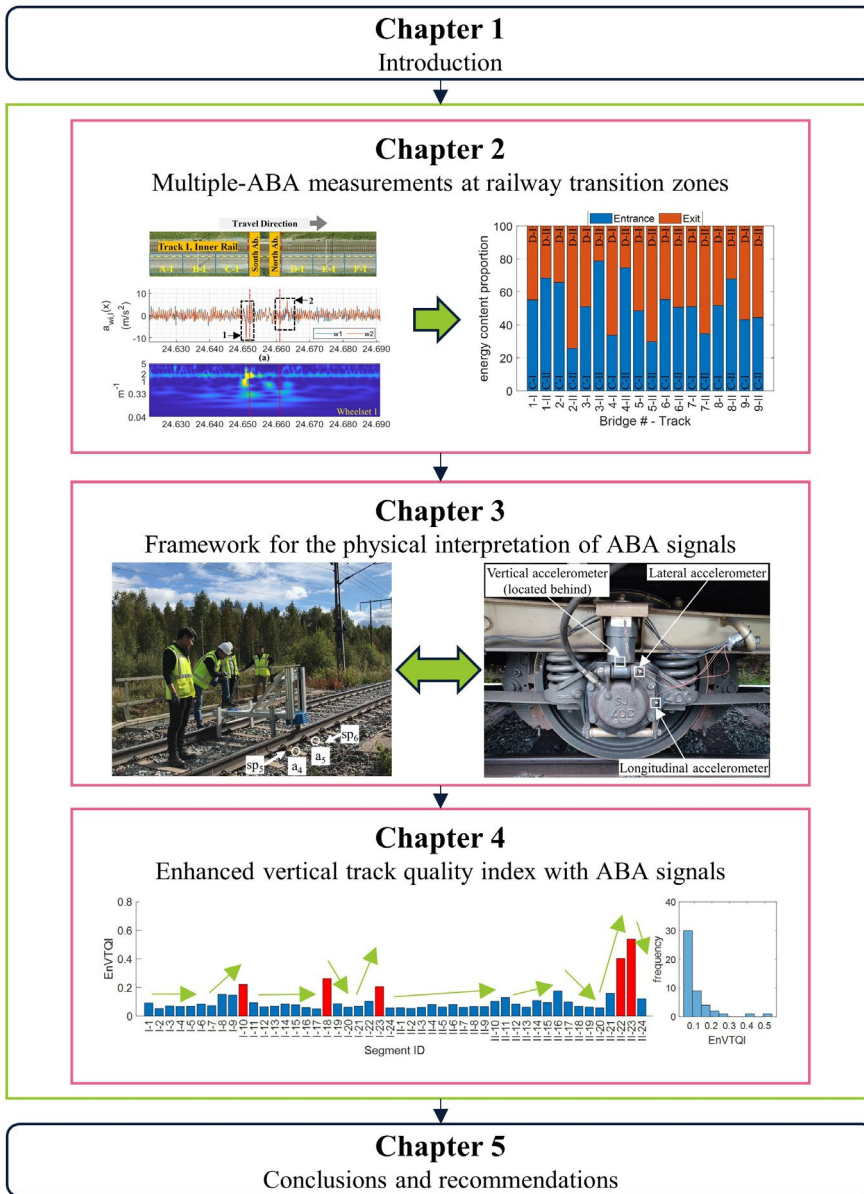
Figure 1.3: Dissertation outline.

2

MULTIPLE-ABA MEASUREMENTS AT RAILWAY TRANSITION ZONES

This chapter presents a methodology for monitoring transition zones using responses of multiple-axle box acceleration (multi-ABA) measurements. The time-frequency characteristics of the vertical ABA signals from four wheelsets are analyzed. The major contributions are as follows. 1) We propose four key performance indicators (KPIs) to quantify local multi-ABA energy differences at different abutments, tracks, entrance and exit sides, and inner and outer rails. 2) The same dominant spatial frequencies are obtained with different measurement speeds, so the proposed method is suitable for multi-ABA systems mounted on operational trains. Transition zones at nine double-track railway bridges are selected as the case study. The KPIs indicate that 1) the energy differences between abutments are above 80% in three bridges; 2) two abutments show that the energy differences between tracks are higher than 100%; 3) three tracks have energy differences above 100% between the entrance and exit sides; and 4) the energy differences between rails are above 80% on three sides. Finally, using measurement with 7 years of difference, the KPIs and track quality index are discussed. These findings suggest that multi-ABA measurement can be used as a health condition monitoring method for railway transition zones to support condition-based maintenance.

2.1. INTRODUCTION

Railway transition zones are the segments between the conventional track and rigid structures, such as bridges, tunnels, and culverts. The degradation of track geometries at transition zones usually occurs much faster than at other locations [22,26–32]. For example, in the Netherlands, it has been reported that the maintenance frequency at transition zones can be 2-8 times that for typical tracks [38]. This frequent maintenance is very costly and largely reduces track availability.

The fast degradation of transition zones has attracted extensive worldwide attention from the railway community. The literature on railway transition zones covers various approaches for understanding the corresponding behavior, such as modeling [39–46] and monitoring [33,47–52]. The fast degradation at railway transition zones is mainly attributed to the variation in track support [20,26,33–37].

In addition to differential track support, degradation can occur from secondary causes, such as a poor ballast layer, an insufficient lateral rail constraint, an embankment foundation that is too soft, train speeds higher than the design speed, and an excessively heavy train axle load [26,34]. Therefore, a particular transition zone needs customized solutions because of its specific designs, structures, bearing capacity, soil conditions, etc. Each country has regulations for designing and constructing railway transition zones [34]. The maintenance solutions for transition zones have varied from ballast tamping or stone blowing [53] to the use of under sleeper pads [54], ballast glue with polymers [55], auxiliary rails [56], and adjustable fasteners [57].

These different solutions, combined with the functional service conditions of the transition zones, make the corresponding health monitoring task complex. Researchers in the railway field aim to extract valuable and practical information from transition zones from various measurements. At present, many measurement techniques have been developed to monitor the health conditions of railway transition zones, including trackside and onboard measurement techniques [58]. Trackside measurements can monitor responses from instrumented transition zones at specific locations and subsequently interpret them into health condition indicators. Every train passage generates the excitation required to

acquire health condition information. In the case of onboard measurements, every train passage acquires information from all the transition zones it visits. In particular, sensors mounted on the vehicle capture the responses related to the train-track interaction. These measurements contain the whole track system response. Identifying which parts of the responses are related to each track component can be challenging, especially in terms of low and middle frequency ranges [23,115–117]. Track monitoring benefits from both trackside and onboard measurements.

In this study, we focus on onboard sensing, considering that nowadays, most rolling stock manufacturers are already instrumenting all their rolling stocks, while campaigns for the instrumentation of each and every transition zone still have open challenges when thinking of massive instrumentations in large-scale networks. In [47], a 1-year monitoring campaign of a transition zone at a culvert with concrete approach slabs was conducted considering the vertical displacement and settlement using geophones, accelerometers, and pore water pressure sensors. The results showed that poor performance in the vertical displacement was due to the settlement and rotation of one approach slab. In [33], six months of field monitoring indicated that hanging sleepers or sleepers in poor support conditions were a direct cause of permanent vertical deformation in transition zones. Poor sleeper support increases the applied stress from the sleeper to the ballast. In [48], a monitoring framework was developed to assess the performance of transition zones at culverts. The framework included measurements based on the track dynamic flexibility using hammer tests, vertical acceleration, and displacement responses of the track components (rails, sleepers) using linear variable differential transformers (LVDTs) and a laser-based position-sensitive detector. In [67], a measurement campaign was described for assessing the performance of the novel solution of the transition zone. The responses of track components, including vertical acceleration of sleepers, vertical displacement of sleepers, rails shear stress, and vertical displacement of rails, were selected for the assessment. In [68], three transition zones with different structural details were instrumented with accelerometers at sleepers at the bridge, transition zone, and open track to assess their performance. The results showed that sleeper acceleration of the well-performed transition zone was less than 5g, which was similar to the responses of a sleeper on the open track. In contrast, transition zones with track geometry problems were found to

provide sleeper acceleration higher than 10g. In [69], so-called multidepth deflectometers (MDDs) were introduced to the research framework to investigate differential movement in railway transitions. Then, in [70], MDDs were used to monitor track substructure settlement at different layers. The measurement consisted of permanent deformation monitoring and transient deformation corresponding to the train load. The findings showed that the ballast layer was the most deformed for both accumulated permanent and transient deformations. In addition, digital image correlation (DIC) [71,72], satellite synthetic aperture radar (InSAR) [121], smartphones [88], and geometry measurements [122] have been used to monitor the differential settlement, settlement rate and other characteristics in transition zones. The methods discussed above have general drawbacks, such as complex measurement procedures with high costs, low data acquisition, and transmission efficiency, or a limitation to the geometry state instead of structural conditions. The latest sensing techniques and Internet of Things (IoT) developments are expected to enable full instrumentation of railway bridge transition zones and automatic processing of frequent measurements [64–66].

This study considers a multiple-axle box acceleration (multi-ABA) monitoring technique that relies on onboard measurements and has been implemented on operational trains, enabling frequent condition monitoring of transition zones and other railway track components. The axle box acceleration (ABA) measurement method was developed for railway track defect detection [104–106]. With this method, the local dynamic response deviation can be evaluated and compared to the measurements obtained under healthy conditions. In previous studies, ABA measurements were used to detect squats in rail surfaces, perform condition assessments of insulated rail joints, welds, crossing noses, and measure joint bolt tightness [13,110,112–114]. The high-frequency range of ABA is fundamental for detecting the abovementioned shortwave irregularities. The present study is intended to characterize the ABA responses at railway bridge transition zones as case studies to allow further developments of condition-based assessments of railway transition zones and maintenance solutions, especially substructures that consist of layers of ballast, subballast, and subgrade [17]. Note that in some reports, the subballast and ballast were considered part of the superstructure.

This study focuses on the spatial frequency range from 0.04 m^{-1} to 0.33 m^{-1}, corresponding to the D1 wavelength range of track longitudinal irregularities from 3 m to 25 m [89]. This longitudinal wavelength range has been reported to be dominated by substructure variations [118,119], is used as one of the criteria for measuring tamping activity [18], and is used for the analysis of track settlement modeling [120]. Multi-ABA measurements include acceleration signals in the vertical direction on multiple wheelsets; such signals are considered the primary input to define the responses of railway transition zones. Then, multi-ABA signal responses at different transition zone locations are analyzed. It has been reported that more severe track conditions cause higher dynamic wheel loads [18]. Thus, a method is proposed here to compare the degradation level of transition zones at a particular bridge based on ABA energy, as larger ABA energies should be observed for tracks with more degradation. We propose four key performance indicators (KPIs) based on multi-ABA measurements to evaluate the differences in energy levels between different abutments, tracks, sides, and rails at each bridge.

This chapter is organized as follows. The proposed methodology for monitoring railway transition zones using multi-ABA is presented in Section 2.2. Section 2.3 describes an analysis of multi-ABA signals from different wheelsets and different measurement speeds. Next, the responses of multi-ABA signals at various transition zone study areas are analyzed in Section 2.4. Section 2.5 presents results from the degradation level evaluation of transition zones using KPIs based on multi-ABA measurements. The evolution of KPIs over time is analyzed in Section 2.6. Finally, the conclusion of this study and suggestions for further research are presented in Section 2.7.

2.2. MULTIPLE-ABA MEASUREMENT AT TRANSITION ZONES

The methodology of this study is shown in Figure 2.1. The first step is data collection. Next, wavelets are used to extract multi-ABA signal characteristics, and the multi-ABA responses are analyzed at various locations of a particular railway bridge. Finally, the condition of railway transition zones is evaluated using the ABA energy as the basis of four KPIs that quantify differences between abutments, tracks, sides, and rails.

2
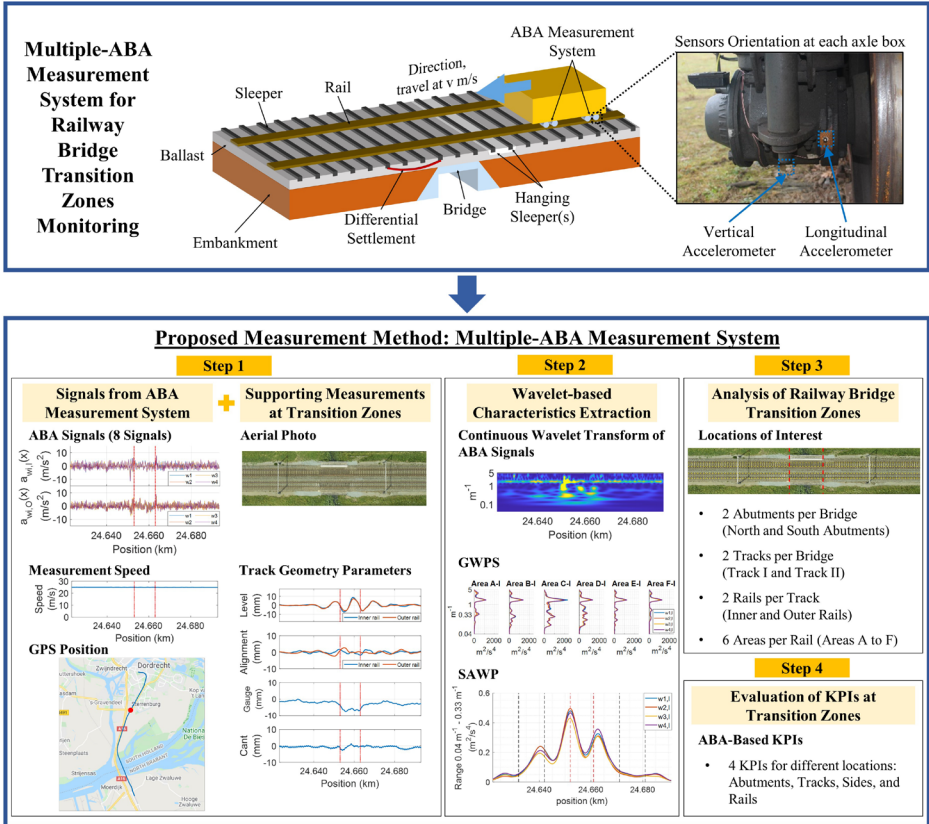
Figure 2.1: Proposed methodology of this chapter.

(source of aerial photographs: BBMS, ProRail, source of background map: Google Maps).

2.2.1. DATA COLLECTION AT RAILWAY TRANSITION ZONES

The ABA measurement system [123] consists of three major components. First, 1-directional accelerometers with linear characteristics up to 10 kHz are attached and aligned with the center of each axle box in the vertical and longitudinal directions, with respect to the train travel direction. Second, a global positioning system (GPS) antenna and tachometer are used to determine the position and running speed of the measurement train. Third, an NI compact RIO data acquisition system records signals with synchronized sampling between all channels. The acceleration at time instant t for wheelset w and rail r is defined as $a_{w,r}(t)$. Eight acceleration signals from four wheelsets $w \in \{w1, w2, w3, w4\}$ and the inner (I) and outer (O) rails $r \in \{I, O\}$ are considered. The front wheelset at the front

bogie is $w1$, the rear wheelset at the front bogie is $w2$, the front wheelset at the rear bogie is $w3$, and the rear wheelset at the rear bogie is $w4$. The location of the wheelset w at time instant t is $x_w(t)$. Then, after synchronizing the signals, the acceleration signals can be evaluated as a function of the track location x, $a_{w,r}(x)$. According to the system configuration, the measurement system records ABA signals with a sampling rate of 25.6 kHz. However, several studies have reported that the track substructure vibration responses occur in a frequency range below 100 Hz [124–126]. In this chapter, the considered wavelength λ of track irregularities is from 3 m to 25 m. These irregularities are the excitation, and the corresponding passing frequency f at speed V of the measurement train is:

$$f = \frac{V}{\lambda}$$

Eq. 2.1

The maximum operating speed in the conventional Dutch railway network is 140 km/h. Therefore, the corresponding frequencies of interest are on the order of 12.96 Hz. A 4th-order Butterworth low-pass filter with 100 Hz cut-off frequency is used to preprocess the measured ABA signals to cover the considered dynamic responses.

In addition, supporting information is considered from the Dutch railway infrastructure monitoring database, called the Branche Breed Monitoring Systeem (BBMS, in Dutch), including aerial photographs and track geometry measurements. The track geometry measurements include six parameters: The longitudinal level of inner rail and outer rail (deviation of the top of rail head in the vertical direction from the reference line), alignment of inner rail and outer rail (deviation of the side of rail head in the lateral direction from the reference line), track gauge (perpendicular distance between the inner side of rail head), and cant (different height between the top of rail heads). The data are all positioned in the Dutch railway reference system.

2.2.2. RESPONSE EXTRACTIONS USING THE WAVELET

ABA signals are nonstationary and capture the track characteristic frequency responses at different locations. One of the well-known methods for analyzing these local variations is wavelet analysis. The continuous wavelet transform (CWT) converts the acceleration

signals into energy at a specific location and frequency based on a group of shifted and scaled wavelet functions. The CWT is defined in [127] as follows:

$$CWT_{w,r}(x,s) = \sum_{n'=0}^{N-1} a_{w,r}(n')\psi^*\left(\frac{(n'-n)\delta_t}{s}\right)$$

Eq. 2.2

where $CWT_{w,r}(x,s)$ is the wavelet coefficient of the acceleration signal from wheel w and rail r at location x and wavelet scale s with $s > 0$, N is the number of data points in a considered time frame, $n = 0, \ldots, N-1$, $a_{w,r}(n')$ is the ABA signal at instant $t = n'$, n is the time index variable for the continuous translation, δ_t is the time interval between data points, and Ψ is the wavelet mother function. The function Ψ^* is a family of wavelets derived from the mother wavelet by translations and scaling, and * refers to the complex conjugate. In this chapter, the Morlet function is used as the mother wavelet.

Finally, the wavelet power spectrum (WPS) is defined as the square of the absolute wavelet coefficients:

$$WPS_{w,r}(x,s) = \left|CWT_{w,r}(x,s)\right|^2$$

Eq. 2.3

where $WPS_{w,r}(x,s)$ is the WPS of the acceleration signal from wheel w and rail r at location x and wavelet scale s with $s > 0$. The scalogram, a plot representing a function of time and frequency, is used to visualize the WPS. Instead of the time domain, the space domain, according to the track position, is used at each instance. Moreover, the spatial frequency (m^{-1}), the inverse of the wavelength obtained by dividing the measured frequency by the measured speed, is considered due to the speed differences between different measurements. Therefore, the scalogram in the space domain function and the spatial frequency domain are used instead of the time and frequency domains. This modified scalogram can reflect the primary track responses with various measurement speeds at different locations.

Then, the global wavelet power spectrum (GWPS) is used to evaluate an average of the WPS within a particular segment of positions, calculated as follows:

$$GWPS_{w,r}(s) = \frac{1}{n_2 - n_1} \sum_{n=n_1}^{n_2} WPS_{w,r}(x_n, s), \quad x_{n_1} < x_n < x_{n_2} \qquad \text{Eq. 2.4}$$

where $GWPS_{w,r}(s)$ is the GWPS of the acceleration signal from wheel w and rail r, within the location from x_{n1} to x_{n2}, for wavelet scale s with $s > 0$, $WPS_{w,r}(x_n,s)$ is the wavelet power spectrum at position x_n, and n_1 and n_2 are selected according to the preferred window length of the analysis.

Finally, the scale average wavelet power (SAWP) is used to investigate the WPS within a considered spatial frequency range and can be defined as follows:

$$SAWP_{w,r}(x) = \frac{\delta_j \delta_t}{C_\delta} \sum_{j=j_1}^{j_2} \frac{WPS_{w,r}(x, s_j)}{s_j} \qquad \text{Eq. 2.5}$$

where $SAWP_{w,r}(x)$ is the SAWP of the acceleration signal from wheel w and rail r, at location x and within the wavelet scale s from s_{j1} to s_{j2}, $WPS_{w,r}(x,s_j)$ is the wavelet power spectrum at scale j, δ_j is the scale step, δ_t is the time step, and C_δ is the empirically derived constant of the wavelet function.

2.2.3. RAILWAY BRIDGE TRANSITION ZONES

This section aims to provide solutions for monitoring the substructure at conventional railway lines, particularly due to the generally poor bearing capacity of the Dutch soil. In this chapter, we first consider the challenges at bridge transition zones. At those locations, a sharp change in track stiffness occurs, and the lower frequency responses of ABA show a dramatic change, where ballast, subballast, and subgrade responses dominate.

This studied railway line is double-track with fixed travel directions; see Figure 2.2. Track I is for trains traveling from Lage Zwaluwe to Dordrecht, and Track II is for trains traveling from Dordrecht to Lage Zwaluwe. The health condition of the transition zones is estimated by analyzing the measurements at different locations. These locations include the entrance and exit sides on each of the two tracks, abutments (dashed red lines in Figure 2.2), and the inner and outer rails (dashed yellow lines in Figure 2.2). A segment length of 30 m was reported to be sufficient for investigating transition zones [26,46,128], in line with the maximum wavelength of 25 m of interest. Thus, track sections are analyzed at both

ends of the bridge, from 30 m before the abutment on the entrance side to 30 m from the abutment on the exit side. Analysis of the energy content of the multi-ABA signals indicated that 53% of the energy is concentrated in the first 10 m next to the bridge. Thus, we analyze six areas that are 10 m in length at the entrance side (Areas A-I to C-I for Track I and Areas A-II to C-II for Track II) and the exit side (Areas D-I to F-I for Track I and Areas D-II to F-II for Track II). The partitioning of 10 m helps visualize the spatial characteristics of transition zones. The farther the zone is from the bridge (zones A and F), the closer the response is to the conventional track. Further, the estimation of SAWP and wavelet responses from multi-ABA measurements do not require the proposed partitioning for analysis.
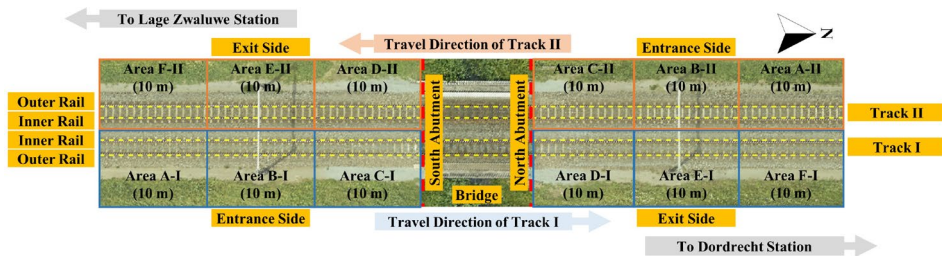
Figure 2.2: Study areas of transition zones at the double-track railway bridge (source of aerial photographs: BBMS, ProRail).

2.2.4. CASE STUDIES OF RAILWAY BRIDGE TRANSITION ZONES

Transition zones at nine railway bridges between Dordrecht station and Lage Zwaluwe station, denoted as Bridge 1 to Bridge 9, are selected as the case studies. Figure 2.3 presents a map of the bridge locations, which are indicated with red dots. Bridges 1, 2, and 3 are bridges that cross urban roads in the city of Dordrecht. Bridges 4 and 6 cross over small waterways. Bridge 5 crosses over bicycle paths. Bridge 7 is the Moerdijk bridge that crosses the river Hollands Diep. Bridge 8 crosses a rural road, and Bridge 9 crosses a regional railway track. Table 2.1 shows detailed information for each bridge, including aerial photographs and side view photographs.

The measurement campaign was conducted at both tracks in May 2019. Two measurements are available for Track I (between Lage Zwaluwe and Dordrecht), denoted as Track I#1 and Track I#2. The two additional measurements for Track II (between

Dordrecht and Lage Zwaluwe) are called Track II#1 and Track II#2. Figure 2.4 shows the speed profile of the measurements and the average speed over 30 m when the train enters and exits the bridges.


Figure 2.3: Location of bridges between Dordrecht station and Lage Zwaluwe station (source of the background map: Google Maps).
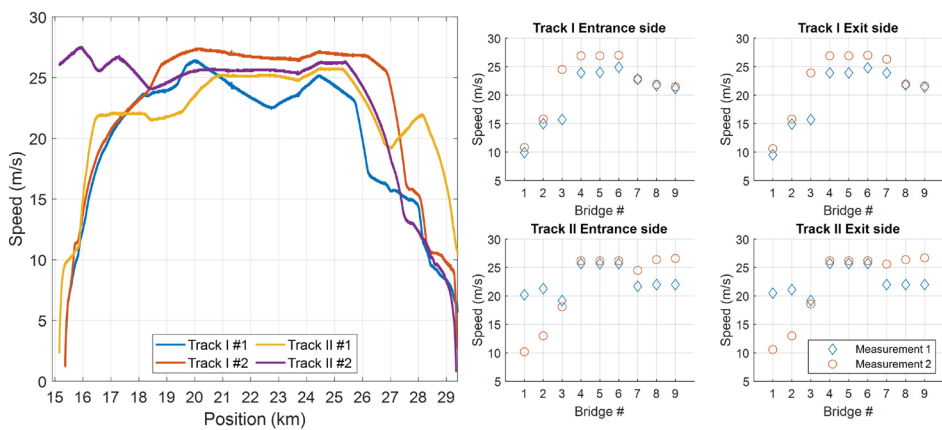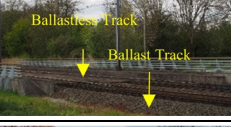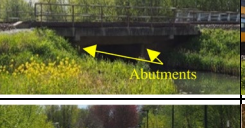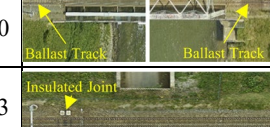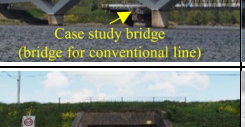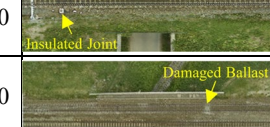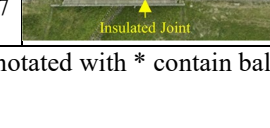
Figure 2.4: Speed profile and average speed of the ABA measurement system at each transition zone from the measurement campaigns.

Table 2.1: Railway bridge transition zones, aerial photographs, and side-view photographs (source of aerial photographs: BBMS, ProRail).

2

Transition Zone at Bridge	Position (km)	Aerial Photo	Side-View Photos	
1	28.416 – 28.433	Insulated Joint		
2*	27.729 – 27.764	Ballastless Track / Auxiliary rails		Ballastless Track / Ballast Track
3	26.994 – 27.022	Damaged Ballast / Insulated Joint / Auxiliary rails		Freight train
4	25.256 – 25.265		Abutments	
5	25.233 – 25.242	Insulated Joint / Insulated Joint		Insulated Joint / Battery/Relay
6	24.652 – 24.661			Abutments
7*	17.835 – 18.940	Ballastless Track / Ballastless Track / Ballast Track / Ballast Track	Case study bridge (bridge for conventional line)	High Speed Line / Conventional Line
8	17.423 – 17.430	Insulated Joint / Insulated Joint		Thick embankment
9	17.270 – 17.297	Damaged Ballast / Insulated Joint		Thick embankment

Note: Bridges annotated with * contain ballastless track.

2.3. Multi-ABA RESPONSES FROM DIFFERENT WHEELSETS AND MEASUREMENT SPEEDS

This section analyzes the ABA signals from different wheelsets and different measurement speeds. To showcase the analysis of different wheelsets, signals from the inner rail at the transition zones of Track I at Bridge 6, measured at a speed of 24.9 m/s (Track I#1), are selected. Bridge 6 is selected because it is relatively isolated from insulated joints (the closest is 42.8 m away) and other bridges. Then, the analysis of measurement speeds considers Bridge 3, as it has the largest speed variations from the measurement campaign (15.7 m/s and 24.2 m/s).

2.3.1. Multi-ABA RESPONSES AT DIFFERENT WHEELSETS

Figure 2.5 shows that signals from all the wheelsets provide strong responses at positions close to both abutments. For Bridge 6, the responses near the South Abutment are stronger than the responses near the North Abutment. No indication of a significant difference in the wavelengths and amplitudes between the ABA signals measured from the four wheelsets is observed. Similar dominant peaks at the entrance and exit sides close to abutments are found from the four signals (see dashed rectangles 1 and 2 in Figure 2.5(a) and (b). Consequently, the WPS of the ABA signals from the four wheelsets follow similar patterns (see Figure 2.5(c), (d), (e), and (f)).

Figure 2.6 shows that the GWPS responses from different wheelsets in each study area contain the same number of dominant peaks with slight amplitude differences. For Track I of Bridge 6, in the considered spatial frequency range from 0.04 m^{-1} to 0.33 m^{-1}, the closer the area is to the bridge, the higher the total energy. Furthermore, the dominant peak at each area varies in frequency and amplitude, as indicated by the blue rectangles in Figure 2.6. Note the common peak outside the region of interest at 1.68 m^{-1}, which corresponds to a 0.60 m wavelength that is sleeper-related.

Figure 2.7 presents the SAWP in the spatial frequency range from 0.04 m^{-1} to 0.33 m^{-1} from the four wheelsets. Although similar SAWP patterns are observed, differences are found in the peak locations and amplitudes. For example, the peaks in Area C-I have amplitudes between 0.48 m^2/s^4 and 0.67 m^2/s^4, and the positions of the peaks vary within a

range of approximately 1 m. In the case of Area D-I, the peaks have amplitudes between $0.31\ m^2/s^4$ and $0.47\ m^2/s^4$ with less than 1 m variation in the position of the peaks.
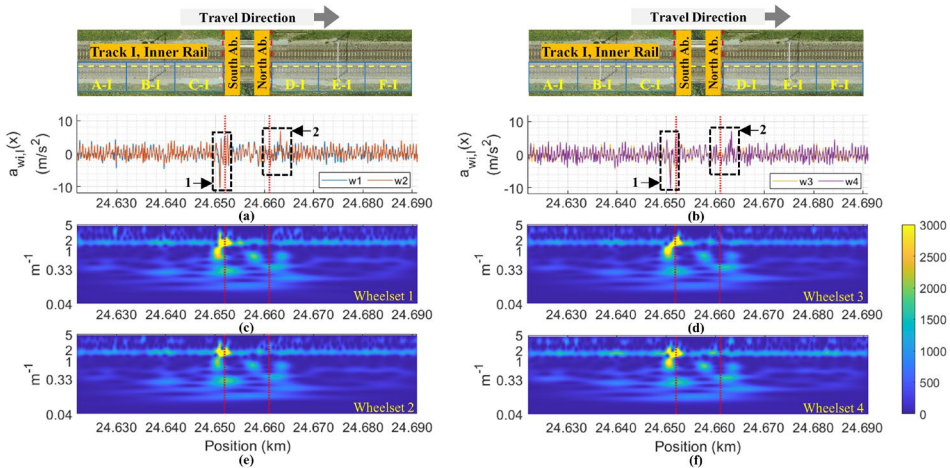
Figure 2.5: Responses of the ABA signals from 4 wheelsets measured at the inner rail of Track I at Bridge 6, ABA signals with 100 Hz cutoff frequency (source of aerial photographs: BBMS).
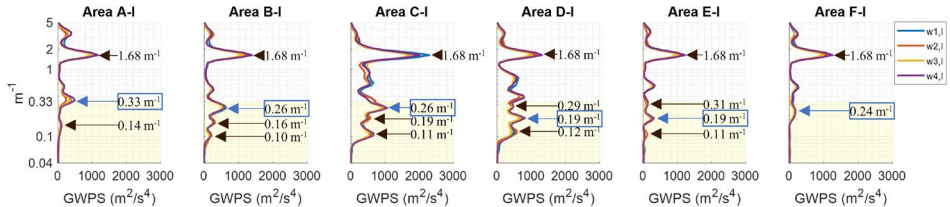
Figure 2.6: GWPS of the ABA signals of the transition zones at the inner rail of Track I at Bridge 6. A-I to C-I are areas on the entrance side, and D-I to F-I are areas on the exit side.
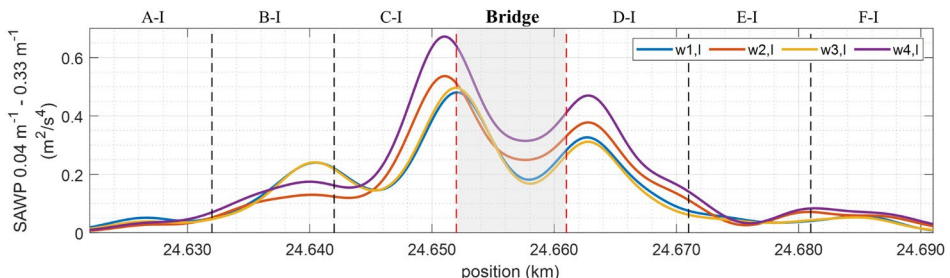

Figure 2.7: SAWP of the ABA signals from 4 wheelsets at the inner rail of Track I at Bridge 6.

Finally, different wheelsets provide similar responses when analyzing other transition zones. Thus, the average GWPS and SAWP can be considered to account for the minor

variabilities between wheelset responses. Furthermore, we observed local changes in the spatial frequency range between 0.04 m^{-1} and 0.33 m^{-1} for different transition zones. Thus, the total energy of the SAWP is a good candidate for determining a general KPI for transition zones.

2.3.2. INFLUENCE OF THE MEASUREMENT SPEED ON MULTI-ABA RESPONSES

The influence of the measurement speed on multi-ABA responses is analyzed since the measurement speeds at different transition zones can vary due to different operational and track conditions. For Bridge 3, the ABA signal responses of wheelset 1 are shown in Figure 2.8. The peak locations of the ABA signals are similar, but the amplitude of each peak is larger with a faster measurement speed (see Figure 2.8(a) and (c)). Measurements at different speeds show different WPS and GWPS responses in terms of the energy level, but the locations of the corresponding dominant spatial frequencies are similar, as shown in Figure 2.8(b) and (d) and Figure 2.9. We observe similar numbers of dominant peaks and notable alignment of peaks in all the different study areas (see yellow regions of Figure 2.9). This shows good repeatability of the measurements. Furthermore, a comparison of the SAWP values of the ABA signals from the two measurement speeds is presented in Figure 2.10. The result shows that a signal from a particular wheelset provides similar peak positions even though the measurement speeds are different. Moreover, the amplitude is larger with a faster measurement, and the differences are more prominent than with a slower measurement. Varying peak positions of approximately 1 m for different wheelsets are observed between measurements (as discussed in Section 2.3.1).

Finally, similar findings are obtained when analyzing other transition zones. That is, speed variations in the multi-ABA measurement have a minor influence on the location of the dominant peaks. However, the measurement speeds strongly influence the multi-ABA responses in terms of energy. As expected, faster speeds lead to larger dynamic responses of the train-track interactions [18]. The multi-ABA data characterize the responses of the whole track system under a very strong input excitation given by the moving load (train). This excitation is stronger than in conventional input excitation methods such as hammer tests and falling weight devices. The literature reports that substructure components

dominate low frequencies, so a higher excitation of the substructure components is expected
and provides a better estimation of their condition. For substructure condition assessment,
a faster measurement speed is preferable in the design of KPIs for transition zones since it
provides more noticeable responses due to the higher excitation level than a slower speed,
particularly in the low-frequency range. Still, other track components are also more excited,
necessitating further studies for separating the responses from each track component, for
instance, from the subgrade, subballast, ballast, and sleepers.
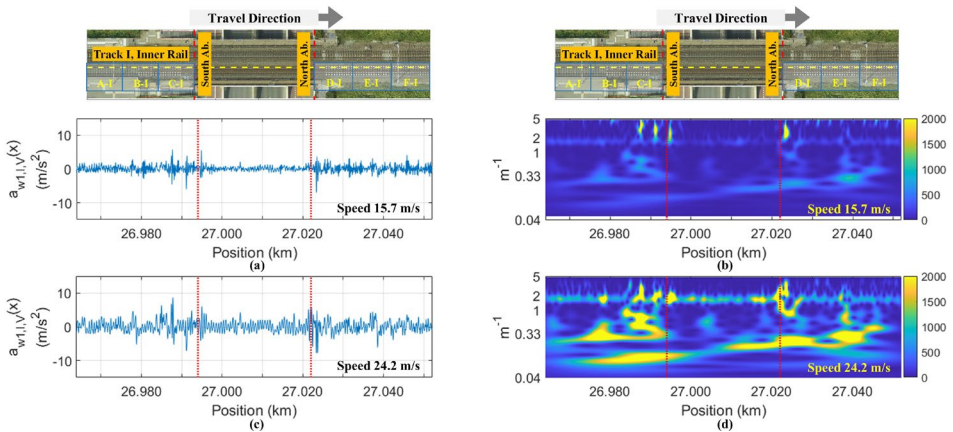

Figure 2.8: ABA responses (with 100 Hz cutoff frequency) at Bridge 3 in wheelset 1 on the inner
rail of Track I: (a) and (b) ABA and its WPS, measured at 15.7 m/s; and (c) and (d) ABA and its
WPS, measured at 24.2 m/s (source of aerial photographs: BBMS).
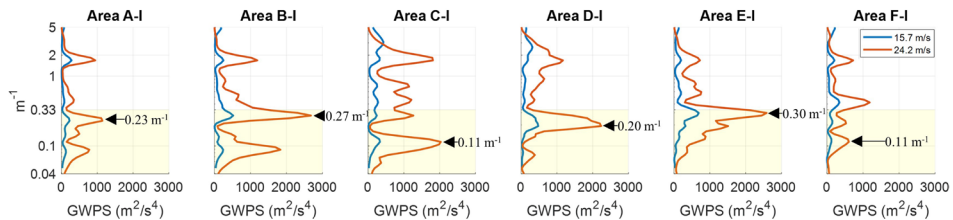
Figure 2.9: GWPS of ABA signals from two different measurement speeds at Bridge 3 in wheelset 1
on the inner rail of Track I.
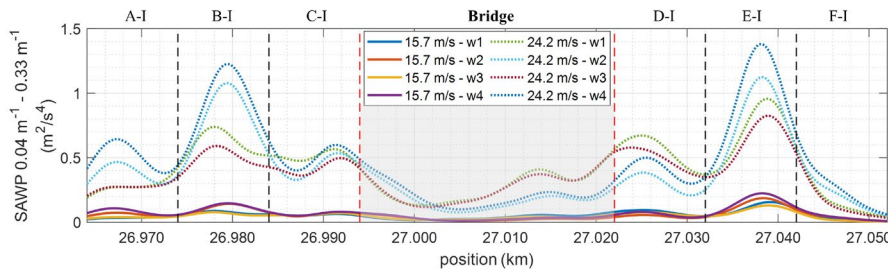
Figure 2.10: SAWP of the ABA signals from two different measurement speeds at Bridge 3 for the inner rail of Track I.

2.4. MULTI-ABA RESPONSES AT DIFFERENT TRACKS AND RAILS

The responses of multi-ABA signals measured at different tracks at the same bridge and different rails of the same track are investigated in this section. The multi-ABA signals measured at Bridge 6 are selected as an example since this bridge has the largest distance from other track components, such as insulated rail joints.

Additionally, signals with a minor difference in the measurement speeds between the two tracks are considered to reduce the speed effect on the analysis (as discussed in Section 2.3.2). Figure 2.11 presents multi-ABA signals from the inner rail (I) and outer rail (O) for Tracks I and II in the space domain and their WPS values. The train moved with a speed of 24.9 m/s on Track I and 25.7 m/s on Track II. The responses from each rail and track show different energy distributions over the frequency range of interest. In the following subsections, we analyze these differences.
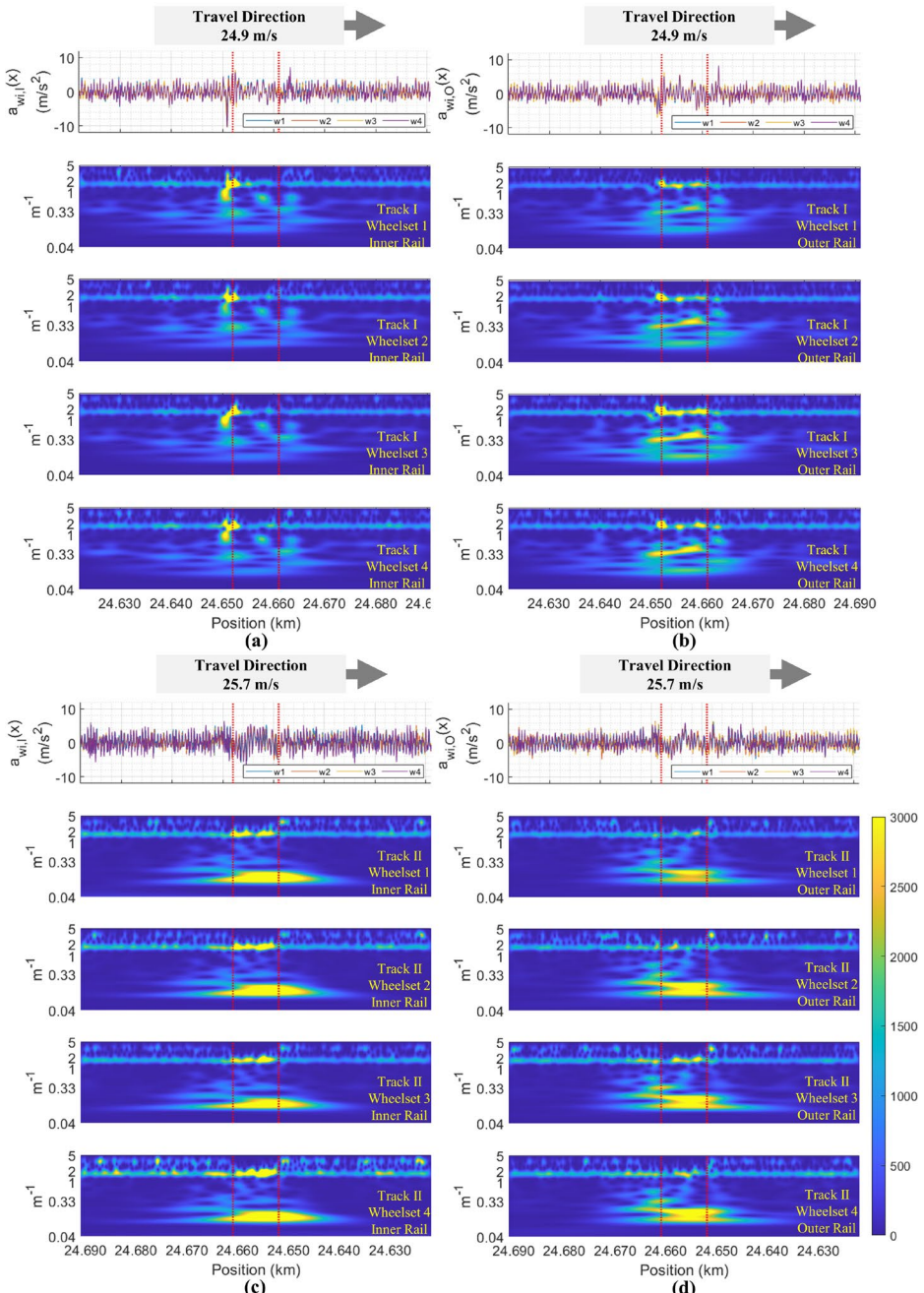
Figure 2.11: Multi-ABA signals (with 100 Hz cutoff frequency) and WPS at Bridge 6: (a) signals for the inner rail of Track I, (b) signals for the outer rail of Track I, (c) signals for the inner rail of Track II, and (d) signals for the outer rail of Track II.

2.4.1. RESPONSES OF MULTI-ABA SIGNALS FROM DIFFERENT TRACKS

The sum of the SAWP values measured from the inner rail and outer rail for each of the four wheelsets is considered to study degradation at the track level. Figure 2.12(a) and (b), for Tracks I and II, show the averaged SAWP values from the four wheelsets and the interval defined by the maximum and minimum SAWP values, respectively. The results show that Track I exhibits unsmooth energy changes, with dips at kilometer 24.630 in Area A-I, kilometer 24.644 in Area C-I, and kilometer 24.676 in Area E-I (see Figure 2.12(a)). The energy for Track II changes smoothly between consecutive study areas (see Figure 2.12(b)), with no significant dips in Area A-II, Area C-II, and Area E-II, as observed in Area A-I, Area C-I and Area E-I. We do not observe local changes in Track II at kilometer positions of 24.630, 24.644, and 24.676. Additionally, there are no visible track components in Track I that explain the differences with Track II based on observations from the aerial photograph.
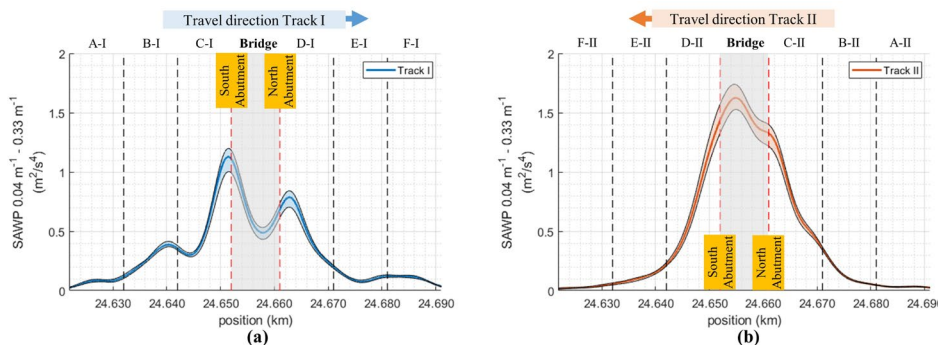
Figure 2.12: SAWP of the two tracks at Bridge 6: (a) responses at Track I; (b) responses at Track II.

Next, in Figure 2.13, the sum of SAWP values is used to quantify the amount of ABA energy in each study area. The results show that the sum of SAWP is higher for Track I in Areas A, B, and F. The ABA energy on the entrance side of Track I (Area C-I) is larger than that on the exit side (Area D-I) by 24.6%. Track II shows a smaller energy difference than Track I, for which the entrance side (Area C-II) energy is only 2.9% larger than that on the exit side (Area D-II). Figure 2.13(c) shows the percentage of energy change between two consecutive study areas. The maximum percentage of change for Track I is 275.4% from Areas A-I to Area B-I, while the maximum change for Track II is 571.9% from Area B-II

to Area C-II. This finding suggests that the track components whose response is reflected in the range 0.04 m^{-1} – 0.33 m^{-1} (dominant by substructure) in the studied transition zones for Track I and Track II are dissimilar. Further studies are needed to understand better the relation between the operational condition of the transition zones, multi-ABA signals, track geometry differences, and malfunctions at the track structure.
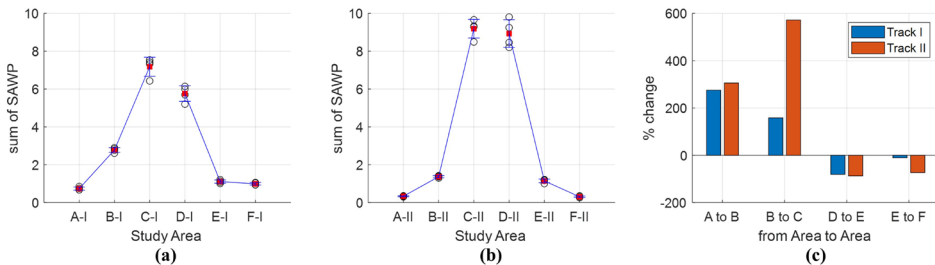
Figure 2.13: Sum of SAWP values for different areas of Bridge 6: (a) study areas on Track I; (b) study areas on Track II; and (c) percentage of change between the study areas.

To compare abutments, the ABA energies in Areas C-I and D-II are summed to represent the conditions of the track segment near the South Abutment, which gives a value of 16.11 m^2/s^4. The sum of the ABA energy in Areas D-I and C-II represents the track segment near the North Abutment and is approximately 14.95 m^2/s^4. This calculation suggests that the South Abutment exhibits approximately 7.8% higher energy than the North Abutment. Additional onsite investigations can provide a better understanding of these differences. For instance, a structural settlement or damages could be the possible reason to explain larger differences. Finally, when analyzing various bridges, the condition variation of the substructure at transition zones on the abutment level and track level is relatively local; for instance, the stronger degradation process of transition zones is not always located at the entrance side.

2.4.2. RESPONSES OF MULTI-ABA SIGNALS FROM DIFFERENT RAILS

This section analyzes ABA signals from the inner rail (I) and outer rail (O). We use measurements from wheelset 1 in Bridge 6 as an example. Figure 2.14(a) and (b) present the responses of the inner rail, while Figure 2.14(c) and (d) show the outer rail responses. The ABA signals from the inner and outer rails yield similar peak positions (see blocks 1, 2, 3, and 4 in Figure 2.14). However, the inner rail signal shows a significantly larger

amplitude than the outer rail signal at a peak close to the South Abutment. This suggests that at Track I, the South Abutment experiences a stronger uneven degradation than the North Abutment. Consequently, the WPS values of the inner rail close to the South Abutment are significantly larger than those from the outer rail (see blocks 5 and 7).
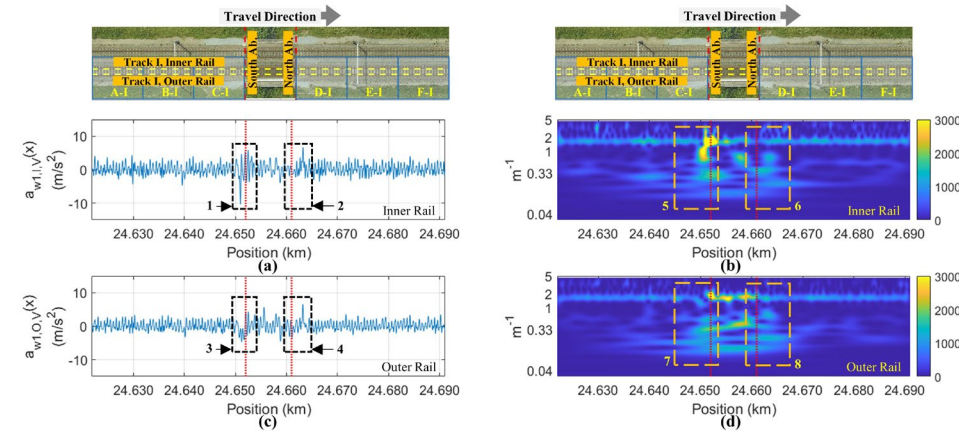
Figure 2.14: ABA responses (with 100 Hz cutoff frequency) of Track I at Bridge 6: (a), (b) responses of the inner rail in the space domain and WPS; and (c), (d) responses of the outer rail in the space domain and WPS (source of aerial photographs: BBMS, ProRail).

Multi-ABA signals from both rails in terms of the GWPS values in each study area are compared in Figure 2.15. Signals from the inner and outer rails show differences in the frequencies and amplitudes of the dominant peaks in the study areas. Areas C-I and D-I show noticeable response differences between the two rails in the spatial frequency range below 0.33 m^{-1} (see yellow regions). In addition, remarkable differences between the two rails are also found at spatial frequencies above 0.33 m^{-1} (see, for example, Area C-I). Even though the responses above 0.33 m^{-1} are not within the scope of this study, this finding could be indicative of transition zone health conditions related to the deterioration of sleepers, such as hanging sleepers. Hence, further studies are needed for a better understanding.

Next, the SAWP values of the signals at both rails in Tracks I and II and the corresponding track geometry parameters at the transition zones are shown in Figure 2.16. Figure 2.16(a) shows noticeable differences in Areas B-I, C-I, and D-I regarding the location and amplitude of the SAWP peak responses between the inner and outer rails. The

inner rail shows larger energies than the outer rail in Area B-I, while the outer rail shows larger energies in Areas C-I and D-I. The responses of Track II in Figure 2.16(b) show significantly different responses in Area C-II (outer rail with higher energy) and Area D-II (inner rail with higher energy). These findings suggest a sensitivity of the multi-ABA to estimate responses from signals measured at different rails. Slight amplitude variations and similar peaks and wave behavior can be observed. A possible reason to explain this higher spatial resolution is that the multi-ABA measures 25,600 times in a second (or every 1.5 mm) when the measurement speed is 140 km/h. In the case of a conventional track geometry recording car, the signals are reported every 25 cm.
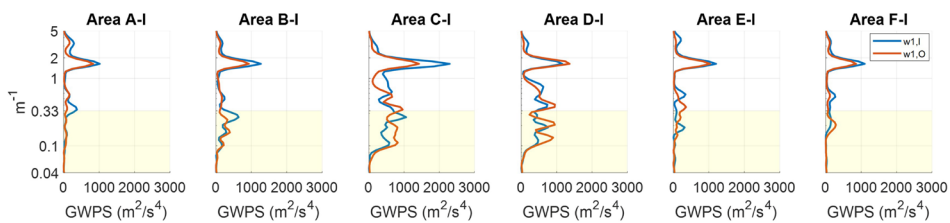
Figure 2.15: GWPS of the ABA signals measured at different rails for Track I at Bridge 6.

Although the ABA measurement system can detect differences in ABA energy between 2 rails, current substructure remedies in practice, for instance, ballast tamping and subgrade strengthening, are mainly conducted underneath two rails simultaneously. Nevertheless, this detection capability might provide indications to support track substructure maintenance solutions at specific spots with next-generation technology. Furthermore, numerical simulations of the transition zones can be developed and fine-tuned to reproduce this effect, and then we can expect a better understanding of the track parameters. Furthermore, we found a considerable variation in track geometry parameters, especially in Area C and Area D on both tracks, where the SAWPs also vary significantly. This finding might relate to the reported relationship between the longitudinal level and the track substructure conditions [118,129–133]. Since in this chapter, we consider the various layers of the substructure as a whole, a determination of the severity level of each layer is required for a more detailed maintenance planning. Therefore, further studies could support a better understanding of the relationship between ABA signals and track geometry parameters, making track substructure condition assessment more informative and insightful.
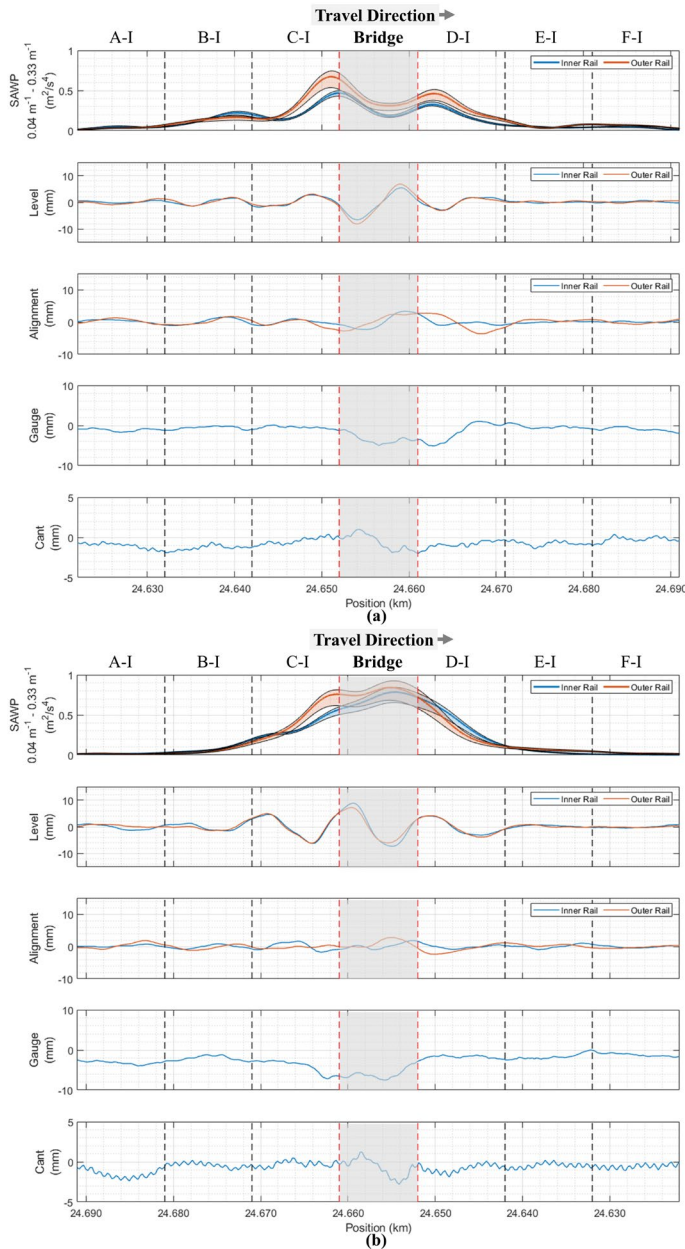
Figure 2.16: SAWP of the ABA signals and track geometries at Bridge 6:
(a) measurement for Track I and (b) measurement for Track II.

2.5. KEY PERFORMANCE INDICATORS BASED ON THE MULTI-ABA FOR TRANSITION ZONES

This section proposes a methodology for continuously monitoring the degradation levels of transition zones using KPIs based on multi-ABA measurements. Previous studies reported that more severe degradation levels of track components provide larger ABA energies [112,113]. Assuming that an undegraded condition has the lowest percentage of energy contents, a large difference between the energy contents of the two transition zones indicates that the transition zone with high energy content should have a more severe degradation. Therefore, the relative percentage difference of the energy content is proposed as an indicator of transition zone health conditions. Thus, ABA energy-based KPIs are developed to evaluate differences between transition zones using SAWP. At a particular bridge, four KPI types are proposed in this chapter to represent an ABA energy comparison of transition zones at different abutments (North and South), tracks (I and II), sides (entrance and exit), and rails (inner and outer). A brief description of a particular KPI is shown in Table 2.2.

Table 2.2: Description of the proposed KPIs

KPIs	Description
$\text{KPI}_b^{\text{abutment}}$	Relative energy difference between the South and North Abutments at bridge b.
$\text{KPI}_{b,a}^{\text{track}}$	Relative energy difference between 2 tracks that is associated with abutment a (either the South or the North Abutment) of bridge b.
$\text{KPI}_{b,t}^{\text{side}}$	Relative energy difference between the entrance and exit sides of track t (either Track I or Track II) of bridge b.
$\text{KPI}_{b,s,t}^{\text{rail}}$	Relative energy difference between the inner and outer rails of side s (either the entrance side or exit side) of track t of bridge b.

The previous sections discussed that the ABA energy is highly location- and speed-dependent, so measurements with minor speed differences between Tracks I and II are selected.

2.5.1. KPI FOR ABUTMENTS

As discussed in Section 2.4.1, the SAWP sum at Area C-I of Track I and Area D-II of Track II can be used to represent the condition of track segments associated with the South

Abutment, while the SAWP sum at Areas D-I and C-II can be used to represent track segments that correspond to the North Abutment. Therefore, a KPI for evaluating differences in degradation level between abutments is proposed as follows:

$$\text{KPI}_b^{\text{abutment}} = \frac{\left(\sum_{x=x_3}^{x_4} \overline{SAWP}_b^{\text{Track I}}(x) + \sum_{x=x_3}^{x_4} \overline{SAWP}_b^{\text{Track II}}(x)\right) - \left(\sum_{x=x_1}^{x_2} \overline{SAWP}_b^{\text{Track I}}(x) + \sum_{x=x_1}^{x_2} \overline{SAWP}_b^{\text{Track II}}(x)\right)}{\dfrac{\left(\sum_{x=x_3}^{x_4} \overline{SAWP}_b^{\text{Track I}}(x) + \sum_{x=x_3}^{x_4} \overline{SAWP}_b^{\text{Track II}}(x)\right) + \left(\sum_{x=x_1}^{x_2} \overline{SAWP}_b^{\text{Track I}}(x) + \sum_{x=x_1}^{x_2} \overline{SAWP}_b^{\text{Track II}}(x)\right)}{2}} \times 100 \qquad \text{Eq. 2.6}$$

where b is the bridge number, $\sum_{x=x_m}^{x_n} \overline{SAWP}_b^{\text{location}}(x)$ is the ABA energy at a considered location from kilometer x_m to x_n, $\overline{SAWP}_b(x)$ is an averaged SAWP from 4 wheelsets, x_1 and x_2 are kilometer positions defining the South Abutment (Areas C-I and D-II), and x_3 and x_4 define the North Abutment (Areas C-II and D-I). According to Eq. 2.6, a negative $\text{KPI}_b^{\text{abutment}}$ indicates that the transition zones associated with the South Abutment are more degraded, and a positive $\text{KPI}_b^{\text{abutment}}$ indicates that the transition zones associated with the North Abutment are more degraded. Values of approximately 0% represent cases when the ABA energy contents (as associated with degradation conditions) between the transition zones at the South and North Abutments are similar.

Figure 2.17(a) shows the partition of the total ABA energy content between the South and North Abutments, and Figure 2.17(b) shows $\text{KPI}_b^{\text{abutment}}$. The KPI ranges from -79.7% to 92.4% for the bridges in the case study. In 4 out of 9 bridges (bridges 1, 3, 4, and 8), more severe degradation occurs at the North Abutment. Furthermore, three bridges indicate a considerable difference, approximately 80.0%: $\text{KPI}_2^{\text{abutment}}$ is -79.4%, $\text{KPI}_3^{\text{abutment}}$ is 92.4% and $\text{KPI}_4^{\text{abutment}}$ is 78.0%. Finally, Figure 2.17(a) and (b) show that the degradation level of the track segments associated with two abutments can vary and that each bridge exhibits individual degradation characteristics reflected by the KPI.

2.5.2. KPI FOR TRACKS

At a particular abutment, we define a KPI that estimates the difference in the ABA energy between different tracks. This KPI is defined as follows:

$$\text{KPI}_{b,a}^{\text{track}} = \frac{\sum_{x=x_m}^{x_n} \overline{SAWP}_{b,a}^{\text{Track II}}(x) - \sum_{x=x_m}^{x_n} \overline{SAWP}_{b,a}^{\text{Track I}}(x)}{\frac{\sum_{x=x_m}^{x_n} \overline{SAWP}_{b,a}^{\text{Track II}}(x) + \sum_{x=x_m}^{x_n} \overline{SAWP}_{b,a}^{\text{Track I}}(x)}{2}} \times 100 \qquad \text{Eq. 2.7}$$

where b is the bridge number, a is abutment, either S (South) or N (North), $\sum_{x=x_m}^{x_n} \overline{SAWP}_{b,a}^{\text{location}}(x)$ is the ABA energy from kilometer x_m to x_n at Abutment a, and $\overline{SAWP}_{b,a}(x)$ is an averaged SAWP from 4 wheelsets. According to Eq. 2.7, at any abutment, positive value of $\text{KPI}_{b,a}^{\text{track}}$ indicates that Track II is degraded more, and negative $\text{KPI}_{b,a}^{\text{track}}$ indicates that Track I is degraded more. Values of approximately 0% suggest that both tracks have a similar degradation condition at the abutment.

Figure 2.17(c) shows the partition of total ABA energy content between Tracks I and II for each abutment in the case study. These results show that the ABA energy is distributed differently at each abutment. Figure 2.17(d) shows $\text{KPI}_{b,a}^{\text{track}}$ for all the abutments of the case study. The results from 18 abutments show that positive KPI values are found in 11 abutments (in the ranges from 3.7% to 148.6%), and negative values in 7 abutments are found (from -17.9% to -111.3%). Moreover, 2 out of 18 abutments provide the highest differences between tracks (higher than 100.0%). The North Abutment of Bridge 3 exhibits a higher degradation of Track II, and the North Abutment of Bridge 7 shows a higher degradation of Track I.

2.5.3. KPI FOR THE EXIT AND ENTRANCE SIDES

A KPI is designed to quantify the degradation differences between the entrance side at Area C and the exit side at Area D of a particular track. This KPI for evaluating differences between the exit and entrance sides of a track is:

$$
\text{KPI}_{b,t}^{\text{side}} = \frac{\left(\sum_{x=x_3}^{x_4} \overline{SAWP}_{b,t}^{\text{exit}}(x) - \sum_{x=x_1}^{x_2} \overline{SAWP}_{b,t}^{\text{entrance}}(x) \right)}{\dfrac{\left(\sum_{x=x_3}^{x_4} \overline{SAWP}_{b,t}^{\text{exit}}(x) + \sum_{x=x_1}^{x_2} \overline{SAWP}_{b,t}^{\text{entrance}}(x) \right)}{2}} \times 100
\qquad \text{Eq. 2.8}
$$

where b is the bridge number, t is either I or II referring to Track I or Track II, respectively, $\sum_{x=x_m}^{x_n} \overline{SAWP}_{b,t}^{\text{location}}(x)$ is the ABA energy at a considered location from kilometer x_m to x_n, $\overline{SAWP}_{b,t}(x)$ is an averaged SAWP from 4 wheelsets, x_1 and x_2 are the kilometer positions of the entrance side (Area C), and x_3 and x_4 are the kilometer positions of the exit side (Area D). According to Eq. 2.8, a negative $\text{KPI}_{b,t}^{\text{side}}$ indicates that the entrance side is degraded more, and a positive $\text{KPI}_{b,t}^{\text{side}}$ indicates that the exit side is degraded more. Values near 0% indicate similar degradation conditions on both sides.

Figure 2.17(e) shows the partition of total ABA energy between the entrance and exit sides, and Figure 2.17(f) shows $\text{KPI}_{b,t}^{\text{side}}$ for all the case study locations. In 7 cases, the exit side is more degraded, with KPI values ranging from 5.5% to 97.0%. In 11 cases, the entrance side is more degraded, with KPI values from -2.9% to -115.3%. Finally, Track II of Bridge 2 shows the highest positive value (97.0%), and Track II of Bridge 3 and Track II of Bridge 4 provide the most negative values (-115.3% and -99.0%, respectively). Figure 2.17(e) and (f) indicate that the degradation severity is related to the local condition of the track.

Figure 2.18 shows aerial photographs taken in 2019 and site-visit photographs taken in 2021 at Track II of Bridge 3, which has the highest negative KPI value. The photographs show remarkable differences in the ballast appearance at the entrance side of Track II, especially in Areas B-II and C-II. The site-visit photograph shows that some new ballast has been placed. The images suggest that the area has required various maintenance interventions in the last few years. The KPI suggests that the problem is substructure-related.
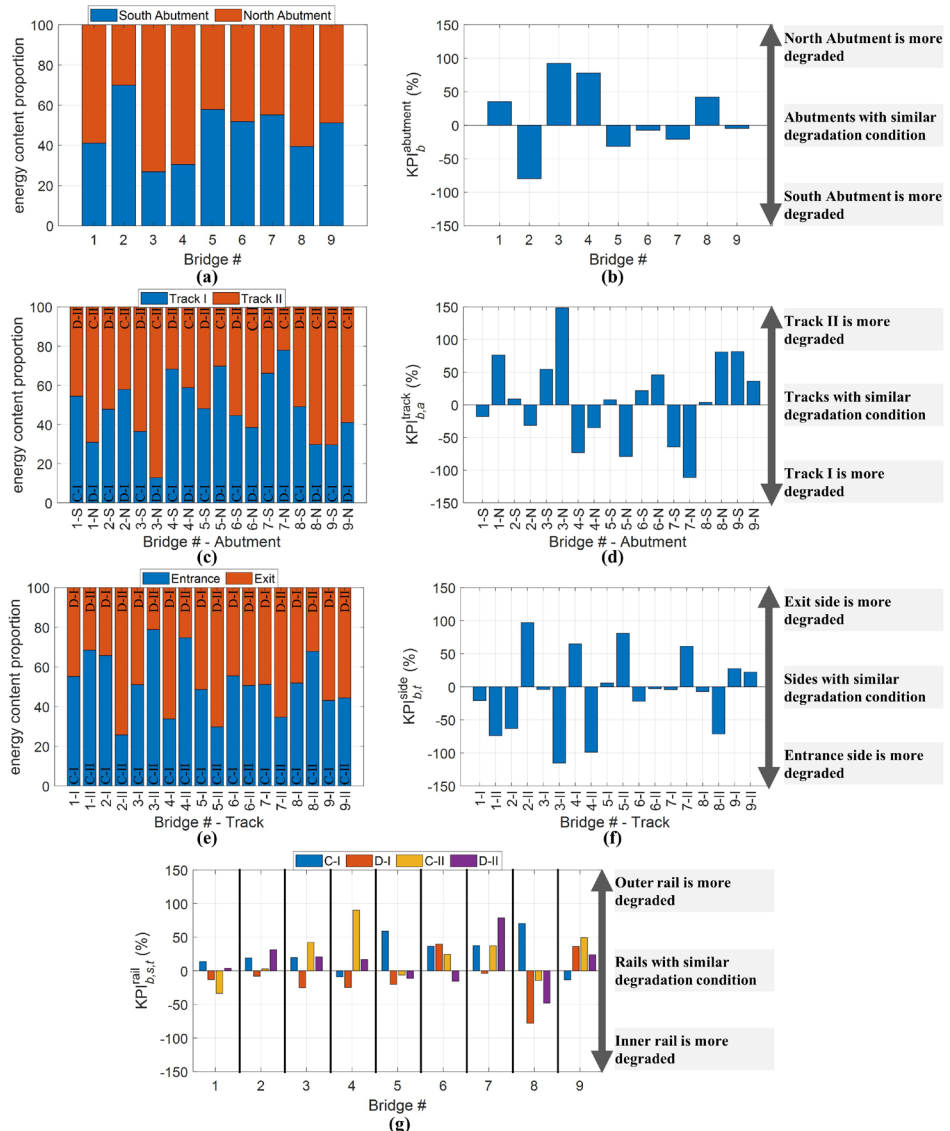
Figure 2.17: Degradation level evaluation at different locations of transition zones: (a), (c), (e) partition of total energy content between the two abutments, two tracks at a particular abutment, two sides at a particular track; (b), (d), (f), (g) KPI to evaluate substructure condition differences between abutments, tracks, sides, and rails.
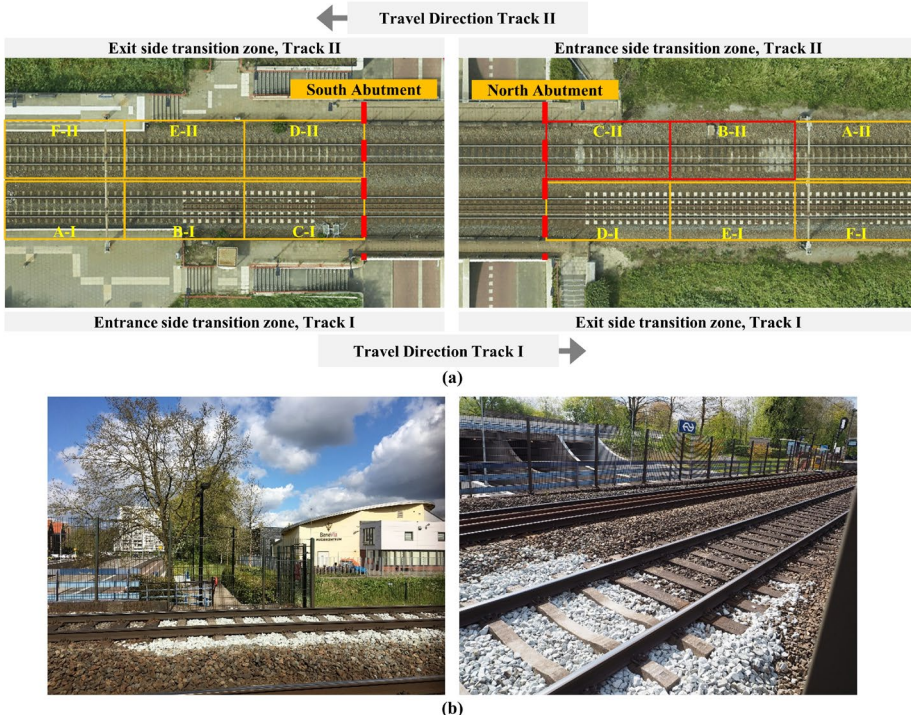
Figure 2.18: Photos of Bridge 3: (a) aerial photographs, where the red rectangle indicates the different appearances of ballast at the entrance site of Track II; (b) site visit photographs taken at the entrance side of Track II (source of aerial photographs: BBMS).

2.5.4. KPI FOR INNER AND OUTER RAILS

Following the discussion in Section 2.4.2, we propose quantifying the local differences between the inner and outer rails at the transition zones of each bridge, side, and track. This KPI is defined as follows:

$$
\text{KPI}_{b,s,t}^{\text{rail}} = \frac{\left(\sum_{x=x_m}^{x_n} \overline{SAWP}_{b,s,t}^{\text{outer}}(x) - \sum_{x=x_m}^{x_n} \overline{SAWP}_{b,s,t}^{\text{inner}}(x) \right)}{\dfrac{\left(\sum_{x=x_m}^{x_n} \overline{SAWP}_{b,s,t}^{\text{outer}}(x) + \sum_{x=x_m}^{x_n} \overline{SAWP}_{b,s,t}^{\text{inner}}(x) \right)}{2}} \times 100 \qquad \text{Eq. 2.9}
$$

where b is the bridge number, s is either C or D referring to Area C (entrance area) or Area D (exit area), respectively, t is either I or II referring to Track I or Track II, respectively,

$\sum_{x=x_m}^{x_n} \overline{SAWP}_{b,s,t}^{\text{location}}(x)$ is the ABA energy at a considered location from kilometer x_m to x_n, and

$\overline{SAWP}_{b,s,t}^{r}(x)$ is an averaged SAWP from 4 wheelsets, where r is either the inner or outer rail. According to Eq. 2.9, $\text{KPI}_{b,s,t}^{\text{rail}}$ is negative when the signals suggest greater degradation of the inner rail, and $\text{KPI}_{b,s,t}^{\text{rail}}$ is positive for greater degradation of the outer rail.

Figure 2.17(g) shows $\text{KPI}_{b,s,t}^{\text{rail}}$ for the case study. In 21 out of 36 sides, a positive KPI value from 2.8% to 90.2% is found, indicating that ABA signals from the inner rail suggest a less severe degradation than in the outer rail. In the remaining 15 tracks, negative KPI values from -4.0% to -78.1% indicate a higher degradation from the inner rail signals. Furthermore, most of the differences range from -40.0% to 40.0%, with only three cases providing considerable differences of approximately 80.0% or higher. The entrance side at Track II of Bridge 4 and the exit side at Track II of Bridge 7 show the most positive KPI values of 90.2% and 78.8%, respectively. The exit side at Track I of Bridge 8 provides the most negative KPI value at -78.1%.

The finding shows that the degradation differences between the two rails are not detectable in most cases. Regarding the findings of this section, the locations that show higher degradation levels could be further investigated to identify the causes and effects on the performance of the transition zones. Consequently, tailored maintenance planning with suitable track remedies can be performed at those specific locations.

2.6. EVOLUTION OF KPIS OVER TIME

This section analyzes the evolution of the KPIs over time at transition zones. The datasets of ABA signals from measurement campaigns in 2016, 2019 (the dataset used in Section 2.5), and 2022 are used as primary inputs for this analysis. Since track maintenance records are unavailable, we use the track geometry parameters from 2016 – 2022 to calculate the track quality index. In this chapter, we use combined standard deviation (CoSD), according to EN 13848-6, which is proposed as follows:

$$CoSD = \sqrt{w_{\overline{\text{AL}}}SD_{\overline{\text{AL}}}^2 + w_{\text{G}}SD_{\text{G}}^2 + w_{\text{CL}}SD_{\text{CL}}^2 + w_{\overline{\text{LL}}}SD_{\overline{\text{LL}}}^2} \qquad \text{Eq. 2.10}$$

where $SD_{\overline{AL}}$ is the standard deviation of the alignment, average from the inner and outer rails, SD_G is the standard deviation of the track gauge, SD_{CL} is the standard deviation of the cross level, $SD_{\overline{LL}}$ is the standard deviation of the longitudinal level, average from the inner and outer rail, and w_i is the weighting factor of the individual geometry parameter i (set in this chapter at 0.25 for each parameter). Since the data over time for Bridge 9 is unavailable, the analysis in this section considers Bridges 1 to 8. Figure 2.19 shows the variation of track quality in terms of CoSD over time. The track quality of the transition zone at Bridge 3 on Track II at the entrance side significantly dropped from 2020 to 2021. This finding agrees with observations from track visits in 2021, indicating that new ballast was placed, as shown in Figure 2.18.
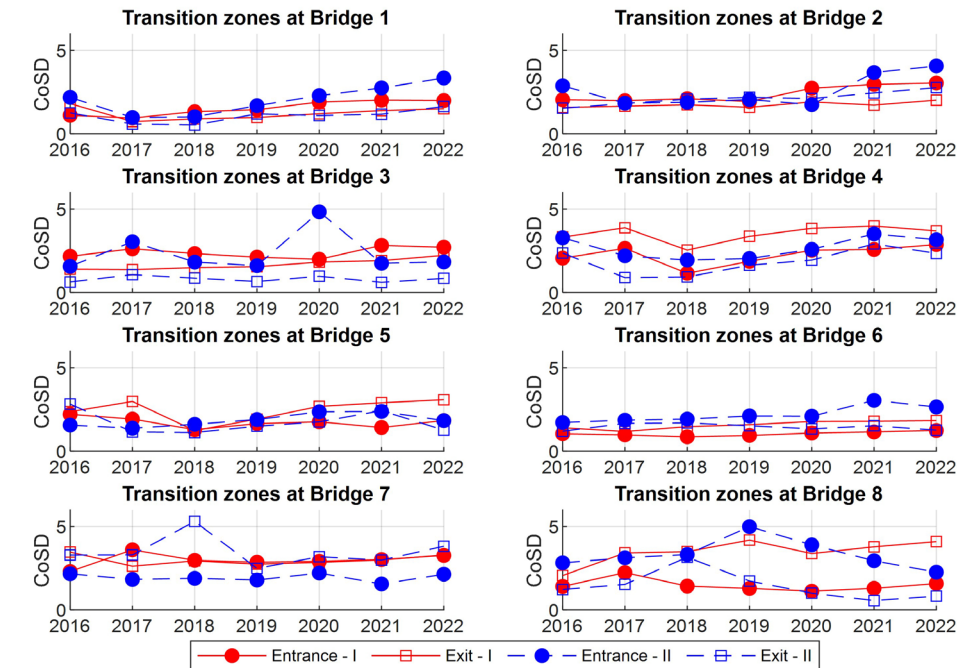

Figure 2.19: Track quality at transition zones from 2016 to 2022.

The ABA energy is speed-dependent, and there are differences in the measurement speed between years at a particular transition zone, as shown in Figure 2.20. To examine the usefulness of the sum of SAWPs as a KPI input, we selected transition zones at Bridge

4, Track I, since this location was measured with the most similar speeds between years (with differences ranging from 0.1 m/s to 1.3 m/s).
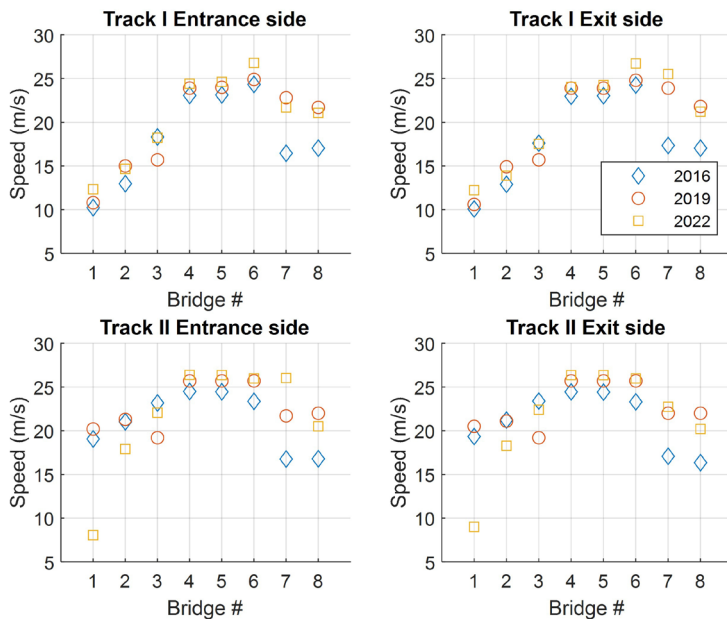

Figure 2.20: Speed differences at a particular transition.

Figure 2.21(a) shows the SAWP evolution over time. Then, the sum of SAWPs at zones C and D are calculated and shown in Figure 2.21(b) and (c), respectively. The results show that the conditions of both transition zones at the entrance and exit sides in 2016 were more degraded than in 2019 since a lower measurement speed provided higher ABA energy. The measurement speed in 2019 is 3.91% higher than the speed in 2016, while ABA energy in 2019 of the entrance and exit sides is lower than in 2016 by 43.83% and 45.74%, respectively. This finding is consistent with the change in track quality over time, as shown in Figure 2.19, since indications of maintenance activities appeared in 2018. With the same criteria, we can conclude that transition zone conditions in 2022 were more degraded than in 2016 and 2019 because of a higher ABA energy. Note that the speed in 2022 is slightly higher than in previous years. The measurement speed in 2022 is 5.22% higher than in 2016 and 1.25% higher than in 2019. For the entrance side, the ABA energy in 2022 is 168.50% higher than in 2016 and 378.04% higher than in 2019. For the exit side, the ABA energy in 2022 is 24.09% higher than in 2016 and 128.69% higher than in 2019.
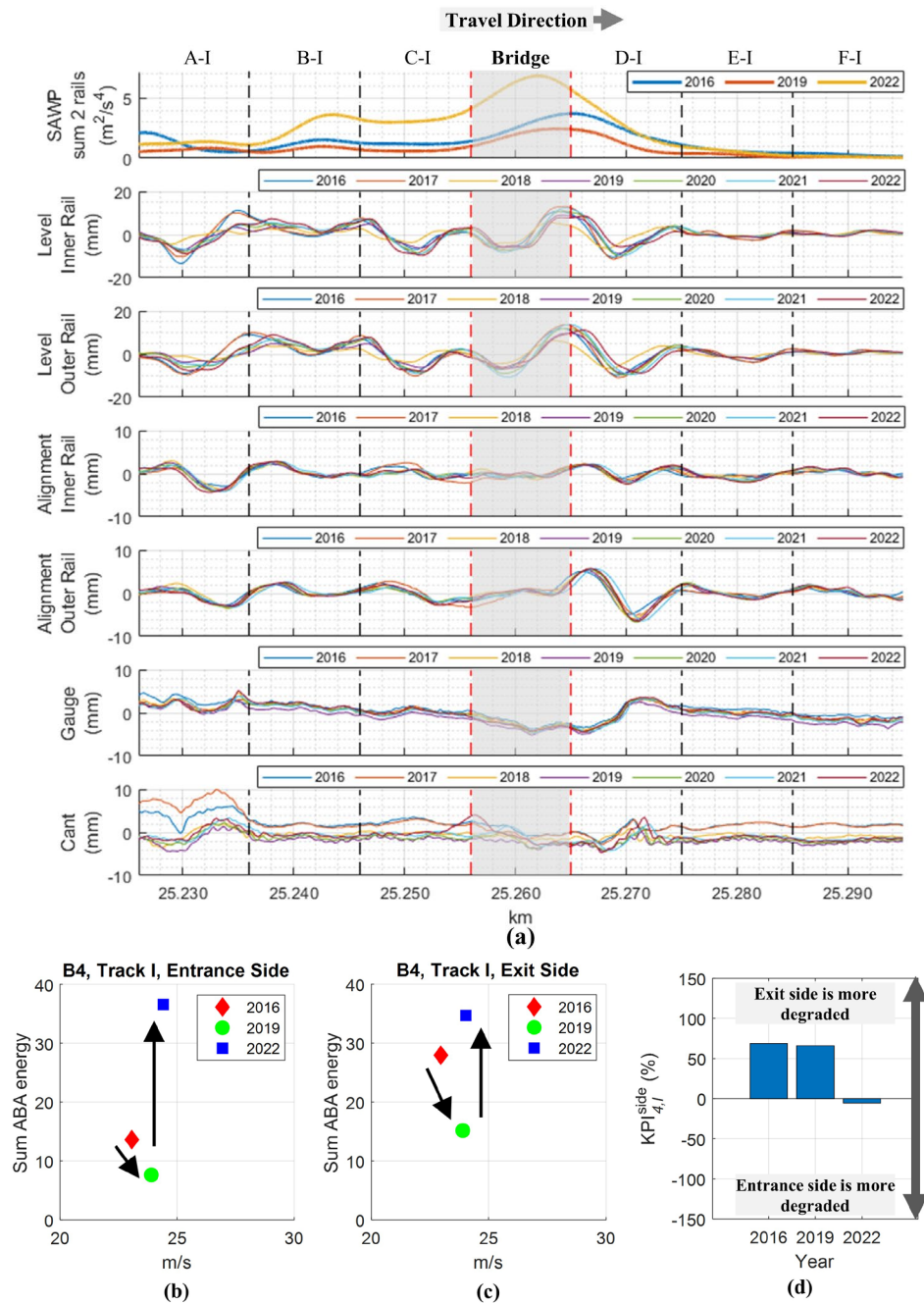
Figure 2.21: Evolution of transition zones degradation at Bridge 4, Track I: (a) SAWP curves and track geometry parameters over time; (b),(c) comparison of ABA energy at entrance side and exit side transition zones; (d) KPI to evaluate condition differences between sides.

Figure 2.21(d) shows the KPI for the entrance and exit side transition zones at bridge 4 ($KPI_{4,t}^{side}$). In 2016, the transition zone on the exit side was 69% more degraded than that of the entrance side. Then, this difference decreased to 66% in 2019, and finally, the entrance side transition zone was 5.4% more degraded than the exit side one in 2022. This finding suggests that the proposed KPI can represent the degradation evolution of transition zones.

Figure 2.22 shows $KPI_{b,t}^{side}$ over time. The most dramatic change in the health condition, a 121.5% increase, occurred at transition zones at Bridge 2, Track II. The exit side transition zone was more degraded than the entrance side by 99.0% in 2019. Then, in 2022, the transition zone at the entrance side was more degraded than the exit side by 22.5%. In contrast, a minor change, 1.7%, occurred at the transition zones at Bridge 4, Track I. Additional sources of measurement data and onsite investigations are needed for a better understanding of the degradation mechanism of transition zones and to relate KPIs with malfunction causes.
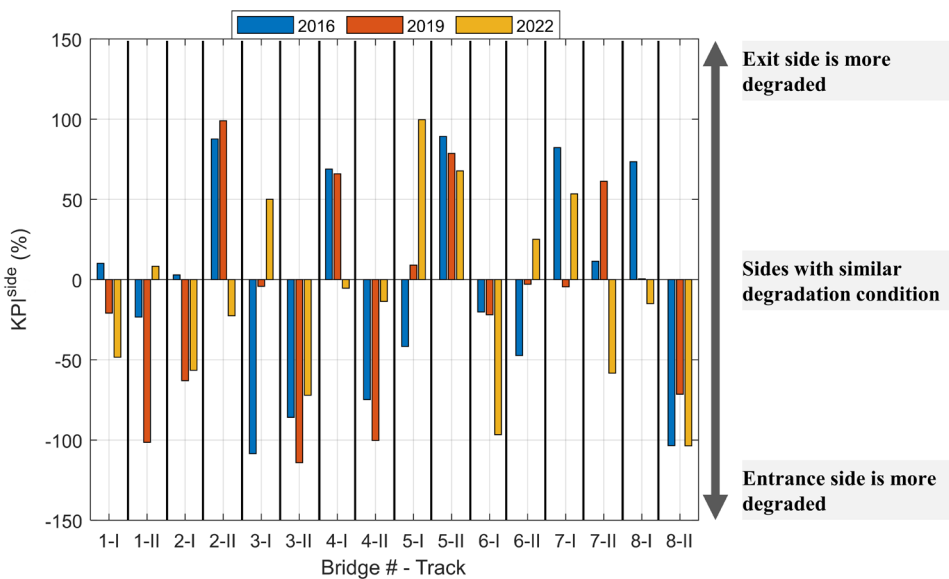

Figure 2.22: KPI to evaluate substructure condition differences between sides from different measurement years.

Another KPI that can be evaluated for transition zones is by considering the vibration acceleration level (VAL), defined as [134]:

$$VAL\left(f_i\right) = 20\log_{10}\left(\frac{a\left(f_i\right)}{a_0}\right)$$

<div style="text-align:right">Eq. 2.11</div>

where $a(f_i)$ is the root mean square of the acceleration at the 1/3 octave band center frequency f_i, a_0 is the reference acceleration, which is 10^{-6} m/s^2.

In this chapter, when calculating the VAL at a specific section, the ABA signals are considered on the track level, including two rails. The VAL at the conventional track (30 m before the entrance transition zone) and at the entrance side transition zone (30 m before the entrance abutment) of Bridge 6 is shown as an example in Figure 2.23. The results show that in the considered spatial frequency range of 0.04 m^{-1} to 0.33 m^{-1} (substructure-related), the VAL of the conventional track is about 100 dB or lower, which is significantly lower than the level of the transition zone where the VAL is in between 100 dB and 110 dB. According to the VAL, the example transition zone provides a vibration 10 times higher than the nearby conventional track. This finding agrees with the 1/3 octave band spectra of the longitudinal level in Figure 2.24. The transition zone provides substructure-related geometry variance 10 times higher than the conventional track. The VAL of the longitudinal level of the conventional track is in the range of $100 - 110$ dB, while that of the transition zone is in the range of $110 - 120$ dB.

The above-mentioned finding supports that the VAL (1/3 octave band spectra) can also be adopted as a KPI. Figure 2.24 shows the evolution of VAL at the entrance transition zone of Bridge 4 (same bridge as in Figure 2.21). The finding shows that the condition in 2022 is more severe than in 2016 and 2019 since the VAL amplitudes in the substructure-related ranges are higher than in other years. The findings from VAL show good agreement with the analysis results from the SAWP quantity, as shown in Figure 2.21.
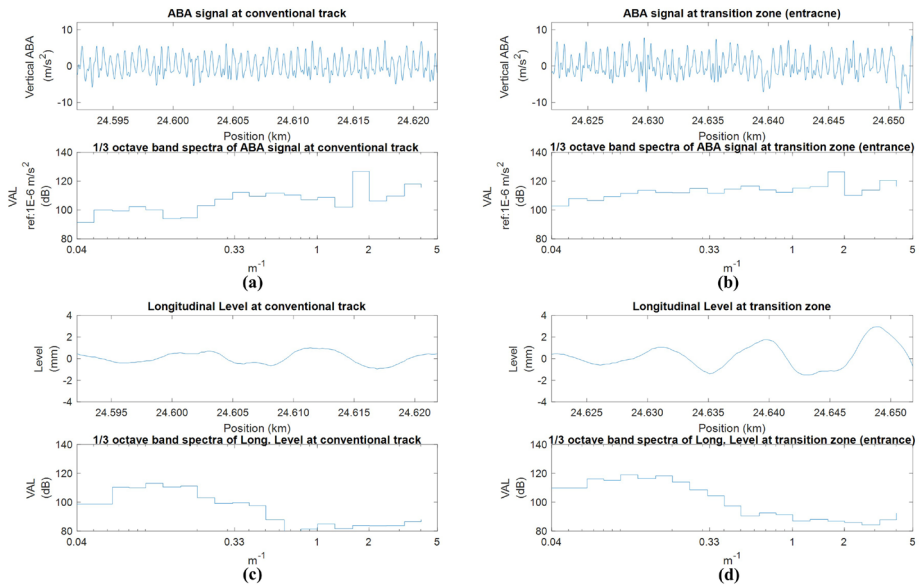
Figure 2.23: Comparison of ABA and the longitudinal level response at the location nearby Bridge 6 in the time domain and the VAL (1/3 octave band): (a) ABA signal at the conventional track; (b) ABA signal at the entrance transition zone; (c) the longitudinal level at the conventional track; (d) the longitudinal level at the entrance transition zone
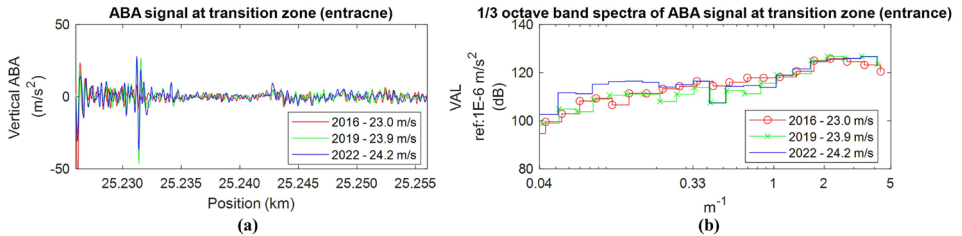
Figure 2.24: Evolution of the entrance transition zone from 2016, 2019, and 2022: (a) ABA signals in the time domain; (b) the *VAL* of ABA signals.

Figure 2.25 shows that the 1/3 octave band, PSD, and GWPS provide similar information on the distribution of ABA energy in the frequency domain. Since ABA signals are non-stationary, the frequency domain quantities have drawbacks that they cannot provide specific locations with local changes or defects. Therefore, we use Wavelet transform and calculate SAWP, then develop KPIs derived from SAWP for transition zone condition assessment for this chapter. The use of the 1/3 octave band is complementary and

provides a good overview of the energy signals that can be used to analyze responses at the whole network-level.
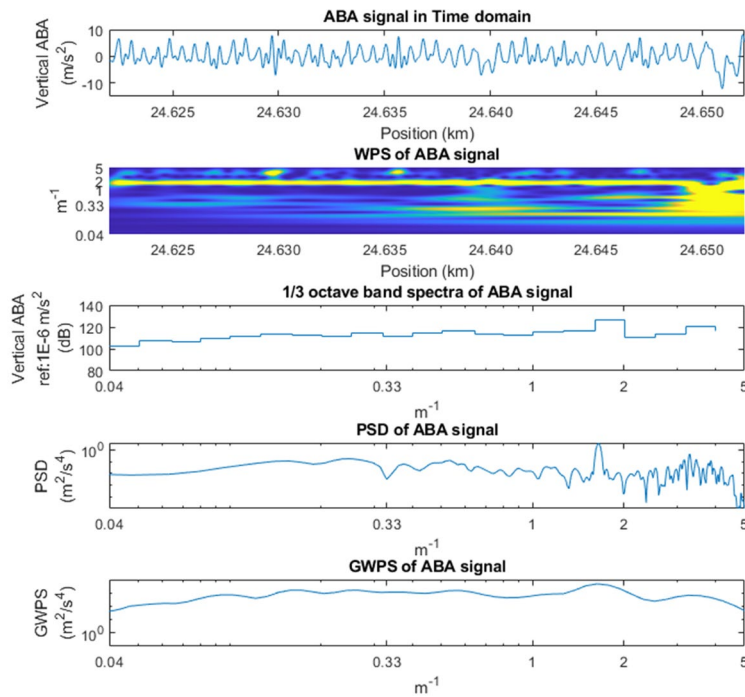
Figure 2.25: ABA signal response in the frequency domain according to 3 different quantities at the entrance transition zone, Bridge 6.

2.7. CONCLUSIONS

This chapter proposes the design of KPIs for monitoring transition zones using multi-ABA measurements. The case study considers transition zones at railway bridges; however, the proposed KPI methodology can apply not only to the Dutch railway network where the soils are very soft, but also to monitor other railway lines and other types of transition zones between soil and rigid structures. Based on the analyses, the following conclusions can be drawn:

1. A multi-ABA measurement system is promising for transition zone condition monitoring. Different transition zones show differences in ABA responses. From the analysis of such responses, the health condition of transition zones can

potentially be evaluated using in-service trains with frequent and continuous measurements.

2. The measurement speed influences multi-ABA responses. A measurement at a higher speed yields more prominent ABA responses at a particular location due to the higher excitation level in the low-frequency range, which helps distinguish the responses related to substructure conditions. Additionally, ABA responses vary when collected from different trains or with the same trains under different operational conditions. This factor must be considered when deriving KPIs from operational trains with different characteristics.

3. For the considered spatial frequency range from 0.04 m^{-1} to 0.33 m^{-1}, the particular transition zones at each bridge exhibit different characteristics. These distributed characteristics pertain to each part of the transition zones and their health condition status.

4. ABA energy-based KPIs allow the assessment of different degradation levels of transition zones from the large-scale level to the small-scale level, i.e., between different abutments of a particular bridge, between different tracks of a particular abutment, between different sides of a particular track, and between rails of a particular side.

5. According to the case study, the locations with the highest degradation do not always occur at a specific abutment (North or South), track (Track I or II), side (entrance or exit), or rail (inner or outer). Further investigations at those locations could provide a better understanding of the degradation mechanisms at transition zones.

6. The KPIs from different measurement years correlate with the track geometry-based quality index. Still, we observed locations where track geometry did not show important variations while ABA indicated stronger responses. The higher resolution of ABA might explain this (one measurement every 1.5 mm with 140 km/h measurement speed) compared to the track geometry measurement method (25 cm).

3

FRAMEWORK FOR THE PHYSICAL INTERPRETATION OF ABA SIGNAL

This chapter presents a measuring framework for railway transition zones using a case study on the Swedish line between Boden and Murjek. The final goal is to better understand the vertical dynamics of transition zones using hammer tests, falling weight measurements, and axle box acceleration (ABA) measurements. Frequency response functions (FRFs) from hammer tests indicate two track resonances, for which the FRF magnitudes on the plain track are at least 30% lower than those at the abutment. The falling weight measurements indicate that the track on the bridge has a much higher deflection than the track on the embankment. Two features from ABA signals, the dominant spatial frequency and the scale average wavelet power, show variation along the transition zone. These variations indicate differences in track conditions per location. Finally, the ABA features in the range of 1.05 m^{-1} to 2.86 m^{-1} are found to be related to the track resonance in the range of 30 Hz to 60 Hz. The findings in this chapter provide additional support for physically interpreting train-borne measurements for monitoring transition zones.

3.1. INTRODUCTION

Railway transition zones are one of the most critical track segments in railway networks since they connect plain tracks and rigid structures, such as bridges, culverts, and tunnels. The differences in the track substructures at transition zones lead to fast track degradation due to the unevenness in the track support conditions [22,26,29–32,36,131]. Therefore, transition zones require more inspection and maintenance than plain tracks. In the Netherlands, maintenance activities at transition zones are reported to be at least twice as frequent as those conducted on plain tracks [38]. Furthermore, maintenance activities are expensive in terms of budget and human resources. In addition, track availability is reduced during maintenance due to track closure or train speed restrictions. Thus, more efficient maintenance methodologies, such as condition-based maintenance, are needed, for which frequent updates of crucial information on transition zone health conditions are necessary.

According to the literature, several wayside measurement techniques have been developed to evaluate the performance and monitor transition zone dynamic behavior. In [68], the performance of the transition zone measurement was investigated based on the vertical acceleration of sleepers under excitation when trains pass by. Transition zones with track geometry problems have sleeper accelerations that are approximately two times higher than those of a plain track. In [48], a framework that assesses the performance of a transition zone at a culvert was developed. The measurements consist of the track dynamic flexibility based on hammer tests and responses of track components to traffic loads. The results showed that the track on the culvert provided 60% less track dynamic flexibility and 45% lower track displacement than plain tracks. In [33], the root cause of differential displacements at transition zones was investigated. Poor sleeper support conditions were found to be a direct cause of the permanent deformation of the transition zones. In [70], the settlement of multiple substructure layers at transition zones was monitored using multidepth deflectometers (MDDs). The ballast layer exhibited the most accumulated permanent and transient deformations in the case studied. From the literature, wayside measurement techniques have been able to provide different types of information on transition zones. However, track access, the availability of power supplies, human resources, and budgets are significant limitations in deploying wayside measurements.

Onboard sensing solutions have been proposed in the literature for monitoring track geometry degradation in transition zones. For example, the track quality and ride comfort at transition zones have been analyzed using acceleration measured by smartphones [88]. In [122], track vertical displacement due to different loading conditions in transition zones was measured using a mobile system called the rail infrastructure alignment acquisition (RILA) system. In our previous work [111], key performance indicators (KPIs) for monitoring transition zones were proposed from wavelet-based features of axle box acceleration (ABA) signals. Nevertheless, further understanding of train-track dynamics at transition zones is needed to increase the interpretability of ABA responses and KPIs for condition assessment. This chapter contributes to filling this research gap by proposing and applying a measurement framework that combines trackside and train-borne technologies for characterizing the vertical dynamic behavior of a railway transition zone. First, two impact excitation tests, namely hammer tests and falling weight tests, are conducted trackside. Frequency response functions (FRFs) regarding the impact force and track component responses are obtained to characterize the track deflection and track resonances (TRs). Variations in the frequency and magnitude features of the FRFs per location indicate the differences in track conditions. Then, train-borne ABA measurements are conducted, and two wavelet-based features at two spatial frequency ranges (0.04 m^{-1} to 0.33 m^{-1} and 1.05 m^{-1} to 2.86 m^{-1}), dominant spatial frequency and the scale average wavelet power (SAWP), are extracted from the vertical ABA signals. Variations in wavelet-based features are found along the transition zone, indicating changes in track conditions. Further, the ABA features are compared with the features from the impact excitation tests. The ABA features in the spatial frequency range of 1.05 m^{-1} to 2.86 m^{-1} align well with the FRF features at the full track resonance (FT). Their relationship provides experimental evidence on the train-track-embankment vertical dynamic behavior and increases the interpretability of the ABA responses in assessing track conditions. Figure 3.1 describes the flowchart of the proposed measuring framework.

The remaining parts of this chapter are organized as follows. First, a case study transition zone and the measurement campaign for track vertical response identification are described in Section 3.2. In Section 3.3, the analyses of the track vertical responses from hammer tests and falling weight tests are described. Then, an analysis of the ABA responses

at the transition zone is presented in Section 3.4. In Section 3.5, findings from the relationship between the impact excitation tests and ABA signals are discussed. Finally, conclusions and suggestions for further studies are presented in Section 3.6.
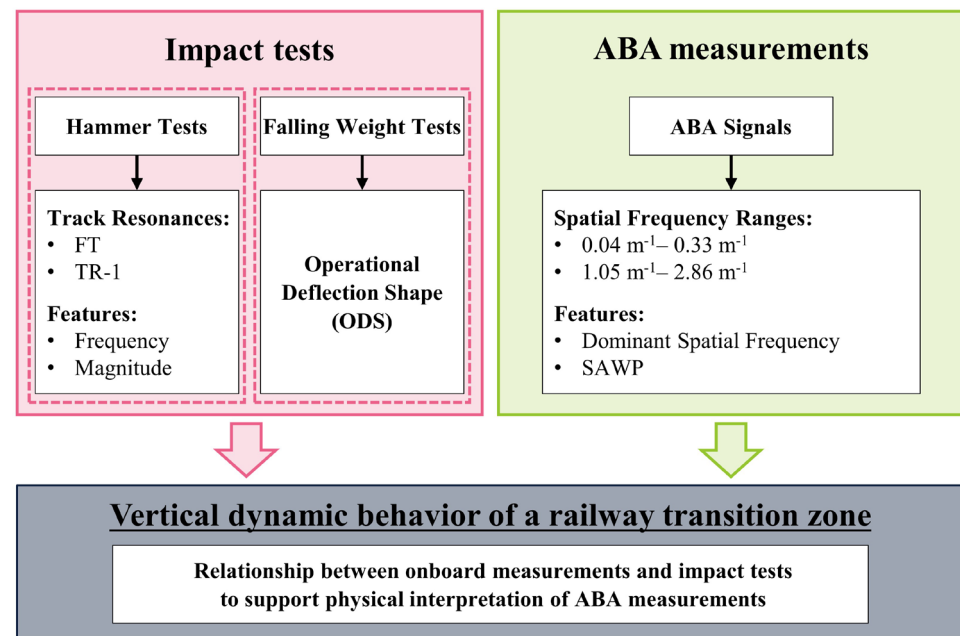
Figure 3.1: Flowchart of the proposed framework of this chapter.

3.2. MEASUREMENTS FOR TRACK VERTICAL DYNAMIC ANALYSIS AT TRANSITION ZONES

3.2.1. DESCRIPTION OF THE CASE STUDY

The railway transition zone analyzed in this chapter is located at a single-span bridge in the Iron Ore Line of Sweden between Boden station and Murjek station. The railway line is a single ballasted track with passenger and freight traffic, including iron ore trains with the heaviest axle load of more than 30 tons. Figure 3.2 shows the bridge and its transition zones.

This bridge is 8.15 m long and has one span, comprising a 4.2 m bridge deck (Zone B), a 1.9 m north approach slab (Zone A), and a 2.05 m south approach slab (Zone C). It is noted that cracks are found on the bridge abutments, which are evidence of the degradation

of the bridge structure. Hence, this bridge was strengthened by installing two steel beams spaced 2.6 m apart to support the bridge deck.
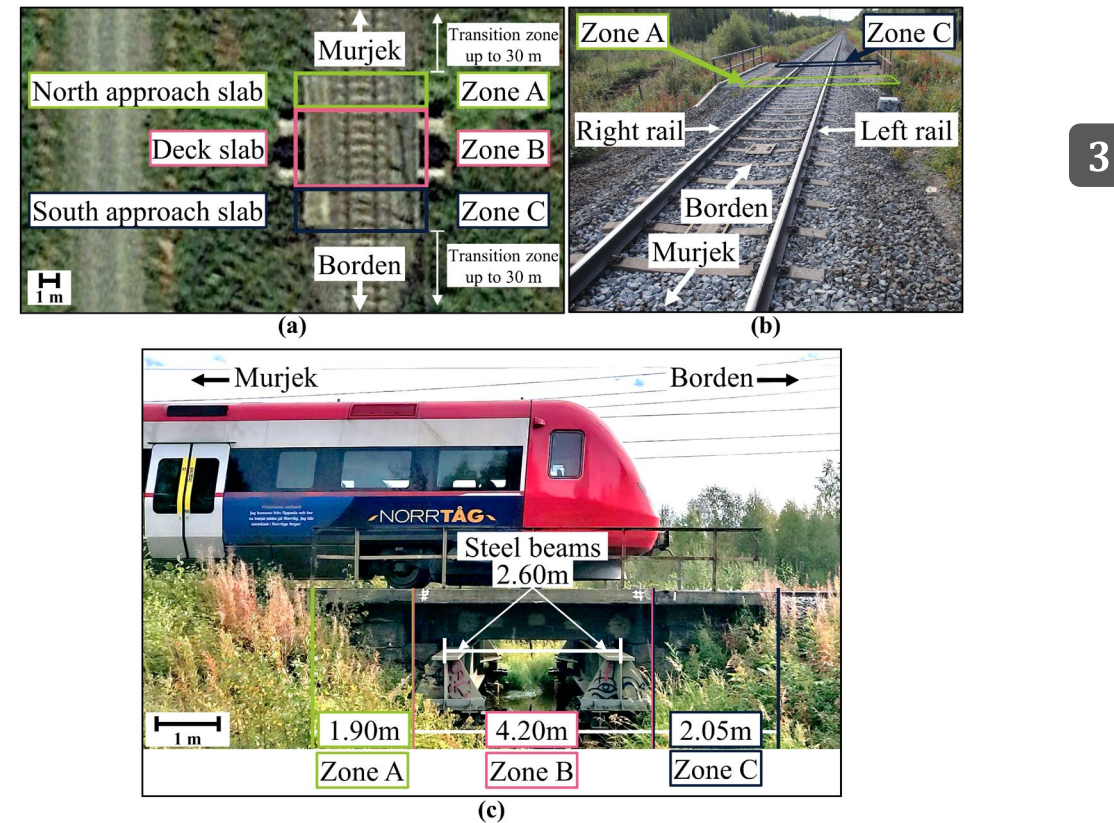
Figure 3.2: A case study track at a short single span bridge: (a) a top view satellite photo (source: Google Maps); (b) a front view photo; (c) a side view photo.

3.2.2. IMPACT EXCITATION TESTS

Impact excitation tests are a common nondestructive measurement technique that is used to identify the dynamic behaviors of a structure by investigating features of their frequency response functions (FRFs). FRFs are transfer functions of the responses of a structure (output) to an impact excitation (input). According to the literature, dynamic characteristic identification [135–137] and estimation of the track component parameters [23,138] can be made by investigating the features of the FRFs.

In this chapter, we consider the impact force, $F(t)$, applied on the rail head as the input and the acceleration, $a(t)$, measured at either a rail or a sleeper as the output. The impact force must be controlled to prevent exceeding the measurement range of load cells and accelerometers. At the same time, excessive force that causes damage to the impactor, the sensors, or the structure at the impact location should also be avoided. In addition, following standard practice, multiple impacts are performed, and inadequate results are disregarded by the repeatability of both input and output signals. This procedure reduces uncertainties in FRF results from measurements.

Three types of FRFs are assessed: accelerance, mobility, and receptance, whose descriptions and relationships are given in Table 3.1 [63]. In the table, $S_{aF}(f)$ is the cross-spectrum of the force and the acceleration, $S_{FF}(f)$ is the autospectrum of the force, and f is the frequency. By analyzing the peaks of the FRFs, it is possible to identify the track resonances (TRs) [63,136]. By observing a specific TR, the deviation in both the frequency and magnitude suggests differences in the dynamic characteristics of the railway track system. Furthermore, different track components have their respective characteristic frequency ranges. For example, track substructure components generally correspond to a frequency range below 150 Hz [139], while track responses in a frequency range from 150–800 Hz are mainly related to sleepers, fastening systems, and rails [140].

Table 3.1: Frequency response functions and their relationship (modified from [63])

Types of FRFs	Accelerance, $H_a(f)$	Mobility, $H_v(f)$	Receptance, $H_d(f)$
Definition	$\dfrac{\text{Acceleration}}{\text{Force}}$	$\dfrac{\text{Velocity}}{\text{Force}}$	$\dfrac{\text{Displacement}}{\text{Force}}$
Formula	$H_a(f) = \dfrac{S_{aF}(f)}{S_{FF}(f)}$	$H_v(f) = \dfrac{H_a(f)}{2\pi f}$	$H_d(f) = \dfrac{H_v(f)}{2\pi f}$

In this chapter, we conducted two types of impact excitations: 1) hammer tests that are suitable to obtain reliable track responses in the frequency range from 30 to 500 Hz and 2) falling weight tests that reliably obtain track responses in the frequency range from 10 to 100 Hz. More details can be found in the following subsections. The reference position (0 m) was defined at the outer edge of the north approach slab, and the position increases in

the direction of Boden station. The average distance of the sleeper interval is 0.65 m. Figure 3.3 shows the locations where hammer tests were conducted on the rail head above sleepers sp_1 to sp_{10} and the locations of accelerometers a_1 to a_8 for track response measurement during the falling weight tests.
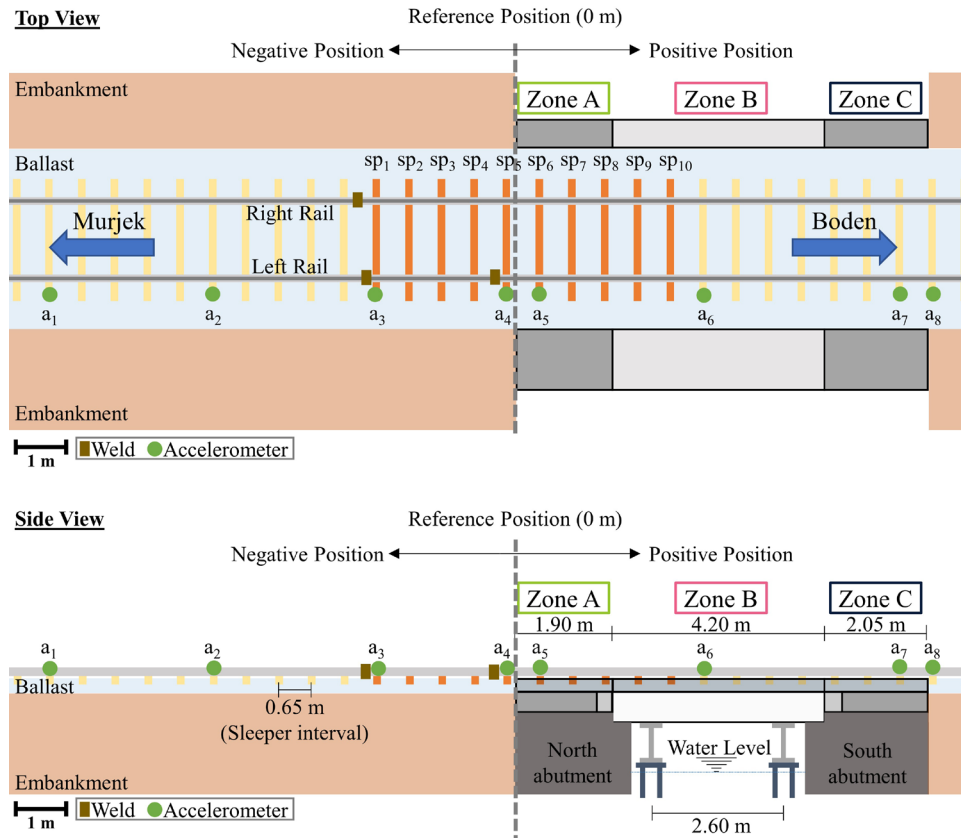
Figure 3.3: Reference position, hammer test locations, and accelerometer positions.

3.2.2.1. HAMMER TESTS

Hammer tests were conducted at 10 locations corresponding to the locations of consecutive sleepers, covering one transition zone (embankment and north abutment). Sleepers sp_1 to sp_5 are located on the track segment on the embankment, while sleepers sp_6 to sp_{10} are located on the segment on the bridge structure. We investigate 'on-support' track responses by applying the impact excitation using a 5.5 kg hammer (PCB 086D50, measurement

range: 0 – 22.2 kN) with a plastic, flat surface, 76 mm in diameter, as a hammer tip on the left rail head directly above the sleeper as an input. The output is a response of the track system in the vertical direction, measured using a unidirectional accelerometer (Brüel & Kjaer 4514-004, measurement range: ± 980 m/s^2), named a_r, attached to the rail head close to the impact location. The force and acceleration signals were recorded using a data acquisition system (MBBM PAK MKII) at a sampling rate of 25.6 kHz. Several impact tests were conducted at the rail head above a particular sleeper. Then, five impacts that provide good coherence were used to calculate an average FRF for minimizing random errors. This setup is shown in Figure 3.4.
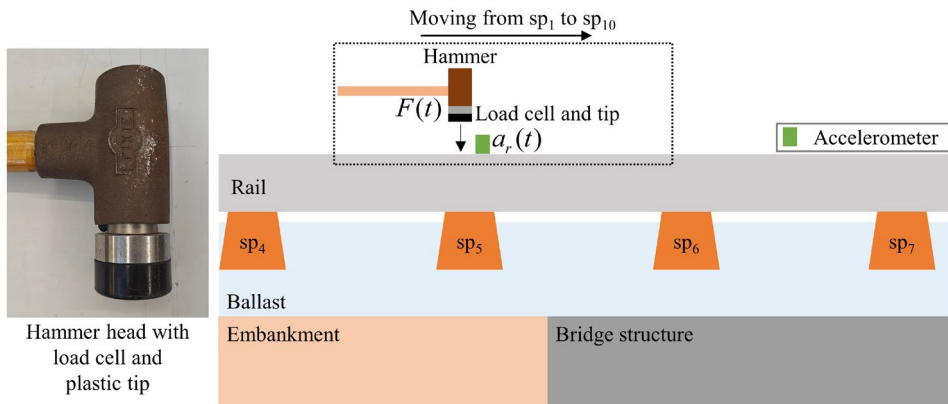
Figure 3.4: A schematic diagram of the hammer test.

3.2.2.2. FALLING WEIGHT TESTS

Falling weight tests efficiently apply large impact energy to the track system to obtain substructure component responses. A special apparatus was designed to release the stacked weight with a plastic, flat surface, 76 mm in diameter, as a tip, similar to a hammer tip, in which the weight and dropping height are adjustable. The impact force is measured using a load cell (Omega LCWD-100K, measurement range: 0 – 444.4 kN). In this chapter, the impact location is at the left rail head at the reference position (0 m) between sp_5 and sp_6. Weights of 60 kg, 80 kg, and 100 kg were dropped from 27 cm, 37 cm, and 47 cm above the rail head. Six unidirectional accelerometers (Bruel & Kjaer 4514-004, measurement range: ± 980 m/s^2), a_1 to a_3 and a_6 to a_8, and two three-directional accelerometers (PCB 356B21, measurement range: ± 4905 m/s^2), a_4 and a_5 (closest sleepers to the impact

location), were attached to the sleepers for measuring transition zone responses. Figure 3.5 shows the measurement setup. The force and acceleration signals were recorded and synchronized using a data acquisition system (MBBM PAK MKII) at a sampling rate of 25.6 kHz. Finally, the average FRF at a particular accelerometer location is calculated using the input and output from 9 configurations of impact.
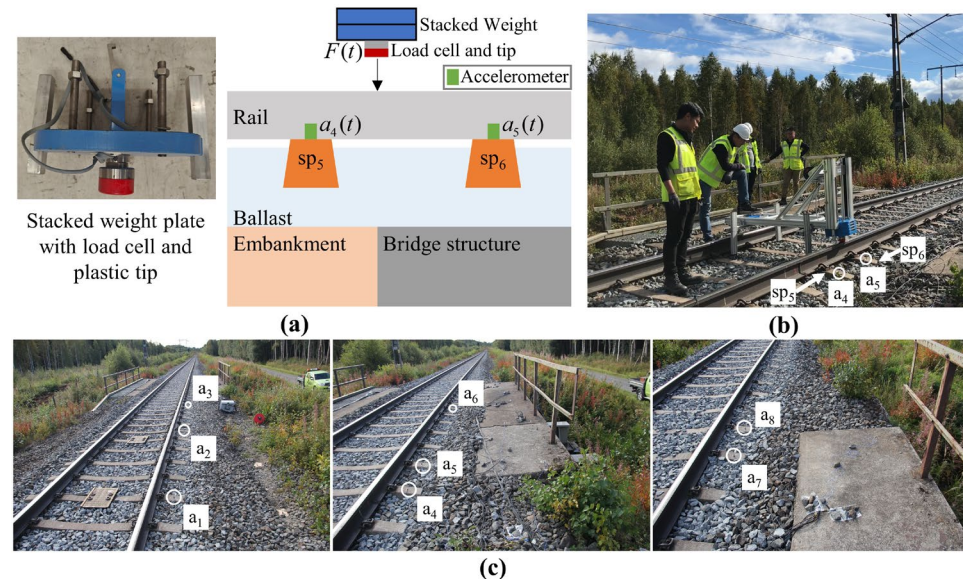
Figure 3.5: Falling weight impact test: (a) a schematic diagram; (b) the falling weight release equipment; (c) accelerometers at eight considered locations.

3.2.3. AXLE BOX ACCELERATION MEASUREMENT SYSTEM

An ABA measurement system was designed to measure vehicle responses on axle boxes as the vehicle interacts with the track. In this chapter, such a system was installed in a passenger wagon. At each axle box, responses were measured using unidirectional accelerometers. In addition, the train position and speed were measured using a high-precision GPS receiver module. All signals were synchronized and recorded using a data acquisition system (NI compact RIO) at a sampling rate of 25.6 kHz. More details of the ABA measurement system can be found in [110,112].

In this chapter, we consider vertical ABA signals. The acceleration at time instant t for wheelset w and rail r is defined as $a_{w,r}(t)$. Eight acceleration signals from four wheelsets w

$\in \{1, 2, 3, 4\}$ and the left (L) and right (R) rails $r \in \{L, R\}$ are considered. The location of wheelset w at time instant t is $x_w(t)$. Then, after synchronizing the signals, the acceleration signals can be evaluated as a function of the track location x, $a_{w,r}(t)$.
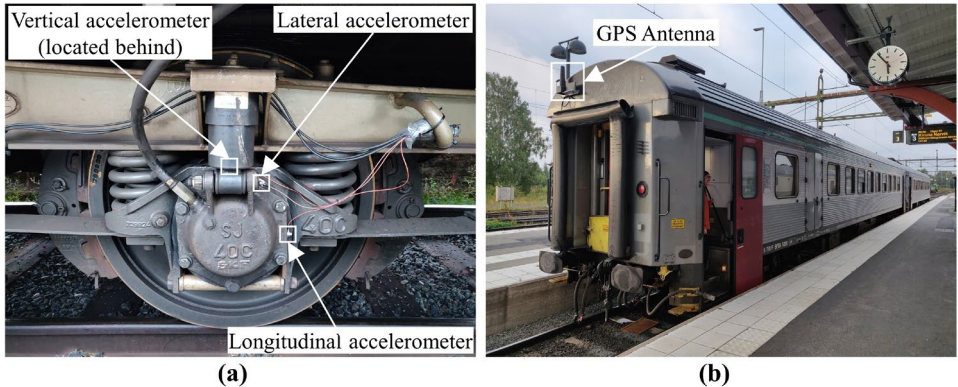
Figure 3.6: ABA measurement system setup on a passenger wagon: (a) position of the accelerometers at one of eight axle boxes; (b) GPS antenna on the roof of the passenger wagon.

The wavelet power spectrum (WPS), which is the product of the continuous wavelet transform (CWT), is considered for analyzing the variation of ABA signals in the time-frequency domain. The WPS can be calculated as follows [127]:

$$WPS_{w,r}(x,s) = \left| \sum_{n'=0}^{N-1} a_{w,r}(n') \psi^* \left(\frac{(n'-n)\delta_t}{s} \right) \right|^2 \qquad \text{Eq. 3.1}$$

where $WPS_{w,r}(x,s)$ is the WPS of the acceleration signal from wheel w and rail r at location x and wavelet scale s with $s > 0$. N is the number of data points in a considered time frame, $n' = 0, \dots , N\text{-}1$, $a_{w,r}(n')$ is the ABA signal at an instant $x_w(n')$, n is the time index variable for the continuous translation, δ_t is the time interval between data points, and Ψ is the wavelet mother function. The function Ψ^* is a family of wavelets derived from the mother wavelet by translations and scaling, and * refers to the complex conjugate. We used the Morlet function as the mother wavelet for this chapter.

Then, two features can be extracted from the WPS, the global wavelet power spectrum (GWPS) and the scale average wavelet power (SAWP), to investigate distributions of the WPS in the frequency (scale) domain and the space domain, respectively.

The GWPS can be calculated as follows [127]:

$$GWPS_{w,r}(s) = \frac{1}{n_2 - n_1} \sum_{n=n_1}^{n_2} WPS_{w,r}(x(n),s), \quad x(n_1) < x(n) < x(n_2)$$ Eq. 3.2

where $GWPS_{w,r}(s)$ is the GWPS of the acceleration signal from wheel w and rail r within the location from $x(n_1)$ to $x(n_2)$ for wavelet scale s with $s > 0$, $WPS_{x,r}(x(n),s)$ is the wavelet power spectrum at position $x(n)$ and scale s, and n_1 and n_2 are selected according to the preferred length of track segment in the analysis. The track segment length can be adjusted based on user preference. The longer considered track segment makes the dominant spatial frequency more pronounced; however, the local characteristics will be hindered. In addition, the number of data points per considered segment depends on measurement speed since the ABA measurement system records signals with a fixed sampling rate. The lower speed provides a higher number of data points.

This chapter investigates the variation of track characteristics on the sleeper interval basis. Therefore, we considered the number of data points corresponding to the measurement speed and the spacing between sleepers at 0.65 m for determining the dominant spatial frequency in Section 3.4.2.

The SAWP can be calculated as follows [127]:

$$SAWP_{w,r}(x) = \frac{\delta_j \delta_t}{C_\delta} \sum_{j=j_1}^{j_2} \frac{WPS_{w,r}(x,s_j)}{s_j}$$ Eq. 3.3

where $SAWP_{w,r}(x)$ is the SAWP of the acceleration signal from wheel w and rail r at location x within wavelet scale s from s_{j1} to s_{j2}, $WPS_{w,r}(x,s_j)$ is the wavelet power spectrum at scale j, δ_j is the scale step, δ_t is the time step, and C_δ is the empirically derived constant of the wavelet function.

3.3. CHARACTERISTICS OF THE TRANSITION ZONE RESPONSES TO IMPACT EXCITATION TESTS

3.3.1. IDENTIFICATION OF THE RELIABLE FREQUENCY RANGE

We identify the reliable frequency range of FRFs based on two criteria [23]: 1) the variance of the FRFs for different impact tests should be small, which means there is a narrow envelope in the reliable frequency range, and 2) the coherence should be close to 1 in the reliable frequency range. The coherence is a statistical value in a function of frequency that examines the relation between the input signal (the impact force, $F(t)$) and the output signal (the acceleration, $a(t)$), ranging from 0 to 1. At a considered frequency, the coherence close to 1 indicates a strong relationship between input and output signals. Hence, the quality of the FRF can be indicated by the coherence. The coherence can be calculated as follows:

$$C_{aF}(f) = \frac{\left|S_{aF}(f)\right|^2}{S_{aa}(f)S_{FF}(f)}$$

Eq. 3.4

where $C_{aF}(f)$ is the coherence, $S_{aF}(f)$ is the cross-spectrum of the force and the acceleration, $S_{aa}(f)$ is the autospectrum of the acceleration, $S_{FF}(f)$ is the autospectrum of the force, and f is the frequency.
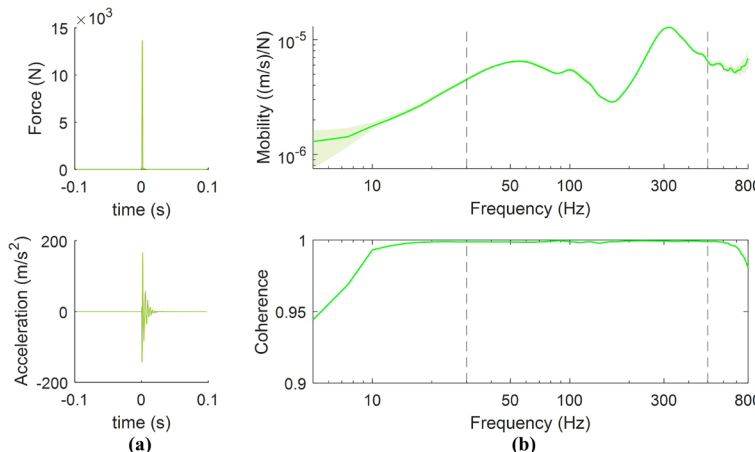

Figure 3.7: Hammer tests, responses measured at the rail head above sp₁: (a) an example of the impact force and the acceleration; (b) mobility and coherence of the track system from 5 hammer impacts.

We chose the FRFs for the hammer tests at the location of sleeper sp_1 as an example. The average FRF, including the envelope (maximum and minimum values) and the coherence, are shown in Figure 3.7. Based on the mentioned criteria, while considering the FRFs at the ten different impact locations, it can be determined that the reliable frequency range is between 30 Hz and 500 Hz.
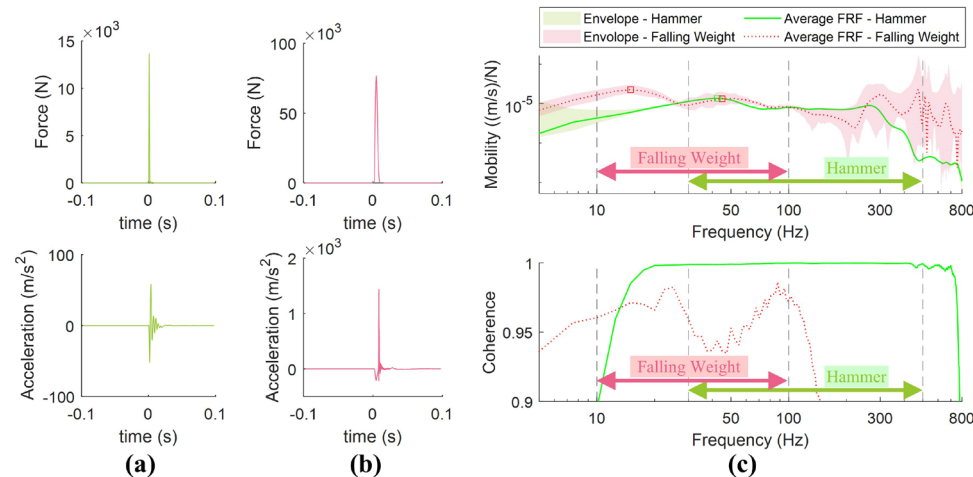
Figure 3.8: Hammer test and falling weight test, responses measured at sleeper sp_5: (a) an example of the impact force and the acceleration due to a hammer impact; (b) an example of the impact force and the acceleration from a 100 kg weight dropped from 47 cm above the rail head; (c) mobility and coherence of the track system from hammer test and falling weight test, □ indicates peaks. The envelope and the coherence of the hammer test are obtained for five impacts from a similar procedure, while the envelope of the falling weight considers a wider range of tests, including tests with different heights and weights.

Then, the reliable frequency range of the falling weight tests is determined. The responses of sleeper sp_5 are selected as an example since its distance from the impact locations of the hammer tests is 0.15 m, which can be considered minor. Based on the abovementioned criteria for determining a reliable frequency range, the results in Figure 3.8(c) show that falling weight tests can be considered reliable from 10 Hz to 100 Hz. Then, in the same figure, we compare the mobility functions between the two types of impact tests. Note that an additional peak of approximately 15 Hz is only observed from the mobility function from falling weight tests. The following peaks of approximately 50 Hz

can be found from both falling weight and hammer tests, even though impact forces and accelerations from both impact tests are largely different, as shown in Figure 3.8(a) and (b). This finding suggests that the FRFs calculated from a wide range of input and output from different impact methods can identify track resonances as long as track resonances are within the reliable frequency range of those impact methods.

3.3.2. VERTICAL DYNAMIC RESPONSES BASED ON HAMMER TESTS

Figure 3.9(a) shows the mobility functions of hammer tests at sp_1 to sp_{10}, in which two noticeable peaks can be observed. The first peak is in the range of approximately 30 Hz to 60 Hz, and the second peak is in the range of approximately 270 Hz to 320 Hz. The first peak is likely full track (FT) resonance, in which the rail and the sleeper vibrate together as a rigid body [63,141]. The identification of the FT resonance can be explained by observing the mobility functions of two outputs at the rail head and underneath the sleeper with respect to the same input. Figure 3.10 compares the mobility functions of the rail and the sleeper at 3 locations: sp1 (a_r and a_3), sp5 (a_r and a_4), and sp6 (a_r and a_5). In each subplot, the peak frequency values in the FT range are insignificantly different between the rail and sleeper FRFs, indicating that both components vibrate together at this resonance. The second peak is named TR-1, which could be related to the responses of other track components above a ballast layer. According to the literature, three track resonances can be determined by hammer tests: 1) FT resonance, 2) rail resonance, in which the rail vibration is relative to the sleeper, and 3) pin-pin resonance, in which the track vibration wavelengths are equal to the sleeper spacing [63,141]. Since the pin-pin resonance mostly occurs between 400 and 1200 Hz, TR-1 should be the rail resonance. Further experiments might be needed to prove this statement.

According to Figure 3.9(a), frequency shifting of FT and TR-1 can be observed from outside the bridge to inside the bridge. Additionally, Figure 3.9(b) and (c) show variations in the magnitudes and damping ratio of TR-1 and FT along the considered track segment. The damping ratio (ζ) can be calculated as follows:

$$\zeta = \frac{\Delta f_{\mathbf{3dB}}}{2 f_{\mathbf{0}}}$$

Eq. 3.5

where ζ is the damping ratio, f_0 is the resonant frequency, and Δf_{3dB} is the bandwidth of the dropped 3dB band from the resonant frequency. Given that the two considered locations provide similar resonant frequencies but differ in dropped 3dB bandwidth. A location with a broader bandwidth represents a faster decay due to a higher damping characteristic, resulting in a higher damping ratio.
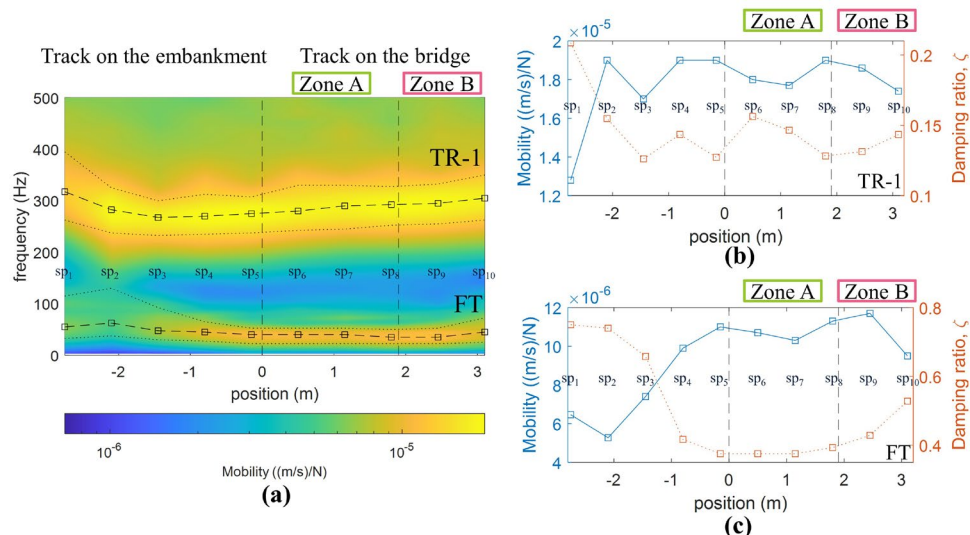
Figure 3.9: Variation in FT and TR-1: (a) a surface plot of the FRFs, including the dropped 3 dB band; (b) mobility magnitude and damping ratio of TR-1; (c) mobility magnitude and damping ratio of FT. □ indicates the positions of sleepers sp_1-sp_{10}, from left to right.

Considering the track segment on the embankment, the locations of sp_1, sp_2, and sp_3 show slightly higher FT frequency values than sp_4 and sp_5, while the corresponding mobility magnitudes are 40 – 55% lower. The damping ratio values at sp_1, sp_2, and sp_3 are 60 - 87% higher than sp_4 and sp_5, representing a faster acceleration decay due to higher damping. The differences in the local conditions in terms of stiffness and damping of the ballast layer should be key factors of the variations in the features of FT resonance [23,63].

Regarding TR-1, the location of sp_1 shows a higher frequency value, but its mobility magnitude and damping ratio are approximately 30% lower and 50% higher than those at sp_2–sp_5, respectively. These findings indicate the different dynamic behavior of the track

components above a ballast layer, and the influence of the nearby weld might have played a role.

While considering the track segment on the bridge from sp_6–sp_{10}, variations in the FT and TR-1 frequency, corresponding magnitudes, and damping ratio are minor compared to those on the embankment. These variations in FRF features from sp_1 to sp_{10} indicate how the vertical dynamic behavior of the track system changes as a function of the position along a transition zone.
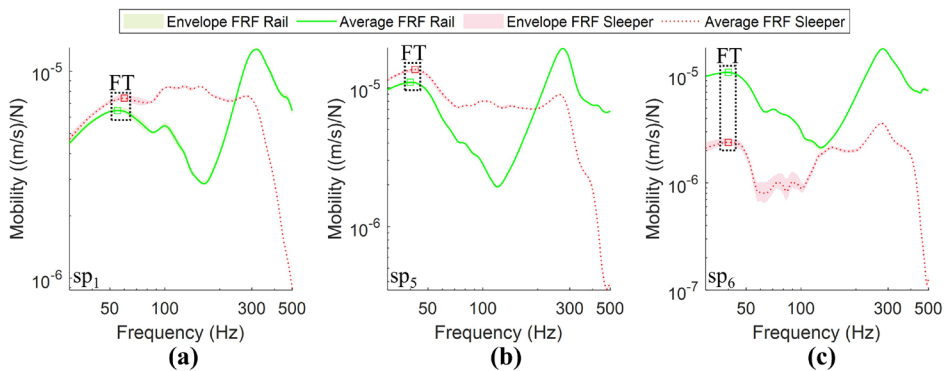
Figure 3.10: FRFs of the track system with respect to responses at the rail head and the sleeper, □ indicates FT: (a), (b), (c) tests at the locations of sp_1, sp_5, and sp_6, respectively.

3.3.3. VERTICAL DYNAMIC RESPONSES BASED ON FALLING WEIGHT TESTS

Different impact test configurations influence the characteristics of FRFs [63,135]. For example, different FRFs are obtained when using different impact excitation forces (different hammers, heights, and weights of the falling weight device), different locations of interest of the output (rail or sleeper), and different distances between the input and output sensors. For example, the peak at 15 Hz (lower than the FT resonance) can be clearly observed from the FRFs of accelerometer a4, which is closest to the impact location, as shown in Figure 3.8. However, FRFs with output sensors farther from the impact location of the falling weight do not obviously identify this peak. This peak could be related to the resonance of the track components underneath the ballast layer since the falling weight device provides higher excitation energy so that lower track components are more excited than when using the hammer.

In this section, we evaluate the deflection characteristics of the transition zone with falling weight at the reference location. We consider the sleeper responses for different frequency ranges through operational deflection shapes (ODSs). The ODS can be used to visualize the actual motion of the structure at the considered frequency, which can resemble mode shapes if the considered frequencies are close to the resonance frequencies of the system. The ODS of the instrumented track can be obtained by considering the imaginary parts of the FRFs, for which the receptance function is considered as follows [142]:

$$ODS(f) = \left[\text{Im}(FRF_{a_1}(f)), \text{Im}(FRF_{a_2}(f)), ..., \text{Im}(FRF_{a_8}(f)) \right] \qquad \text{Eq. 3.6}$$

where $ODS(f)$ is the ODS of the track at the considered frequency f, and FRF_{ai} is the receptance function of accelerometer a_i.

The ODS plots corresponding to the reliable frequency range of the falling weight tests from 10–100 Hz are shown in Figure 3.11. Figure 3.11(a) shows the ODSs corresponding to the frequency range below the FT resonance, which could be related to the responses of the track components below the ballast layer. Except for the responses of a_4 at -0.15 m, which provides the most deflection because it is closest to the impact load, it can be considered that the track segment on the embankment has less deflection than the track segment on the bridge, reflecting the higher capability of the embankment to dissipate and transmit energy compared to that of the track on the bridge. Looking at the ODSs in Figure 3.11(b), which are in the same frequency range as the FT resonance, the a_6 responses at 3.75 m provide the highest downward deflection. As seen in the ODSs in Figure 3.11(c), this location shows the highest upward deflection in the range between 60 and 100 Hz. The location of a_6 is close to the middle span of the bridge deck slab (Zone B); hence, this location can deflect more than Zone A and Zone C, which are closer to the abutments.
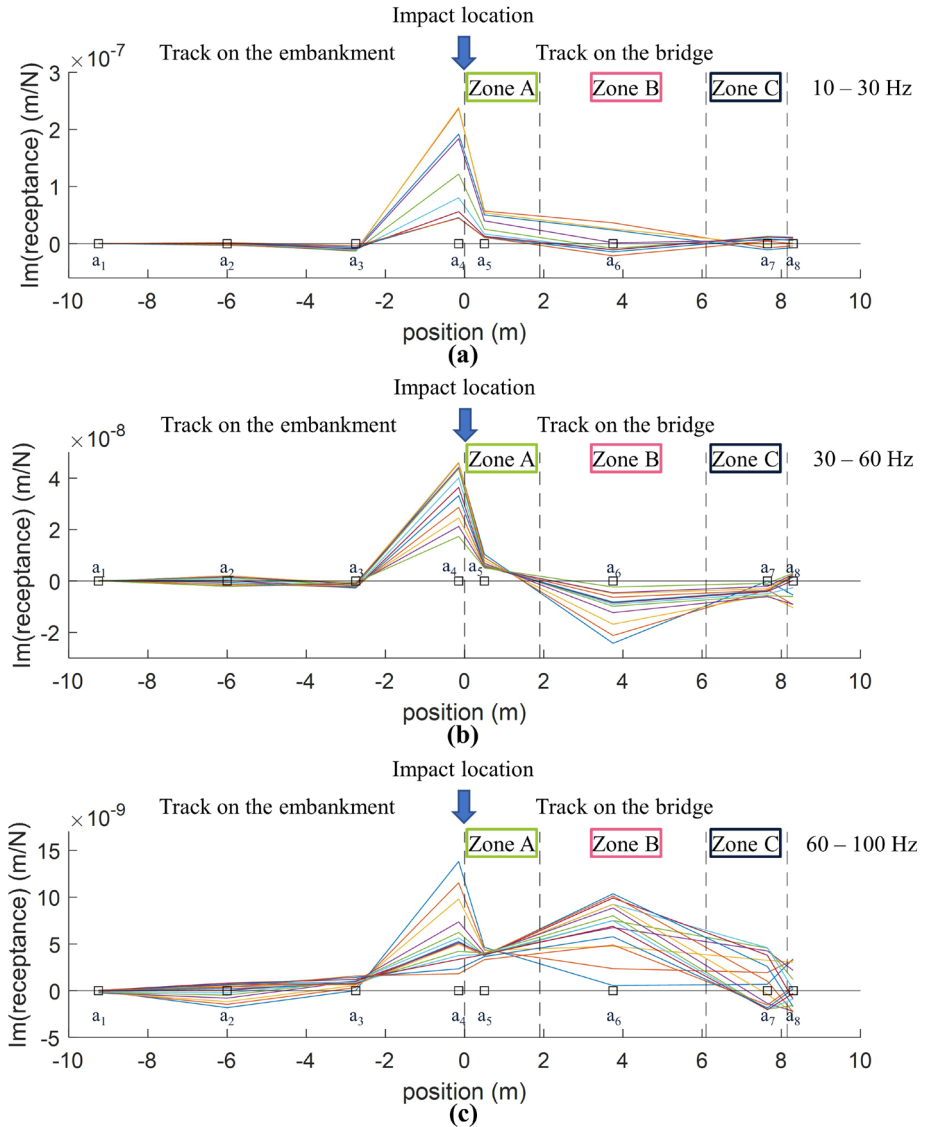
Figure 3.11: Operational deflection shapes of the track at different corresponding frequencies: (a) 10–30 Hz; (b) 30–60 Hz; (c) 60–100 Hz. □ from left to right, indicate the positions of accelerometer a_1 to a_8, respectively, and the arrows represent the impact location at 0 m.

3.4. ABA RESPONSES AT TRANSITION ZONES

3.4.1. ABA SIGNALS IN THE SPACE DOMAIN AND THE SPACE-SPATIAL FREQUENCY DOMAIN

The ABA measurement system was deployed on 25 and 27 August 2022. Each day, the instrumented wagon passed by the case study transition zone two times in different directions. In total, the ABA signals from 4 measurements are available for analysis. Following the findings from a previous study [111], we consider the average vertical ABA signals from four axle boxes on the same side of the wagon and signals within 30 meters from the abutment. Hence, the ABA responses from -30.0 m to 38.15 m are considered in this chapter. Additionally, since the ABA responses are dependent on the speed, we analyze the ABA responses in the space-spatial frequency domain instead of the time-frequency domain. The speed of the train during the different measurements varies, as shown in Table 3.2.

Table 3.2: The average speeds of the instrumented wagon while passing the studied transition zone

Average speed while passing the transition zone	Direction	
	To Murjek	To Boden
Day 1	31.7 m/s	26.8 m/s
Day 2	33.7 m/s	33.0 m/s

Figure 3.12 shows an example of the ABA signals measured toward Murjek station on day 1. Signals in the space domain and the space–spatial frequency domain reflect the properties of the transition zone. Significant changes in ABA signals, particularly in the space-spatial frequency domain, can be observed. The high-energy area is noticed from Zone A to Zone C, with the highest spatial frequency of approximately 0.20 m^{-1} (equivalent to 5 m). This response relates to the interaction of the instrumented wagon with the bridge, and the noticeable spatial frequency is closely related to the length of the bridge deck, which is 4.20 m. Then, energy continuously decreases in the locations further away from the bridge, indicating a change due to the transition zones. Note that at -7.7 m, the spikes in the space domain signal and the high-energy area of approximately 1.53 m^{-1} (equivalent to 0.65 m) and higher are related to welds on both rails. However, the weld on the left rail at -0.3 m does not cause significant differences in the ABA signals. These characteristics of ABA

signals regarding two welds could indicate differences in the weld health conditions, which further investigation could provide more understanding.

The developed KPI^{side} [111] can be used to evaluate the difference in the degradation level between the transition zones of a bridge. The KPI is based on the relative ABA energy difference between the transition zones at the entrance side and the exit side of the bridge with respect to the travel direction of the measurement system. The KPI can be calculated as follows:

$$\text{KPI}^{side} = \frac{\left(\sum_{x=x_3}^{x_4} \overline{SAWP}^{exit}(x) - \sum_{x=x_1}^{x_2} \overline{SAWP}^{entrance}(x) \right)}{\dfrac{\left(\sum_{x=x_3}^{x_4} \overline{SAWP}^{exit}(x) + \sum_{x=x_1}^{x_2} \overline{SAWP}^{entrance}(x) \right)}{2}} \times 100 \qquad \text{Eq. 3.7}$$

where $\sum_{x=x_m}^{x_n} \overline{SAWP}_b^{location}(x)$ is an average SAWP from four wheelsets at a considered location from x_m to x_n, x_1 and x_2 are the boundary positions of the transition zone at the entrance side, and x_3 and x_4 are the boundary positions of the transition zone at the exit side. A positive KPI^{side} indicates that the transition zone at the exit site is more degraded. Based on the four measurements, the north abutment transition zone is more degraded than the south abutment, as shown in Table 3.3. The supporting reason is that the full loaded iron ore trains travel in the direction to Boden. The trains have the heaviest axle load that could accelerate the degradation of the north abutment transition zone.

Table 3.3: KPI^{side} to evaluate the relative degradation level between 2 transition zones.

| Direction	KPI^{side}			Interpretation
	Day 1	Day 2	Average	
To Murjek	44.06	43.30	43.68	The exit side transition zone (north abutment) is more degraded.
To Boden	-6.61	-5.01	-5.81	The entrance side transition zone (north abutment) is more degraded.
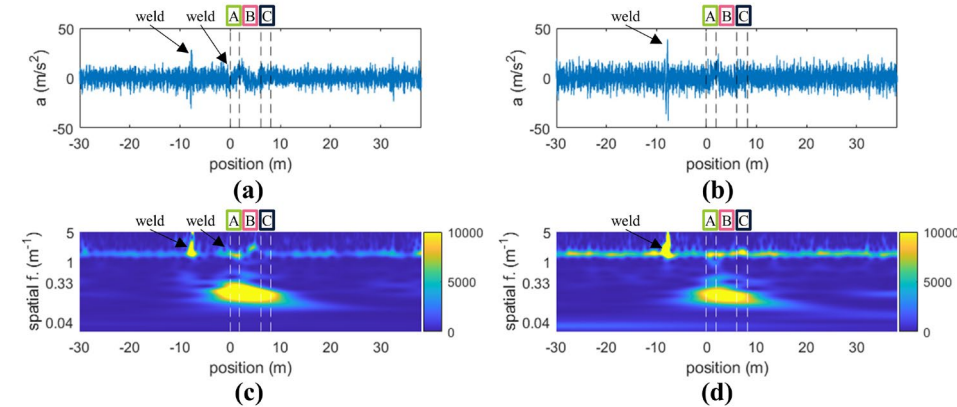
Figure 3.12: Average ABA: (a), (b) signals in the time domain on the left and right rails, respectively; (c), (d) wavelet power spectra in the space-spatial frequency domain on the left and right rails, respectively.

3.4.2. ANALYSIS OF ABA FEATURES AT TRANSITION ZONES

In this chapter, we consider investigating two extracted features from ABA signals: 1) the SAWP, which can be calculated according to Eq. 3.8, and 2) the dominant frequency of a particular piece of track at a particular spatial frequency range, which can be defined as follows:

$$f_a^{\text{dom}}(x) = \arg\max_{f \in [f_1, f_2]} \left(\overline{GWPS}(f) \right), \quad x \in [x_1, x_2]$$

Eq. 3.8

where $f_a^{\text{dom}}(x)$ is the dominant frequency in the range $a = [f_1, f_2]$ within the track location from x_1 to x_2, and $\overline{GWPS}(f)$ is an average GWPS from four wheelsets. In this chapter, we consider a moving window of 0.65 m with 95% overlap to capture the changes in the dominant frequency.

For a particular extracted feature, we considered its variation within two spatial frequency ranges. The first spatial frequency is between 0.04 m^{-1} and 0.33 m^{-1}, corresponding to wavelengths of 3 m to 25 m (D1 wavelength, according to EN 13848-1 [89]). The second range is between 1.05 m^{-1} and 2.86 m^{-1}, corresponding to wavelengths of 0.35 m to 0.95 m. This wavelength corresponds to the sleeper interval of +/- 0.3 m.

According to an investigation of the scalogram of the wavelet power spectrum, those two spatial frequency ranges provide the most noticeable ABA energy.

Figure 3.13 shows the variation in the ABA features measured on day 1 in the direction toward Murjek station, from -10 m to 10 m, covering the north transition zone and the bridge where impact tests are conducted. Besides the influence of the welds at -7.7 m which obviously provide changes in ABA signals, in Figure 3.13(a) and (b), the dominant spatial frequency variation in the range of 0.04 m^{-1} to 0.33 m^{-1} (the green lines) of both rails shows a similar trend at the track segment on the bridge, where the dominant frequency gradually decreases from Zone A to Zone C, from 0.20 m^{-1} to 0.17 m^{-1}. In comparison, the track segment on the embankment from -7 m to -2.5 m shows unevenness between the left and the right rails. Considering the dominant frequency in the range of 1.05 m^{-1} to 2.86 m^{-1} (the red lines), the dominant frequency is at 1.53 m^{-1} for most of the track locations on the right rail, and a slight shift occurs at the location of Zone C. In contrast, the dominant frequency on the left rail shows a higher level of fluctuation with a noticeable change from -2 m to 7 m. The highest shift is at 4.4 m in the middle of Zone B. Then, the dominant frequency gradually decreases to 1.53 m^{-1} at approximately 7 m in the middle of Zone C.

Variations in the SAWP from the left and right rails are shown in Figure 3.13(c) and (d). The SAWP in the range of 0.04 m^{-1} to 0.33 m^{-1} (the blue lines) gradually increases when approaching the bridge, with the highest value at about 2.0 m where is the connection between Zone A and Zone B (from the north abutment to the deck slab). Considering the SAWP in the range of 1.05 m^{-1} to 2.86 m^{-1} (the orange lines), the peaks due to the weld at -7.7 m, which the right rail shows the higher magnitude, can be observed from both rails. While the weld at -0.3 m on the left rail does not provide a significant peak. Besides, fluctuations in the SAWP of both rails along the transition zones and the bridge can be observed.

According to these observations, a conclusion can be drawn that the considered ABA features are relevant to the variation in vertical track dynamic behavior. Noticeable changes are found in transition zones, where the track support conditions change drastically. Furthermore, noticeable dissimilarities in ABA features between the left and right rails are

found at some parts of the track. This indicates that there are differences in the local conditions between the rails.
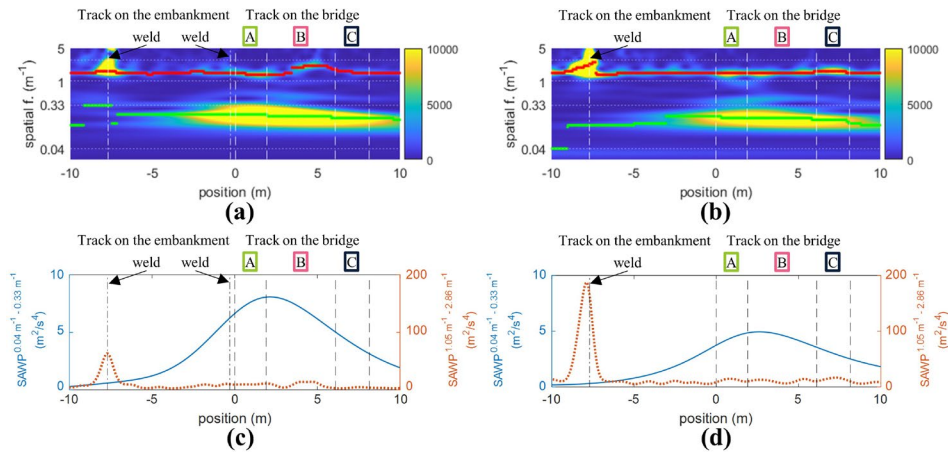

Figure 3.13: Variation in the ABA features at the considered track segment: (a), (b) dominant spatial frequencies on the left and right rails, • corresponds to the range of 0.04 m^{-1} to 0.33 m^{-1}, • corresponds to the range of 1.05 m^{-1} to 2.86 m^{-1}; (c), (d) SAWP of 2 considered bands on the left and right rails.

3.4.3. REPEATABILITY OF THE ABA MEASUREMENTS

This section evaluates the repeatability of the considered ABA features considering two measurement speeds and two measurement directions. Please note that the influence of the welds is not included in the analysis. Regarding the influence of the measurement speed, the ABA signals from the left rail and measurements in the direction toward Murjek Station on Day 1, with a running speed of 31.7 m/s, and on Day 2, with a running speed of 33.7 m/s, are selected for evaluation. Figure 3.14(a) shows the considered ABA features from the two measurements. Both measurements show a similar pattern of dominant frequency in the ranges of 0.04 m^{-1} to 0.33 m^{-1} and 1.05 m^{-1} to 2.86 m^{-1}. The SAWPs from the two measurements are similar. However, the measurement with a higher measurement speed yields a higher SAWP magnitude than that with a slower measurement speed.

Next, the evaluation of the influence of the measurement directions is considered. The ABA signals on the left rail from the measurements in the direction toward Murjek Station on Day 2 with a measurement speed of 33.7 m/s and toward Boden Station on Day 2 with

a measurement speed of 33.0 m/s are selected. Figure 3.14(b) shows the variation in the considered ABA features between the two measurements. Although the different wheel moving directions at the transition zones provide different wheel force distribution characteristics [26], the variations in the ABA features between the two measurements are similar. There are minor differences in ABA features in the range of 1.05 m^{-1} to 2.86 m^{-1} (see the second and the fourth rows of Figure 3.14(b)). The dominant frequencies show a slight difference in Zone B at approximately 4 m to 5 m from the middle of the bridge deck (the second row of Figure 3.14(b)). Moreover, the SAWPs show different numbers of peaks and peak locations between -3 m and 5 m (the fourth row of Figure 3.14(b)).
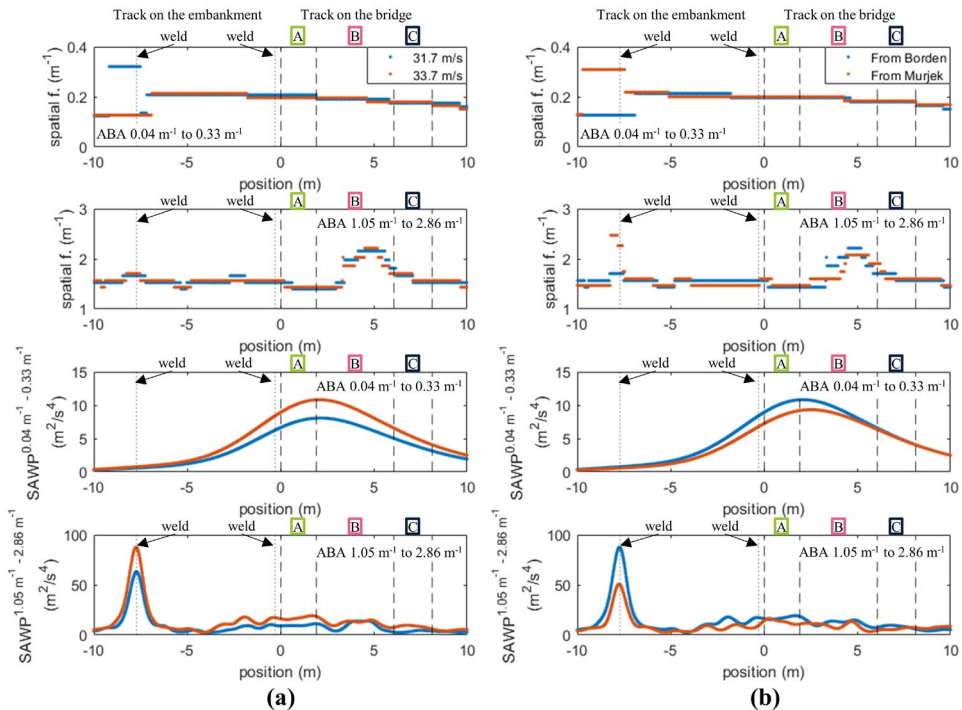
Figure 3.14: Variation in the ABA features on the left rail: (a) different speeds; (b) different directions. The first and second rows are the dominant spatial frequencies in the ranges of 0.04 m^{-1} to 0.33 m^{-1} and 1.05 m^{-1} to 2.86 m^{-1}, respectively. The third and fourth rows are the SAWP corresponding to the dominant spatial frequency in the range of 0.04 m^{-1} to 0.33 m^{-1} and 1.05 m^{-1} to 2.86 m^{-1}, respectively.

These findings suggest that ABA measurements with different speeds and directions provide considerable consistency ABA features. Making transition zone conditions monitoring using in-service trains more reliable.

3.5. RELATIONSHIP BETWEEN THE IMPACT TESTS AND ABA MEASUREMENT RESULTS

The results from the impact tests and ABA measurements allow us to estimate the variations in the vertical dynamic behavior at different locations in the transition zone. The proposed measurement framework can be used to assess the health conditions of railway tracks and estimate their properties, such as track stiffness and damping from FRF-derived features [23,63,135]. In this section, we analyze the possible relationships between the impact tests and ABA measurements to be able to interpret the condition monitoring results from ABA measurements.

The ABA responses in the ranges of 1.05 m^{-1} to 2.86 m^{-1} are most likely related to ballast layer conditions. An investigation shows that the changing trend of the dominant frequency of the ABA signals is aligned with the FT resonance obtained by the hammer tests, as shown in Figure 3.15(a) and (c). Both features show a decreasing trend from approximately -2 m to the end of Zone A.

The SAWP from ABA signals follows a behavior similar to the FT resonance magnitude estimated from the hammer tests, as indicated by the arrows in Figure 3.15(b) and (d). An increasing trend of both features can be observed from approximately -2 m to 0 m. Then, both values fluctuate with two peaks from the beginning of Zone A to the beginning of Zone B.

These findings suggest that changes exist in the transition zone vertical dynamic behavior due to sleeper support conditions, in which conditions of a ballast layer are dominant. This finding agrees with the current knowledge that sleepers and rails vibrate together like a rigid body in terms of FT resonance, in which the properties of the ballast layer play a major role, as mentioned in Section 3.3.2.

In addition, the variation in the ABA features provides a noticeable change at 3.0 m to 7.0 m, which covers Zone B and Zone C, as shown in the dotted boxes in Figure 3.15(a) and (b). This region corresponds to the high deflection at the position of accelerometer a_6, according to the ODSs obtained with falling weight tests, as shown in Figure 3.11. These high deflection factors could be a result of the ballast layer properties, and the location could be a contributing factor. This location is close to the middle span of the bridge deck, which tends to deflect and vibrate more than other parts.
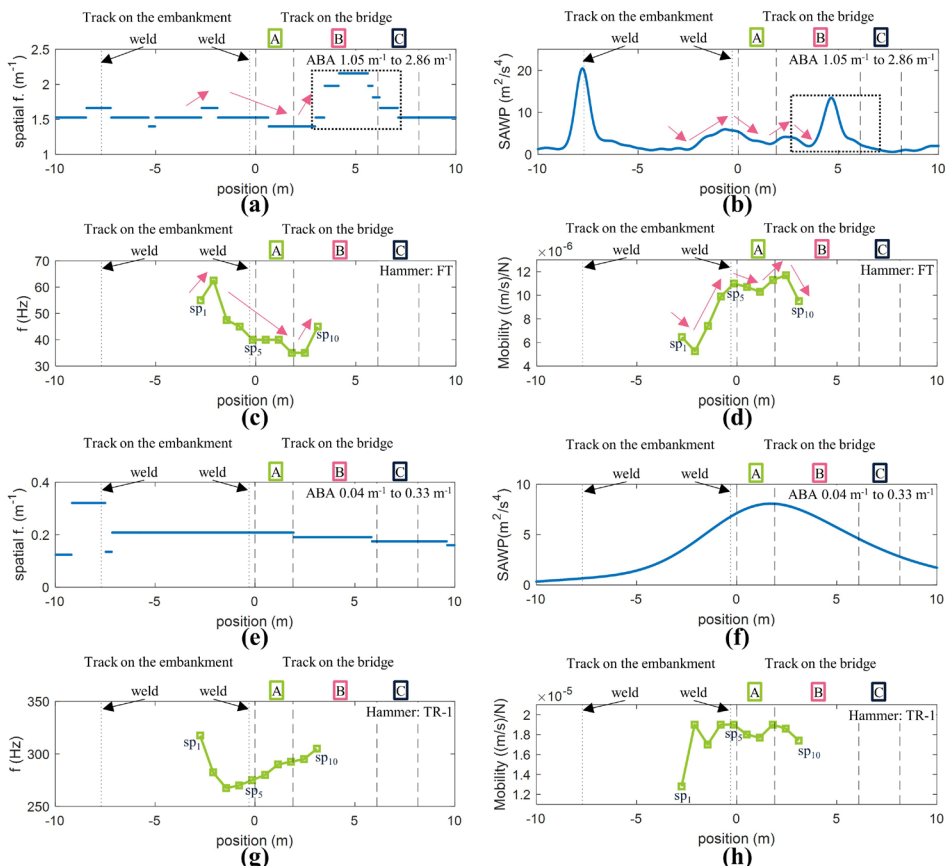
Figure 3.15: The features from the hammer tests and ABA measurements: (a), (b) the dominant frequency and SAWP in the range of 1.05 m^{-1} to 2.86 m^{-1}; (c), (d) the FT resonance and its mobility magnitude; (e), (f) the dominant frequency and SAWP in the range of 0.04 m^{-1} to 0.33 m^{-1}; (g), (h) the TR-1 resonance and its mobility magnitude; □ indicates the positions of sleepers sp_1–sp_{10}, from left to right, respectively.

Looking at Figure 3.15(e) and (f) for the range of 0.04 m^{-1} to 0.33 m^{-1}, no clear relationship could be identified between the ABA responses and features from the hammer tests. ABA features in this range are not well aligned with the features of FT (Figure 3.15(c) and (d)) and TR-1 (Figure 3.15(g) and (h)) obtained by the hammer tests. The reason is that ABA responses in this range are related to the substructure condition in this spatial frequency range, while FT and TR-1 are related to the condition of the ballast layer and the components above it, respectively.

Even though the available measurement datasets from the impact tests cannot fully understand ABA features in the range of 0.04 m^{-1} to 0.33 m^{-1}, it has been reported that ABA responses in the spatial frequency range are related to the substructure conditions. Therefore, ABA measurements still provide valuable insights into the conditions of the substructure and the ballast layer, allowing estimation of the health condition of the transition zone. Unlike a more degraded transition zone, a transition zone with healthy conditions should exhibit fewer fluctuations in its vertical dynamic characteristics. Notably, the ABA features near 0 m (the north abutment transition zone) show more pronounced changes compared to those near 8.15 m (the south abutment transition zone); please see Figure 3.15(a), (b), (e), and (f). This observation suggests a higher degree of degradation in both the ballast and substructure layers in the north abutment transition zone, which aligns with the findings presented in Table 3.3.

3.6. CONCLUSIONS

This chapter investigates the vertical dynamic behavior of a railway bridge transition zone through an experimental assessment with two measurement techniques: impact tests and onboard measurements. Impact tests provide information about some important track characteristics, including track resonant frequencies and their corresponding magnitudes, which can be observed from the FRFs from the hammer and falling weight tests. Additionally, the track deflection responses can be analyzed by means of the ODSs derived from falling weight tests. Moreover, ABA signal characteristics indicate that the variations in the train-track interactions at transition zones are strongly related to the track health condition. Since the two measurement techniques are based on different principles, analyzing the relationship between the features from the two techniques could provide more

understanding of the ABA features. Furthermore, ABA measurements can be beneficial for health condition monitoring of transition zones at the network scale. According to the findings from the case study, the following conclusions can be drawn:

1. Variations in the FT and TR-1 resonances from hammer tests are observed at different transition zone locations. This indicates that different track vertical dynamic behaviors exist with respect to the ballast layer and the components above it. In comparison, an additional track resonance factor that is lower than FT can be obtained from the falling weight tests.

2. ODSs derived from the falling weight tests show different deflection characteristics along the transition zone. This indicates differences in vertical dynamic responses between segments of the track on the embankment and the track on the bridge.

3. The ABA features from different operational conditions, which are the speeds and moving directions, show considerable consistency in the dominant frequencies and SAWPs along the transition zone, particularly in the two considered spatial frequency ranges, 0.04 m^{-1} to 0.33 m^{-1} and 1.05 m^{-1} to 2.86 m^{-1}. This knowledge can be utilized to minimize the influence of uncertainty in transition zone condition monitoring with in-service trains.

4. The ABA features in the spatial frequency range of 1.05 m^{-1} to 2.86 m^{-1} are related to ballast layer conditions since a similar pattern can be observed between the ABA features and FT resonance features. The dominant ABA frequency is related to the FT resonant frequency, while the SAWP of the ABA is related to the magnitude of the FT resonance.

5. The location that is highly deflected due to excitation can be identified by both ABA measurement and falling weight tests, and the results from both measurement techniques are well aligned.

4

ENHANCED VERTICAL TRACK QUALITY INDEX WITH ABA SIGNALS

The conventional vertical track quality index (TQI) based on the standard deviation of longitudinal levels yields standardized railway track condition assessment. Nevertheless, its capability to identify problems is limited, particularly in the ballast and substructure layers when abrupt changes affect train-track interaction. Previous research shows that dynamic responses from moving trains via axle box acceleration (ABA) measurements can quantify abrupt changes in the vertical dynamic responses. Thus, this chapter proposes a framework to design an enhanced vertical TQI, called EnVTQI, by integrating track longitudinal levels and dynamic responses from ABA measurements. First, measured ABA signals are processed to mitigate the influence of variation in measurement speed. Then, substructure and ballast-related features are extracted, including scale average wavelet power (SAWP) in the ranges 0.04 m^{-1} to 0.33 m^{-1} (substructure) and 1.25 m^{-1} to 2.50 m^{-1} (ballast). This enables identifying track conditions at different track layers. Finally, EnVTQI is determined by weight averaging between the conventional vertical TQI and the ABA features from moving trains. The performance of EnVTQI is evaluated based on 48 segments of a 200-meter track on a Dutch railway line. The results indicate that EnVTQI helps to distinguish track segments that cause poor train-track interaction, which the conventional TQI does not indicate. EnVTQI can supplement the conventional TQI, improving the effectiveness of track maintenance decision-making.

4.1. INTRODUCTION

The ballasted tracks are utilized globally due to their numerous advantages, such as low construction costs, less complexity in design and construction processes, and simplicity of maintenance [7]. The ballast layer and several underneath engineering materials layers, known as the substructure, play an essential role in supporting the track superstructure, i.e., sleepers and rails. The main functions of the substructure are transferring traffic loads, facilitating drainage, and maintaining track alignments [18]. The degradation of ballast and substructure layers leads to poor track quality, resulting in broken ballast, excessive mud, and track settlement. In addition, vegetation and excessive undrained water on the track surface suggest a high moisture content in the substructure layer, resulting in a lower bearing capacity of materials [10]. These degraded track segments can cause abrupt changes in train-track interaction, which increases risks and safety concerns and reduces the service quality of train operations.

Track geometry measurements using track recording vehicles [19] are the standard practice in the railway industry for track inspection at the network level. To assess the overall quality of railway tracks, different track quality indices (TQI) have been developed based on statistical analyses of track geometry parameters and combined by using mathematical methods. TQIs are then used by railway authorities or infrastructure managers to standardize track quality and define maintenance requirements. Examples of conventional TQIs are the combined standard deviation (CoSD) of the European standard [90], the Q index of the Swedish national railway [92], the Chinese TQI [93], the US track roughness index [94], and the FRA track geometry index [95]. In [96], the accuracy, sensitivity, data required, and specificity of TQIs, including CoSD as the baseline, are evaluated based on synthetic track geometry data. As expected, the findings show that different TQIs perform differently in indicating track segments that need maintenance. When selecting a TQI, their tradeoffs are to be considered. For example, the US track roughness index and FRA Track Geometry Index (TGI) show high sensitivity to changes in geometry parameters, which might be easily biased by noise or error in measurement. In [97], the characteristics of 14 TQIs have been studied based on measurement data. The

results show that the standard deviation-based TQIs perform well in assessing overall track condition but might be biased due to track gauge widening in the curved track segments.

Some studies have focused on data-driven and machine-learning methods to extract information from track geometry parameters as an alternative approach. Using data analytics, those applications can provide track geometry forecasts [98] and track geometry degradation predictions [99]. In [11], principal components analysis (PCA) is used for dimension reduction of track geometry parameters. The results show that more than 90% of the variance can be explained by the first three principal components (PCs). In addition, the PCs can be considered directly as TQIs since they perform better in defective segment identification than conventional TQIs. In [100], the dimension reduction of track geometry parameters using T-stochastic neighbor embedding (T-SNE), a nonlinear method, is compared with PCA, a linear method. While the two methods can represent track quality, T-SNE tends to overfit the training and test datasets, resulting in false defect prediction. In [101], a stochastic TQI is developed to deal with uncertainty in measurements of track geometry parameters, in which the Bayesian analysis is its core. In [102], the relationship between track geometry parameters and the lateral to vertical wheel load ratio has been studied using neural network models. The relationships obtained are then used as part of the track geometry inspection technology. Nevertheless, further understanding of the physical meaning of the results from data-driven and machine learning approaches is required by including the physical interpretability of the results.

Track quality assessment based on track geometry parameters has some limitations. For instance, track geometry measurements cannot always capture abrupt changes in train-track interaction [102,103]. Moreover, measurement frequency at a particular location might be limited due to the availability of track recording vehicles. Thus, measurement techniques implemented using in-service trains are becoming the focus of the railway industry. This approach can minimize the abovementioned concerns due to the advantages of the instrumented in-service trains operating daily. Thus, vehicle responses can be obtained frequently as inputs for track quality assessment. However, the challenge is extracting useful information from measured data and standardizing such a type of measurement. According to the literature, several studies have been conducted to find

solutions to use vehicle responses for assessing track condition. In [82], linear regression models are developed to estimate the longitudinal level from bogie vertical acceleration signals. Then, the root-mean-square values of the estimated longitudinal level can be used as a track condition indicator. In [83], a method to estimate track vertical and lateral irregularities using bogies and axle box acceleration signals is developed. Several layers of filtering methods, including Kalman filter, bandpass filters, and amplitude and phase compensation filters, are applied to analyze acceleration signals to obtain estimated track irregularities. In [84], a Kalman filter-based model is developed to estimate lateral track irregularity using input from a gyroscope and accelerometers at a wheelset and a bogie frame. Besides estimating track irregularities, some studies develop a track condition indicator derived from measured vehicle responses. In [85], the continuous wavelet transform is conducted on the simulated vertical vehicle body acceleration from the 2-DOF model while the train passes various track conditions. Then, the summation of wavelet coefficients of the acceleration signal can be considered an indicator to identify damage locations. In [86], vertical vehicle body acceleration is the input. Then, the developed algorithm is applied to simplify the input into a bump pattern, whose characteristics, such as magnitude, can be considered an indicator. In [87], a support vector machine classifier with a linear kernel is used to determine the most robust features from car body acceleration in detecting track changes. Those outcomes from vehicle responses can be used separately or supplementary to conventional TQIs for more effective track maintenance planning rather than relying solely on track geometry information from dedicated track recording vehicles.

Track condition assessment based solely on track geometry parameters provides some constraints, while previous research works have demonstrated the potential of utilizing vehicle responses for track condition assessment. Hence, those aspects motivated us to enhance the performance in track condition assessment by integrating track geometry parameters and vehicle responses. This chapter proposes a framework to design an enhanced vertical track quality index, called EnVTQI, by combining track geometry and vehicle responses in the vertical direction. Track quality regarding the vertical direction is considered since deviation in the longitudinal level, which is relevant to track vertical irregularities, has been reported to be highly relevant to overall track quality [143]. We

focus on the axle box acceleration (ABA) measurement regarding vehicle responses. Measuring ABA is cost-efficient and not complex when implemented on most types of railway vehicles, including passenger trains that operate daily. Several studies have been conducted on ABA measurements for rail defects and irregularities detection [106–111], but a limited number of studies are related to track quality assessment. In [144], a method to measure track vertical stiffness, a parameter representing a relationship between applied load and overall track deformation, through ABA signals is developed. In [24], a combined approach between physic and data-driven models is developed to evaluate stiffness at different layers, i.e., railpad and ballast, at the same time.

In this chapter, the main contributions are the following.

1. A framework for designing an enhanced vertical track quality index (EnVTQI) by fusing longitudinal level with features from the vertical ABA signals.

2. A method for reducing the influence of measurement speed variation to allow the use of vertical ABA signals that are measured under the operational condition of commercial trains.

3. Validation of the framework on the estimation of ballast and substructure layer conditions.

The remaining sections of this chapter are organized as follows. Section 4.2 describes measurements at railway tracks, which are sources of input for designing EnVTQI. Section 4.3 explains a proposed framework for designing EnVTQI of a particular track segment. Section 4.4 presents results and discussions on the performance evaluation of EnVTQI. Finally, conclusions and suggestions for further work are presented in Section 4.5.

4.2. INPUTS REQUIRED FOR ENVTQI

4.2.1. TRACK INFORMATION

In this chapter, we analyze track segments located on a Dutch railway line, which consists of 2 tracks that are dedicated to a fixed travel direction. Track-I is for operational traffic heading to the North, and Track-II is for the opposite direction. This chapter

considers mostly straight segments. Then, segments are defined with criteria that each segment is 200 meters long, following EN 13848-6 [90], and consists of no civil structures, such as bridges or level crossings, which lead to varying ballast and substructure condition. In addition, some track segments are also excluded due to the composition of track components, such as insulated rail joints, switches, and crossings, resulting in isolated discontinuities of train-track interaction. In addition, the Dutch railway infrastructure has specific criteria for condition assessment of those mentioned civil structures and track components [145]. These criteria align with the finding from [143] that track segments with different characteristics, such as curvature, embankment thickness, and inclusion with civil structures or joints, show local deterioration rates. Thus, we excluded civil structures and track components from the further analysis, allowing a comparison between track segments with similar structural characteristics. According to the mentioned criteria, 48 of the 200-meter-long conventional track segments from both tracks, namely I-1 to I-24 for Track-I and II-1 to II-24 for Track-II, will be evaluated for the case study.
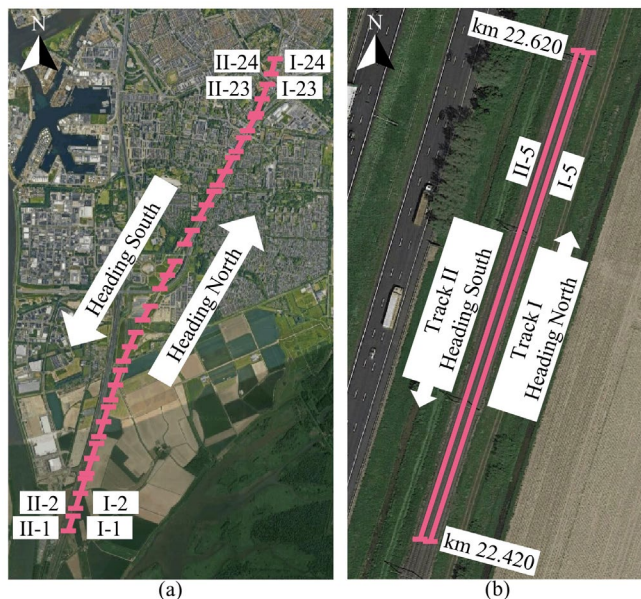

Figure 4.1: Case study track segments: (a) location of 48 segments; (b) zoom-in detail of track segments I-5 and II-5 (source of satellite photos: Google Maps).

4.2.2. TRACK LONGITUDINAL LEVEL MEASUREMENT

ProRail, the infrastructure manager for the Dutch railway network, signs performance-based contracts for track maintenance activities with the outsource contractors. As a part of the contracts, contractors must conduct track geometry measurements with track recording vehicles at least once a year. Then, the information from measurements is centralized at the ProRail railway infrastructure monitoring database, called the Branche Breed Monitoring Systeem (BBMS, in Dutch). All datasets in the BBMS system, including track geometry datasets, are reported as corresponding to the reference track kilometer position.

Among measured track geometry parameters, this chapter considers using only longitudinal levels directly obtained from BBMS. Two obtained longitudinal levels correspond to rail $r \in \{L, R\}$, in which L is the left rail, and R is the right rail. Those signals are already processed with a bandpass filter within a wavelength range between 3 m to 25 m, and the signals have been reported in the space domain with a resolution of 0.25 m, according to EN 13848-1 [89]. Hence, the longitudinal level LL of rail r at the track location x can be defined as $LL_r(x)$. For a 200 m track segment, LL_r consists of 801 data points per rail. In this chapter, one dataset of longitudinal levels measured in 2019 is obtained from BBMS for further analysis on designing EnVTQI.
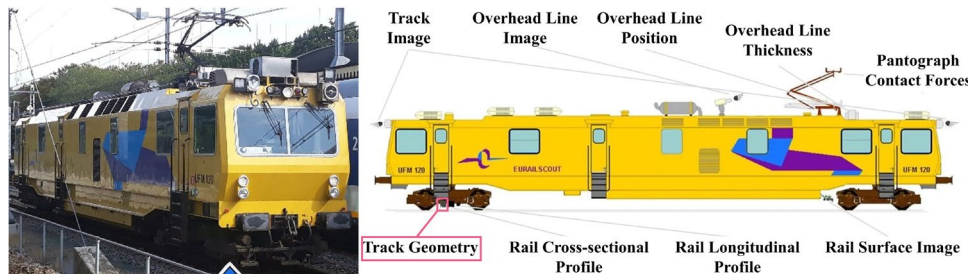

Figure 4.2: Track recording vehicle, in which the geometry measurement module is shown in the box (source of photos: ProRail).

4.2.3. AXLE BOX ACCELERATION (ABA) MEASUREMENT

4.2.3.1. ABA MEASUREMENT SYSTEM

The ABA measurement system developed by the Section of Railway Engineering, TU Delft [123], consists of three major components. The first component is a set of acceleration sensors, a one-directional accelerometer is attached to a particular axle box of the wagon. This study considers only signals from accelerometers in the vertical direction. The second component is speed and positioning sensors, a tachometer and a global positioning system (GPS) unit with real-time kinematic positioning function to determine the measurement speed and corresponding track position of the wagon. The third component is a data acquisition system (DAQ) unit with in-house developed control software for recording and synchronizing multiple signals from all available sensors. Since the ABA measurement system is designed for a wide range of applications in railway infrastructure condition monitoring (including shortwave defect irregularities detection), a sampling rate of 25.6 kHz is used in the current configuration. ABA systems are currently being implemented in various types of railway vehicles in different countries, including daily passenger trains. In this study, the data collected comes from an instrumented wagon from TU Delft dedicated to railway research purposes. In this setup, loading can be considered almost constant in the different measurements, while an important source of variability will come from speed variations, which are analyzed in this chapter.

Based on the configuration of the measurement system, eight acceleration signals are considered from four wheelsets $w \in \{w1, w2, w3, w4\}$, each wheelset with two wheels that correspond to rails $r \in \{L, R\}$, the left (L) and right (R) rails. The acceleration a at time instant t for wheelset w and rail r is defined in the time domain as $a_{w,r}(t)$. The location of the wheelset w at time instant t is $x_w(t)$. Hence, after synchronization with the registered reference information in the BBMS system, such as GPS coordinates of reference kilometers, the acceleration signal can be evaluated as a function of the track location x or in the space domain as $a_{w,r}(x)$, where location x corresponds to the BBMS reference track kilometer positioning.

The number of $a_{w,r}$ data points per a 200 m track segment depends on the measurement speed. For instance, it could be up to 2.56×10^5 data points from one axle box when an average measurement speed is 20 m/s. In May 2019, two rounds of ABA measurement campaigns were conducted on the case study track segments. These two datasets are used for further analysis in the following sections.

Figure 4.3: The ABA measurement system instrumented on the dedicated wagon: (a) a GPS antenna (source of photo: TU Delft OpenCourseWare), (b) accelerometers attached to an axle box.

4.2.3.2. Scale average wavelet power of ABA signals

ABA signals have varied responses due to changes in speed, axle load, and track condition at particular locations. In this chapter, we used ABA signals from the dedicated instrumented wagon. Thus, it can be considered that the axle load of the instrumented wagon does not change significantly in different measurements. Therefore, the variations in ABA signals are mainly caused by speed and track conditions. Instead of directly utilizing ABA signals in the space domain, this study analyzes ABA signals in the space-spatial frequency domain, with the ABA signals being synchronized in the time domain with their corresponding position. The signals in the space-spatial frequency domain are converted from signals in the time-frequency domain. The spatial frequency corresponds to the inverse of the wavelength, calculated by dividing the measured frequency by the measured speed, obtained as in [111].

Since ABA signals are non-stationary signals, wavelet analysis is one of the well-known methods for analysis methods. In this chapter, ABA signals in the space domain are transformed into the space-spatial domain using the continuous wavelet transform (CWT)

[127]. The wavelet power spectrum (WPS) of ABA signals, a matrix of energy at a specific location (with respect to time synchronization) and frequency (relative to scale), is a product of CWT. Finally, the scale average wavelet power (SAWP) of ABA signals is calculated to investigate the variation of WPS within a considered frequency range along the segment. SAWP can be defined as follows:

$$SAWP_{w,r}(x) = \frac{\delta_j \delta_t}{C_\delta} \sum_{j=j1}^{j2} \frac{\left| \sum_{n'=0}^{N-1} a_{w,r}(n') \psi^* \left(\frac{(n'-n)\delta_t}{s_j} \right) \right|^2}{s_j} \qquad \text{Eq. 4.1}$$

where $SAWP_{w,r}(x)$ is the SAWP of ABA signal at wheel w and rail r, at location x and within the wavelet scale s from s_{j1} to s_{j2}, δ_j is the scale step, δ_t is the time interval between data points, C_δ is the empirically derived constant of the wavelet function, N is the number of data points in a considered space frame, $n' = 0, \dots , N\text{-}1$, $a_{w,r}(n')$ is the ABA signal at an instant location $x = n'$, n is the variable for the continuous translation, and Ψ is the wavelet mother function, in which the Morlet is selected in the chapter. The function Ψ^* is a family of wavelets derived from the mother wavelet by translations and scaling, and * refers to the complex conjugate.

According to the literature and findings from our previous studies, the vertical condition of the substructure layer is related to vertical track irregularities in the wavelength range of 3 – 25 m [111,118,119]. In addition, findings from the measurement campaign in [146] show that the variation of ballast layer properties exhibits a relationship with SAWP of ABA signals in the wavelength range of sleeper interval. Hence, in this chapter, we considered SAWP from two spatial frequencies (inverse of the wavelength). Firstly, $SAWP_S$ corresponds to the spatial frequency range of 0.04 m^{-1} to 0.33 m^{-1} or corresponding to irregularities in the wavelength from 3 m to 25 m, which is related to the condition of the substructure layer. Secondly, $SAWP_B$ corresponds to the spatial frequency range of 1.25 m^{-1} to 2.50 m^{-1} or corresponding to irregularities in the wavelength from 0.4 m to 0.8 m, which covers the 0.6 m of a nominal distance between sleepers in the Dutch railway lines, including ± 0.2 m of uncertainty bandwidth. In this range, SAWP is related to the condition of the ballast layer.

4.3. THE ENVTQI DESIGN

This section presents a framework for designing an EnVTQI of a considered track segment, a 200 m distance each for this chapter. The framework consists of three main steps: 1) ABA signal processing, 2) Feature extraction from SAWP of ABA signals and longitudinal levels, and 3) Feature fusion method for determining EnVTQI, as shown in Figure 4.4. A detailed description of each step can be found in the following subsections.

4.3.1. ABA SIGNALS PROCESSING

SAWP from two spatial frequency ranges, 3 m – 25 m, corresponding to the substructure layer, and 0.4 m – 0.8 m, corresponding to the ballast layer, are used for designing EnVTQI. However, calculating SAWP directly from measured ABA signals might consume unnecessary calculation efforts since the signals still contain irrelevant information, such as high-frequency contents corresponding to shortwave irregularities. Further, ABA signals are speed-dependent, so a method is needed to handle the consequences of the speed effect. Hence, processing steps on measured ABA signals should be conducted and are discussed in this section.

4.3.1.1. REDUCE SAMPLE SIZE AND ELIMINATE HIGH-FREQUENCY CONTENTS

According to the configuration of our ABA measurement system, ABA signals were recorded at the fixed sampling rate of 25.6 kHz to guarantee that the small defects on the rail surface were captured. According to the literature, responses of ballast and substructure layers are much lower in frequency [124–126]. Thus, a lower sampling rate can be considered for practical applications of ABA systems that analyze ballast and substructure layer-related problems. The fixed sampling rate makes the spatial resolution of ABA signals dependent on measurement speed. A higher speed of the instrumented wagon provides a lower spatial resolution. For example, for a typical train operational speed on the Dutch railway lines of 140 km/h (38.9 m/s), the lowest spatial resolution of ABA signals is 1.52×10^{-3} m. This resolution is much higher than the longitudinal levels, whose spatial resolution is 0.25 m. The relationship between passing frequency (f), wavelength (λ), and passing speed (v) is:
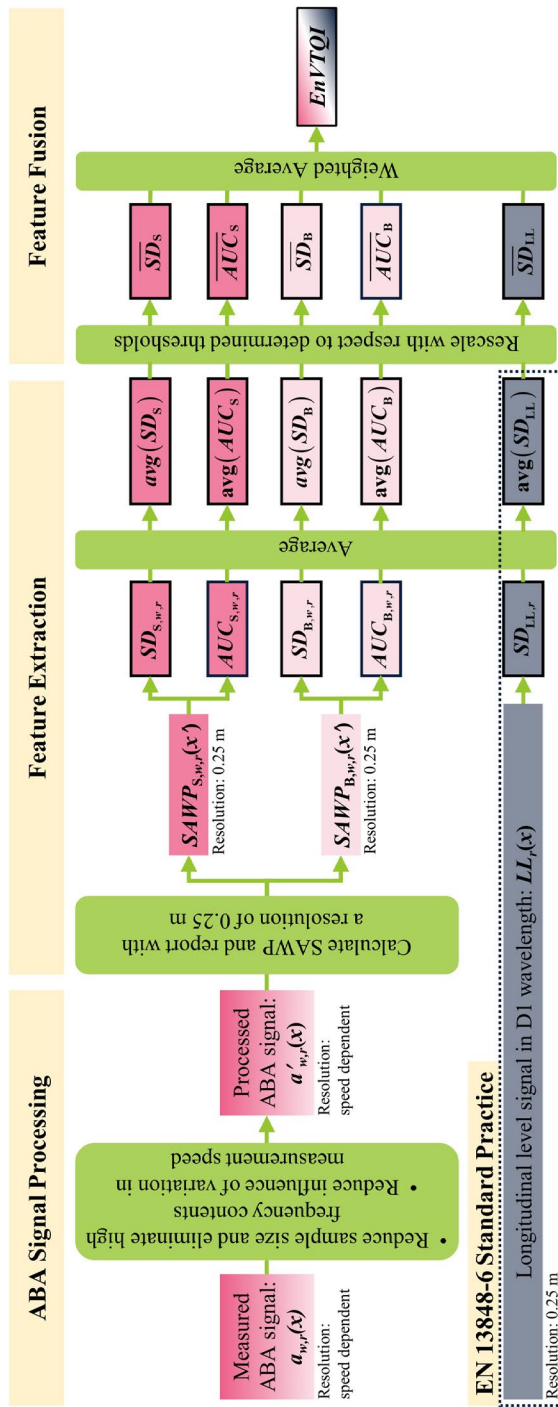
Figure 4.4: A framework for designing EnVTQI of a particular track segment.

$$f = \frac{v}{\lambda}$$ Eq. 4.2

The shortest considered wavelength for this study is 0.4 m. Regarding a typical train operational speed at 140 km/h (38.9 m/s), the highest corresponding frequency to be considered is 97.2 Hz. In this study, most measurements are below 100 km/h. The desired sampling rate and cutoff frequency must correspond to the operational speed. Thus, we consider a resampling from 25.6 kHz to 256 Hz by applying the standard MATLAB resample function [147] to reduce the sample size and a low pass filtering at 100 Hz. The processed signals are then used for the next steps.

4.3.1.2. REDUCE INFLUENCE FROM VARIATION IN MEASUREMENT SPEED

ABA responses are dependent on running speeds and changes in axle load. In this chapter, ABA signals are from our dedicated instrumented wagon, where the axle load can be considered nearly constant during different measurements. Therefore, we consider the effect of measurement speed to be an important source of variability. SAWP from different measurement speeds shows a similar pattern at a particular location [111]. However, the magnitude of SAWP is higher when the measurement speed is higher. Therefore, this step considers reducing the influence of variation in measurement speeds on the SAWP, making an EnVTQI evaluation independent of the measurement speed. We propose an approach to reduce the influence of speed as follows:

$$a'_{w,r}(x) = \frac{a_{w,r}(x)}{v^2}$$ Eq. 4.3

where $a'_{w,r}(x)$ is the processed ABA signal from wheel w and rail r at location x after reducing speed influence, $a_{w,r}(x)$ is the processed ABA from the previous step, and v^2 is the square of the average measurement speed when the instrumented wagon passes by the considered track segment.

The ABA signals at the right rail of segment II-24 are considered as an example to evaluate the performance of the proposed approach. Two measurements with average speeds of 21.6 m/s and 12.5 m/s were conducted on this segment on the same day of May 2019. Therefore, the condition of the track can be considered identical between the two

measurements. SAWP from ABA signals before and after reducing the influence of speeds are shown in Figure 4.5. It can be noticed that the similarity, especially magnitude, of $SAWP_S$ and $SAWP_B$ between the two measurements increases after reducing the influence of speed.
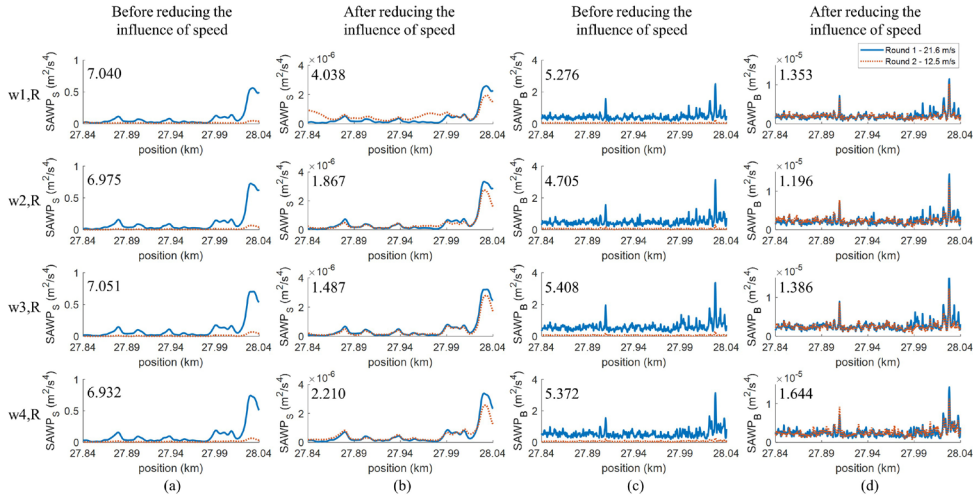

Figure 4.5: $SAWP_S$ and $SAWP_B$ of ABA signals at the right rail of the segment II-24: (a) and (c) before reducing the influence of speed, (b) and (d) after reducing the influence of speed. The top-left number is the scaled Euclidean distance between 2 corresponding signals.

The Euclidean distance is proposed as an indicator to assess the similarity between 2 signals, as follows.

$$d(\mathrm{p,q}) = \sqrt{\sum_{i=1}^{n}\left(q_i - p_i\right)^2} \qquad \text{Eq. 4.4}$$

where $d(\mathrm{p,q})$ is the Euclidean distance between signals p and q, p_i and q_i are the values of signal p and q at index i, and n is the signals p and q length. In this case, we consider SAWP for 200 m at the spatial resolution of 0.25 m, resulting in a similar signal length at 801 samples despite the difference in measurement speeds.

The lower distance between 2 signals suggests a higher similarity of those signals, while the zero distance indicates ideally similar signals. Please note that the magnitude of SAWP signals before and after reducing the influence of speed are different. Thus, scaling

on SAWP should be conducted before calculating the Euclidean distance to ensure a fair comparison. Figure 4.6 shows the example of $SAWP_{S,w3,R}$ before and after reducing the influence of speed and their corresponding scaled SAWP. The value in the top-left of the scaled SAWP plots (Figure 4.6(c) and (d)) corresponds to the scaled Euclidean distance. It can be indicated that the proposed method can reduce the influence of speed since the distance is reduced from 7.051 to 1.487, increasing the similarity between signals from two rounds of measurement. The scaled Euclidean distance between the signals of the remaining wheels can be found in Figure 4.5.

Regarding visual observation and the scaled Euclidean distance, it can be concluded that even though the influence of speed variation still occurs, it is significantly reduced by this proposed approach.
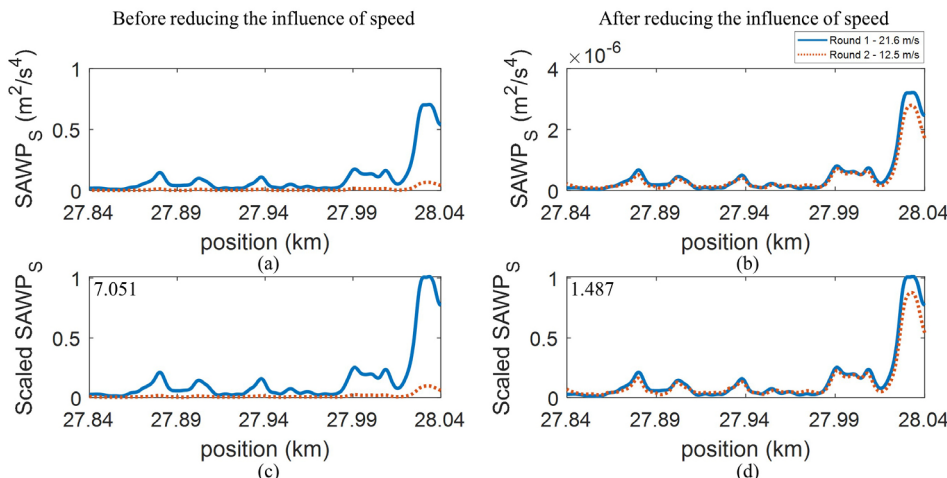

Figure 4.6: $SAWP$s of ABA signal from wheel 3, the right, at the segment II-24: (a) and (c) are before reducing the influence of speed, (b) and (d) after reducing the influence of speed, (c) and (d) scaled SAWP where the top-left number is corresponding to the scaled Euclidean distance.

4.3.2. FEATURE EXTRACTION FROM INPUT SIGNALS

In this step, we consider longitudinal levels and SAWPs of ABA signals as input signals. Then, the most relevant features are extracted from input signals to determine EnVTQI. The steps are discussed next.

4

4.3.2.1. FEATURE FROM LONGITUDINAL LEVELS

According to EN 13848-6 [90], the standard practice for quantifying the vertical track quality is based on the standard deviation of longitudinal levels. First, the quality of the measured longitudinal level datasets should be considered. Environmental factors, different measurement conditions, malfunctioning sensors, and other uncontrolled uncertainties might affect the measurement results, such as noise interference and position shifting [148]. Then, preprocessing, such as position alignment or removal of invalid measured values, is required to increase the accuracy of the standard deviation. Then, the standard deviation of the longitudinal level at the left rail, $SD_{LL,L}$, and the right rail, $SD_{LL,R}$, can be separately calculated as follows:

$$SD_k = \sqrt{\frac{\sum_{i=1}^{N}\left(k(x_i) - \bar{k}\right)^2}{N-1}}$$

Eq. 4.5

where SD_k is the standard deviation of signal k, $k(x_i)$ is the value of signal k at position x_i, $\bar{k}$ is the average value of signal k, and N is the data size of signal k. Then, $SD_{LL,L}$ and $SD_{LL,R}$ are averaged into a single value, $avg(SD_{LL})$, and it is considered as a representative feature from the longitudinal levels of a particular track segment.

4.3.2.2. SAWP CALCULATION

After reducing the influence of speed variation, the processed ABA signals, $a'_{w,r}(x)$, are inputs for SAWP calculation, according to Eq. 4.1. Then, $SAWP_{S,w,r}$, which corresponds to the condition of the substructure layer, and $SAWP_{B,w,r}$, which corresponds to the condition of the ballast layer, are obtained from eight ABA signals measured at eight corresponding axle boxes at wheelset w and rail r. Finally, the SAWP related to x' (same position as reported by the longitudinal level) is obtained with a 0.25 m spatial resolution as follows:

$$SAWP_{w,r}(x') = \frac{\sum_{n \in N} SAWP_{w,r}(x(n))}{|N|}, \ N = \left\{n, |x(n) - x'| \le 0.125\,\text{m}\right\}$$

Eq. 4.6

where $SAWP_{w,r}(x')$ is the SAWP of the ABA signal from wheel w and rail r at location x', in which x' is the same position as reported by longitudinal level signals at an interval of 0.25 m. The number of data points $|N|$ depends on the measurement speed. By selecting a similar spatial resolution between SAWP and the longitudinal level, we aim to produce a fusion of features that allows us to determine EnVTQI. In addition, a spatial resolution at 0.25 m is approximately half of the sleeper interval that is appropriate for detecting changes or defects in the level of an individual sleeper.

4.3.2.3. FEATURES FROM SAWP OF ABA SIGNALS

$SAWP_S$ and $SAWP_B$ are derived products of ABA signals related to substructure and ballast layers, respectively. For designing an enhanced track quality index for a particular track segment in which ABA signals are incorporated, the relevant features to track quality are extracted from SAWP. In this chapter, two types of handcraft features are considered as follows.

First, a variation of SAWP is considered. Good-quality track segments should provide less variation in track parameters. For example, according to EN 13848-6 [90], track segments that provide lower $avg(SD_{LL})$ are considered in better quality classes than segments with higher $avg(SD_{LL})$. Following the mentioned criteria, the standard deviation of SAWP is considered to be one of the handcraft features, which can be calculated using Eq. 4.6. Then, $SD_{S,w,r}$, the standard deviation of $SAWP_{S,w,r}$, and $SD_{B,w,r}$, the standard deviation of $SAWP_{B,w,r}$ corresponding to eight axle boxes at wheelset w rail r, are obtained.

Second, ABA energy is considered to be another handcraft feature. It has been reported that higher ABA energy can be found where severe conditions track components corresponding to various wavelength irregularities are located [111–113]. This criterion can be considered the principal characteristic of ABA signals. Thus, ABA energy corresponding to a particular track segment is considered and can be quantified by an area under the SAWP curve (AUC) as follows:

$$AUC_k = \sum_{i=1}^{N} \frac{(k(x_i) + k(x_{i+1}))\Delta x}{2}$$

Eq. 4.7

where AUC_k is the area under the curve of signal k, $k(x_i)$ and $k(x_{i+1})$ are the value of signal k at position x_i and the right after position x_{i+1}, Δx is the distance between position x_i and x_{i+1}.

After Eq. 4.7, $AUC_{\text{S},w,r}$, the area under the $SAWP_{\text{S},w,r}$ curve, and $AUC_{\text{B},w,r}$, the area under the $SAWP_{\text{B},w,r}$ corresponding to eight axle boxes at wheelset w rail r, are obtained. In total, the ABA signal from a particular axle box at wheelset w and rail r provides four handcraft features: $SD_{\text{S},w,r}$, $AUC_{\text{S},w,r}$, $SD_{\text{B},w,r}$, and $AUC_{\text{B},w,r}$. Figure 4.7 illustrates the correlations between $avg(SD_{\text{LL}})$ of the 48 case study track segments and handcraft features corresponding to ABA signals from the 8 axle boxes during measurement round 1 in 2019. All handcraft features show a positive Pearson correlation to $avg(SD_{\text{LL}})$, with a high correlation of 0.792 and 0.739 for $AUC_{\text{S},w,r}$ and $SD_{\text{S},w,r}$. From this analysis, we observe measurements that are outliers and features that are not highly correlated. These locations are interesting in this work, as they are characterized by ABA responses that deviate from $avg(SD_{\text{LL}})$, suggesting local phenomena not captured by track geometry.
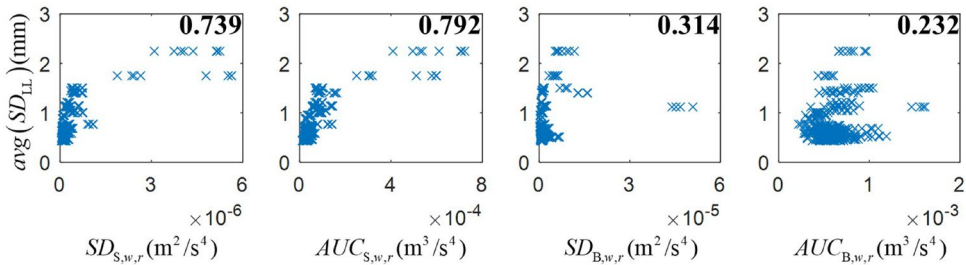

Figure 4.7: Correlation plots between the average standard deviation of longitudinal levels and features from $SAWP_{\text{S}}$ and $SAWP_{\text{B}}$. The top-right number is the Pearson correlation between the paired features of each subplot.

4.3.3. FEATURE FUSION

EnVTQI is determined by fusing features from longitudinal levels and ABA signals. EnVTQI is designed to be a single value representing the quality of the track for ease of implementation. According to EN 13848-6, $avg(SD_{\text{LL}})$ is calculated from longitudinal levels corresponding to two rails to represent a vertical TQI of a particular track segment. This principle is adopted in determining EnVTQI, as described next.

Each handcraft feature has eight values derived from signals of the four axle boxes on each rail. The eight values are aggregated from all the eight available wheelsets by averaging them. This approach reduces uncertainties in SAWP of ABA signals since we found in our previous study that ABA signals from different axle boxes show slight differences, such as slight shifting of SAWP peak locations and slight differences in SAWP magnitudes, even though they correspond to the same rail [111]. Figure 4.5 shows that different wheelsets exhibit slight variations in SAWP, for example, segment II-24. Table 4.1 shows the extracted features from different wheels and the EnVTQI while considering ABA signals from different wheelsets (see Figure 9). The results indicate that utilizing ABA signals from multiple wheelsets can reduce variations in EnVTQI related to different wheel conditions and measurement uncertainty.

Table 4.1: Extracted features of segment II-24 from ABA signals from different wheels.

| Features	Left Rail				
	w1	w2	w3	w4	avg
$SD_{S,w,r}$	4.46×10^{-7}	3.92×10^{-7}	3.70×10^{-7}	3.99×10^{-7}	4.02×10^{-7}
% diff from avg	11.02%	-2.35%	-7.99%	-0.68%	
$AUC_{S,w,r}$	9.10×10^{-5}	8.69×10^{-5}	8.32×10^{-5}	9.24×10^{-5}	8.84×10^{-5}
% diff from avg	2.97%	-1.71%	-5.79%	4.53%	
$SD_{B,w,r}$	9.06×10^{-7}	7.56×10^{-7}	8.66×10^{-7}	9.20×10^{-7}	8.62×10^{-7}
% diff from avg	5.13%	-12.34%	0.50%	6.71%	
$AUC_{B,w,r}$	4.28×10^{-4}	4.14×10^{-4}	3.77×10^{-4}	4.39×10^{-4}	4.14×10^{-4}
% diff from avg	3.37%	-0.18%	-9.03%	5.84%	
Features	Right Rail				
	w1	w2	w3	w4	avg
$SD_{S,w,r}$	5.74×10^{-7}	7.54×10^{-7}	7.29×10^{-7}	7.46×10^{-7}	7.01×10^{-7}
% diff from avg	-18.03%	7.54%	4.04%	6.45%	
$AUC_{S,w,r}$	7.77×10^{-5}	9.50×10^{-5}	9.51×10^{-5}	9.84×10^{-5}	9.15×10^{-5}
% diff from avg	-15.12%	3.75%	3.93%	7.45%	
$SD_{B,w,r}$	1.02×10^{-6}	1.14×10^{-6}	1.36×10^{-6}	1.30×10^{-6}	1.21×10^{-6}
% diff from avg	-15.36%	-5.48%	13.01%	7.83%	
$AUC_{B,w,r}$	4.00×10^{-4}	4.57×10^{-4}	5.42×10^{-4}	5.06×10^{-4}	4.76×10^{-4}
% diff from avg	-16.02%	-4.01%	13.84%	6.19%	
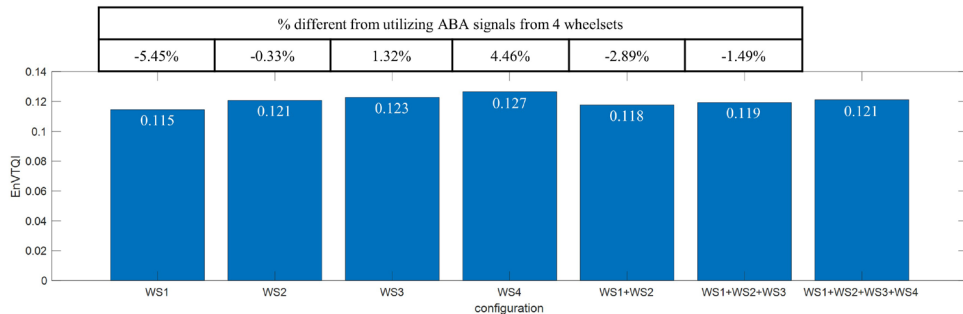
Figure 4.8: EnVTQI of segment II-24 regarding utilizing ABA signals from multiple wheelsets.

Then, five features are considered to determine the EnVTQI of a particular track segment. One feature is from the longitudinal level, $avg(SD_{LL})$, and four features are from SAWP of ABA signals, $avg(SD_S)$, $avg(AUC_S)$, $avg(SD_B)$, and $avg(AUC_B)$.

EnVTQI of a particular track segment is a single value obtained from the fusion of the five features. However, directly fusing all features might cause bias since the units and ranges of features are different, as shown in the x-axis of Figure 4.7. Therefore, the rescaling of each feature is applied. For a particular track segment, its corresponding features are rescaled with respect to the determined lower and upper values, as follows:

$$\overline{F}^{j} = \left(\frac{avg\left(F^{j}\right) - LV_{F}}{UV_{F} - LV_{F}} \right)$$

Eq. 4.8

where $\overline{F}^{j}$ is a rescaled value of feature F at segment j, $avg(F^{j})$ is an averaged value of feature F at segment j, LV_{F} and UV_{F} are the determined lower and upper values of feature F. Those boundary values can be adjusted to the measured track. For this chapter, the lower and upper values were determined based on observation from Figure 4.7.

Then, the five rescaled features of segment j, $\overline{SD}_{LL}^{j}$, $\overline{SD}_{S}^{j}$, $\overline{AUC}_{S}^{j}$, $\overline{SD}_{B}^{j}$, and $\overline{AUC}_{B}^{j}$ are fused into $EnVTQI^{j}$, as follows:

$$EnVTQI^{j} = \alpha_{1}\overline{SD}_{LL}^{j} + \alpha_{2}\overline{SD}_{S}^{j} + \alpha_{3}\overline{AUC}_{S}^{j} + \alpha_{4}\overline{SD}_{B}^{j} + \alpha_{5}\overline{AUC}_{B}^{j}, \ \alpha_{1} + \alpha_{2} + \alpha_{3} + \alpha_{4} + \alpha_{5} = 1$$

Eq. 4.9

where $EnVTQI^{j}$ is the enhanced vertical track quality index of track segment j, and α_{i} is the weight factor in the range between 0.00 to 1.00 of parameter i, in which the sum of α_{i} for

five features is 1. EnVTQI is unitless, where the segments with a lower EnVTQI value show a better track quality than those with a higher EnVTQI value. The procedure of tuning weight factors can be conducted following the reasoning behind the EN standard [90]. It also allows infrastructure managers to tune the importance of each handcraft feature. For instance, the weight of ballast-related features can be higher than substructure-related features in case the condition of the ballast layer requires more attention than the substructure. The weight of the substructure-related features can be set to 0.00 for some applications, such as planning for tamping.

Table 4.2: Lower and upper values per feature

Features F	Description	Lower and upper values				Unit
		With speed influence reduction		Without speed influence reduction		
		Lower LV_F	Upper UV_F	Lower LV_F	Upper UV_F	
$avg(SD_{LL})$	the average of the standard deviation of LL_r	3.0×10^{-1}	3.0×10^{0}	3.0×10^{-1}	3.0×10^{0}	mm
$avg(SD_S)$	the average of the standard deviation of $SAWP_{S,w,r}$	4.0×10^{-8}	6.0×10^{-6}	3.0×10^{-3}	1.0×10^{0}	m^2/s^4
$avg(AUC_S)$	the average of the area under the curve of $SAWP_{S,w,r}$	1.0×10^{-5}	7.5×10^{-4}	1.0×10^{0}	1.2×10^{2}	m^3/s^4
$avg(SD_B)$	the average of the standard deviation of $SAWP_{B,w,r}$	2.0×10^{-7}	5.5×10^{-5}	1.0×10^{-2}	1.5×10^{1}	m^2/s^4
$avg(AUC_B)$	the average of the area under the curve of $SAWP_{B,w,r}$	2.0×10^{-4}	2.0×10^{-3}	5.0×10^{1}	5.8×10^{2}	m^3/s^4

4.4. RESULTS AND DISCUSSION

4.4.1. VERTICAL TRACK QUALITY ANALYSIS

4.4.1.1. EN STANDARD INDICES

EN 13848-6 [90] defines two approaches to quantify track quality. The first approach considers the overall track quality index, defined as the Combined standard deviation (CoSD), which can be calculated as follows.

$$CoSD = \sqrt{\alpha_{AL}\, avg\left(SD_{AL}\right)^2 + \alpha_{G}\, SD_{G}^{\,2} + \alpha_{CL}\, SD_{CL}^{\,2} + \alpha_{LL}\, avg\left(SD_{LL}\right)^2} \qquad \text{Eq. 4.10}$$

where *CoSD* is the combined standard deviation, SD_i is the standard deviation of the geometry parameter i, α_i is the weight factor of the geometry parameter i, AL is alignment, G is track gauge, CL is cross level, and LL is longitudinal level. The second approach considers a particular track geometry parameter. For vertical track quality, the average standard deviation of the longitudinal levels of the left and right rails, $avg(SD_{LL})$, is considered.

Track geometry data from a measurement in 2019 is selected to discuss the track quality of the case study track segments. Forty-eight track segments, namely I-1 to I-24 for Track-1 and II-1 to II-24 for Track-II, are selected as case studies. CoSD is calculated with an equal weighting factor of 0.25 for each track geometry parameter, as in [97], which is shown in Figure 4.9(a), while $avg(SD_{LL})$ is shown in Figure 4.9(b).

Next, a comparison between CoSD and $avg(SD_{LL})$, is conducted. The CoSD values of all the 48 track segments range from 0.447 to 1.814. The five segments with higher CoSD values (ranked highest to lowest) are segments II-23, II-22, II-21, II-11, and I-10. These segments are highlighted as red bars in Figure 4.9(a). In comparison, the $avg(SD_{LL})$ values of the segments range from 0.435 to 2.247. Segment II-23 has the poorest vertical track condition with the highest $avg(SD_{LL})$ value. The following four track segments are II-22, I-10, II-16, and I-23, in descending order of severity. In addition, the changing patterns of track quality evaluated by CoSD and $avg(SD_{LL})$ are almost similar, as indicated by the arrows in Figure 4.9(a) and (b). The Pearson correlation between CoSD and $avg(SD_{LL})$ is 0.81. Furthermore, a similar distribution of their corresponding histograms of both indices can be observed. These findings align with the finding from [143] that the vertical track quality highly dominates the overall track quality. Hence, this chapter mainly focuses on the vertical track quality to represent overall track quality.
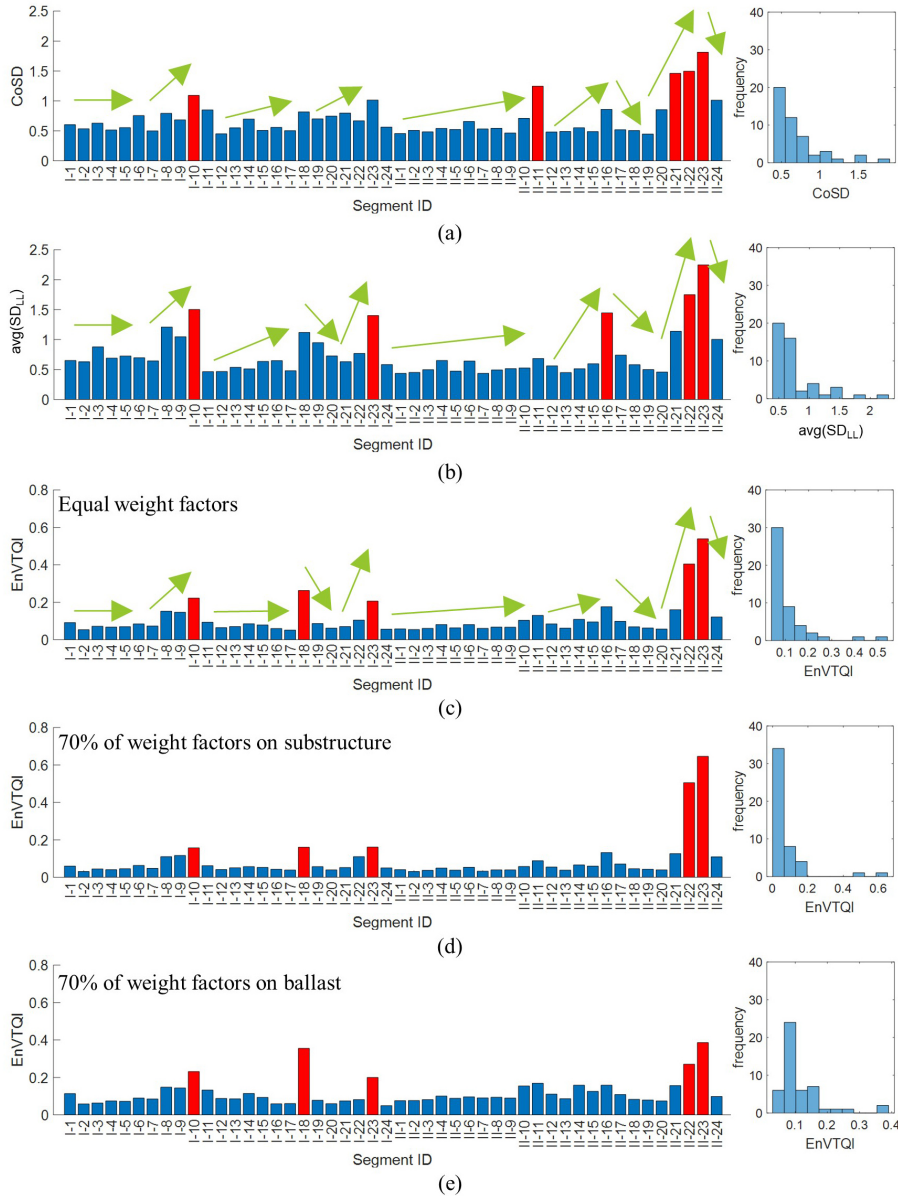
Figure 4.9: Track quality indices and its histogram of case study track segments based on measurement data in 2019: (a) CoSD where equal weight factors are assigned; (b) $avg(SD_{LL})$; (c) EnVTQI where equal weight factors are assigned; (d) EnVTQI where 70% of weight factors are assigned to substructure-related features; and (e) EnVTQI where 70% of weight factors are assigned to ballast-related features. Red bars indicate track segments with the worst 10% of all considered segments.

4.4.1.2. COMPARISON BETWEEN AVG(SD_{LL}) AND ENVTQI

The vertical track quality evaluated by EnVTQI for each case study track segment, calculated with an equal weight of 0.2 for each feature, is shown in Figure 4.9(c). We observe that $avg(SD_{LL})$ and EnVTQI indicate some segments have similar patterns. For instance, in Track-II, the track quality increases from II-16 to II-20, then the track quality drops from II-21 to II-23, and the track quality increases again in II-24. The Pearson correlation between $avg(SD_{LL})$ and EnVTQI is 0.91. Moreover, the histogram of EnVTQI shows good similarity to the histogram of $avg(SD_{LL})$.

There are segments of interest when comparing $avg(SD_{LL})$ and EnVTQI, such as Segments I-11 and I-12. From the perspective of longitudinal levels, the vertical track quality of segments I-11 and I-12 can be considered similar since the $avg(SD_{LL})$ values of I-11 and I-12 are 0.464 mm and 0.467 mm, respectively. However, based on the EnVTQI with equally assigned weighting factors in Figure 4.9(c), the track condition of segment I-11 is more severe than segment I-12 since $EnVTQI^{\text{I-11}}$ (0.093) is higher than $EnVTQI^{\text{I-12}}$ (0.064). While considering features for determining EnVTQI, all ABA-derived features corresponding to segment I-11 provide higher values than segment I-12, as shown in Table 4.3. Considering Figure 4.10(a-1), (a-2), (b-1), and (b-2), no noticeable changes in longitudinal level signals can be found in segments I-11 and I-12. In comparison, changes in $SAWP_S$ and $SAWP_B$ at track positions indicated by the dashed boxes in Figure 4.10(a-3) and (a-5) can be noticed, which leads to the higher ABA-derived features of segment I-11. These findings suggest that using ABA signals to assess track condition can enhance the standard practice of only considering track geometry.
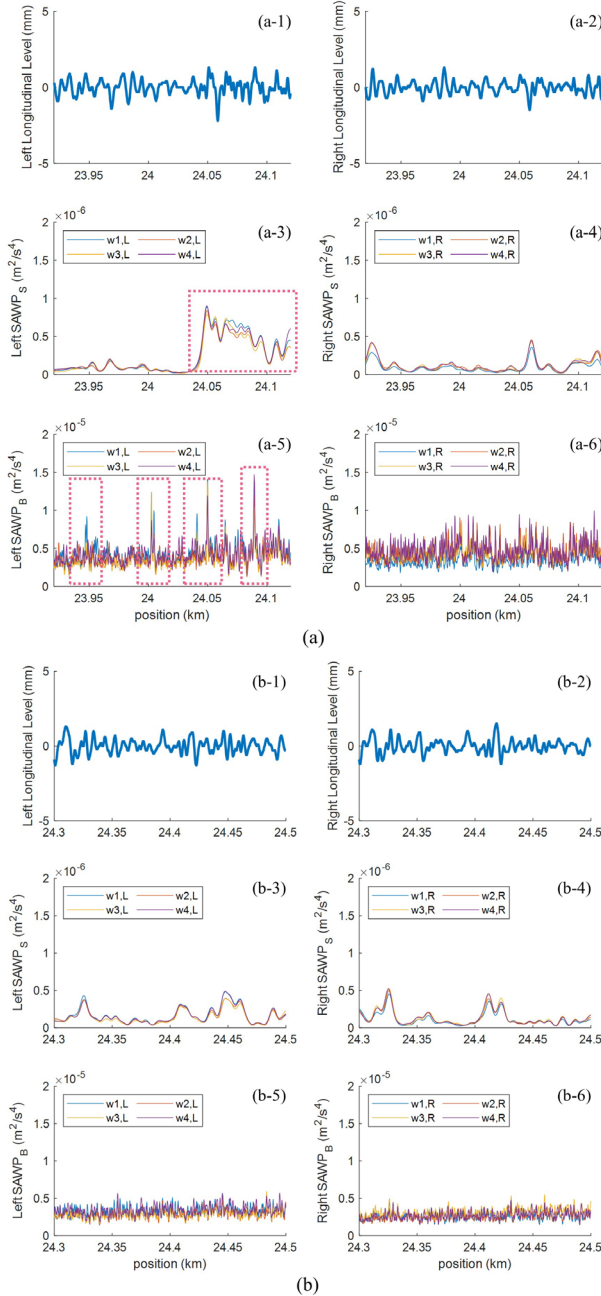
Figure 4.10: Signals corresponding to the track segment: (a) track segment I-11; (b) track segment I-12. Subfigures 1 and 2 are longitudinal levels at the left and right rails, subfigures 3 and 4 are SAWP$_S$ at the left and right rails, and subfigures 5 and 6 are SAWP$_B$ at the left and right rails.

Other locations of interest are I-18 and II-16. EnVTQI indicates that segment I-18 is one of the worst segments, instead of segment II-16 as indicated by $avg(SD_{LL})$. Considering longitudinal levels, it can be noticed from the dash boxes in Figure 4.11(b-1) and (b-2) that segment II-16 provides a higher variation of longitudinal levels than segment I-18. The values of $avg(SD_{LL})$ for II-16 and I-18 are 1.446 mm and 1.118 mm, respectively. In the case of EnVTQI, the $\overline{SD}_S$ and $\overline{AUC}_S$ corresponding to segment II-16 are higher than those of segment I-18, as shown in Table 4.3. The dashed boxes in Figure 4.11(b-3) and (b-4) indicate the locations with noticeable $SAWP_S$ peaks, which lead to the high values of the $\overline{SD}_S$ and $\overline{AUC}_S$. Thus, according to these features, the worst substructure condition is from segment II-16. However, features related to the ballast layer condition, $\overline{SD}_B$ and $\overline{AUC}_B$, of segment II-18 are significantly higher than those of segment II-16, as shown in Table 4.3.

In Figure 4.11(a-5) and (a-6), dash boxes indicate the locations that cause the high value of these features. The most noticeable peaks are located approximately at km 26.42, indicating the most severe spot in the ballast layer of segment II-18. This spot significantly dominates the overall track condition, leading to a higher value of $EnVTQI^{\text{I-18}}$ (0.263) than $EnVTQI^{\text{II-16}}$ (0.176). Regarding relative percentage differences, we observe more considerable variations for I-18 regarding the ballast features, so it is reasonable to suggest that the location faces a higher degradation condition. Finally, while EnVTQI provides aggregated information about track quality, the values required to calculate EnVTQI allow for identifying problematic track structure layers, allowing the physical interpretability of the results.
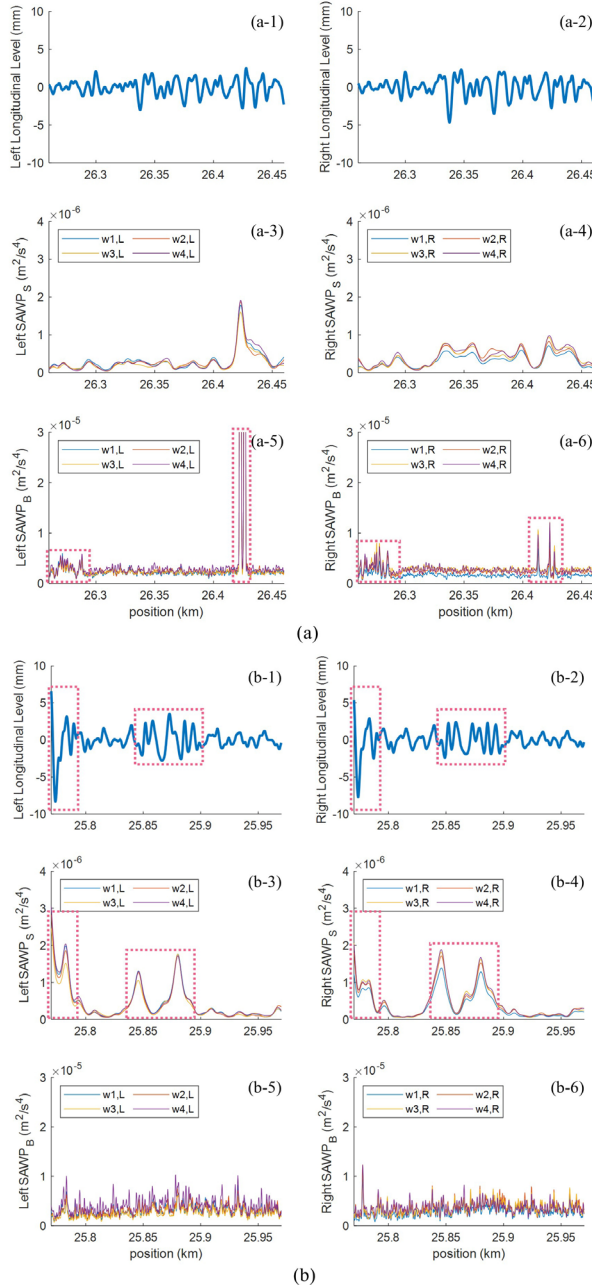
Figure 4.11: Signals corresponding to the track segment: (a) track segment I-18; (b) track segment II-16. Subfigures 1 and 2 are longitudinal levels at the left and right rails, subfigures 3 and 4 are SAWP_S at the left and right rails, and subfigures 5 and 6 are SAWP_B at the left and right rails.

Table 4.3: Parameters corresponding to considered track segments

Parameter	I-11	I-12	Relative difference (%)	Ratio I-11 : I-12	I-18	II-16	Relative difference (%)	Ratio I-18 : II-16
$avg(SD_{LL})$	0.464	0.467	0.6	0.99	1.119	1.446	29.2	0.77
$\overline{SD}_{LL}$	0.061	0.062	1.6	0.98	0.303	0.425	40.3	0.71
$\overline{SD}_{S}$	0.023	0.010	56.5	2.30	0.035	0.070	100.0	0.50
$\overline{AUC}_{S}$	0.038	0.027	28.9	1.41	0.081	0.106	30.9	0.76
$\overline{SD}_{B}$	0.017	0.006	64.7	2.83	0.431	0.018	95.8	23.94
$\overline{AUC}_{B}$	0.326	0.216	33.7	1.51	0.463	0.263	43.2	1.76
$EnVTQI$	0.093	0.064	31.2	1.45	0.263	0.176	33.1	1.49

4.4.2. EnVTQI UNDER SPEED VARIATION

ABA signals are speed-dependent, and in operational conditions, it is not possible to conduct ABA measurements with a constant speed for the whole railway line. In this subsection, the performance of the method to reduce the effect on speed is investigated. The average speed of the instrumented wagon passing by each track segment is calculated. The speed profiles from 2 measurement rounds along the case study railway line are shown in Figure 4.12(a). It can be noticed that the measurement speeds from the two rounds are different, especially from section I-1 to section I-22 and from section II-21 to section II-24. The lowest speed discrepancy is 0.2 m/s at segment II-20, while the highest speed variation is 9.7 m/s at segment I-18.

The EnVTQIs calculated from the ABA signals without and with speed influence reduction are shown in Figure 4.12(b) and (c), respectively. Without speed correction, considering segments I-10 and I-18 indicated by arrows in Figure 4.12(b), EnVTQI corresponding to measurement round 1 suggests that the condition of segment I-10 is more severe than that of segment I-18, while EnVTQI corresponding to measurement round 2 suggests the opposite result. The reason for this is that the speed of segment I-10 (23.9 m/s) is higher than that of segment I-18 (16.7 m/s) in measurement round 1, while the speeds of both segments can be considered similar (26.6 m/s for segment I-10 and 26.4 m/s for segment I-18) in measurement round 2. In measurement round 2, where speed differences can be neglected, it can be concluded that the condition of segment I-18 is more severe than

that of segment I-10. This is in line with the results evaluated by the EnVTQI with speed correction (Figure 4.12(c)). This simple example demonstrates the need and the capability of the proposed approach to reduce the influence of speed variation.

The total differences of EnVTQIs from the two ABA measurement rounds are 45.8 % if the proposed approach is not utilized. In contrast, the total differences are reduced to 6.6% after utilizing the proposed approach. Significant EnVTQI differences still exist in some track segments, for example, segment I-22, indicated by an arrow in Figure 4.12(c).
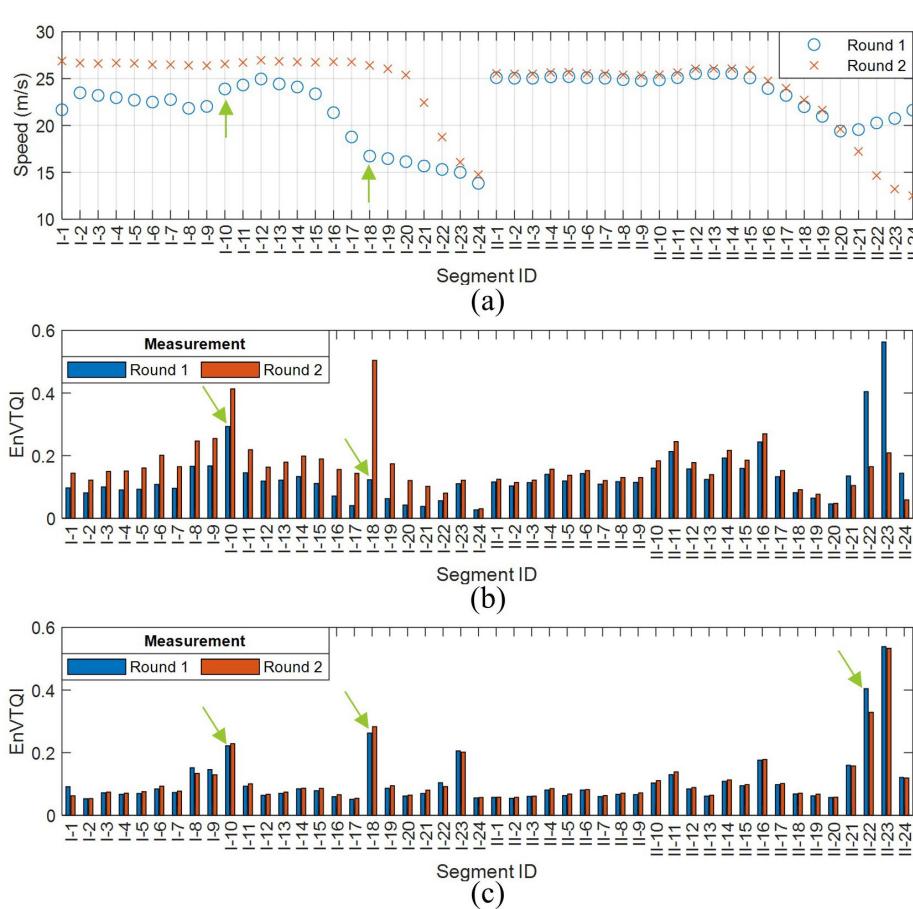
Figure 4.12: Comparison of EnVTQI between 2 rounds of ABA measurement: (a) measurement speeds from 2 rounds at a particular segment; (b) EnVTQI from ABA signals without reducing the influence of speed variation; (c) EnVTQI from ABA signals with reducing the influence of speed variation.

4.4.3. INFLUENCE OF WEIGHT FACTORS ON ENVTQI

Different assigned weight factors allow users to tune the importance of features that are α_1 for $\overline{SD}_{LL}$ related to longitudinal levels, α_2 for $\overline{SD}_S$ and α_3 for $\overline{AUC}_S$ related to the condition of the substructure layer, α_4 for $\overline{SD}_B$ and α_5 for $\overline{AUC}_B$ related to the condition of the ballast layer. Tuning weight factors makes EnVTQI better reflect track condition for a particular application, such as tamping, and better match the characteristics of a particular railway line. In this section, characteristics of EnVTQI regarding various assigned weight factors are investigated.

Figure 4.13 shows the EnVTQI of 48 case study segments based on various combinations of weight factors, in which one weight is set to 1.00, and the remaining weights are set to 0.00. The results demonstrate that different weight factor combinations yield different EnVTQI characteristics, indicating the differences in sensitivity of specific features and ballast and substructure conditions.

Three combinations of weight factors are tested, and their corresponding EnVTQI are shown in Figure 4.9. Firstly, equal weight factors of 0.20 are assigned to all features, and EnVTQI can be found in Figure 4.9(c). Secondly, 70% of the total weight is assigned to substructure-related features. The weight factors of rescaled $\overline{SD}_S$ and $\overline{AUC}_S$ are 0.35 each, while the weight factors of the remaining features are 0.10 each. The corresponding EnVTQI to this configuration can be found in Figure 4.9(d). Lastly, 70% of the total weight is assigned to ballast-related features. Weight factors of 0.35 are assigned to rescaled $\overline{SD}_B$ and $\overline{AUC}_B$, while the remaining features are assigned a weight factor of 0.10. The results of EnVTQI corresponding to this weight configuration are shown in Figure 4.9(e).

By determining the 10% of track segments with the highest EnVTQI, the same five segments, II-23, II-22, I-18, I-10, and I-23, are indicated by EnVTQI from three different weight configurations. Differences in the severity ranking and the magnitude of EnVTQI can be observed and shown in Table 4.4. In the case of high-weight factors assigned to substructure-related features, the severity of segments II-23 and II-22 are more distinguishable. In the case of high-weight factors assigned to ballast-related features,

segment I-18 is in the second rank, and its EnVTQI magnitude is close to segment II-23, the most severed segment. This finding agrees with the finding in Section 4.1.2 that a high $SAWP_B$ peak can be found at segment I-18.
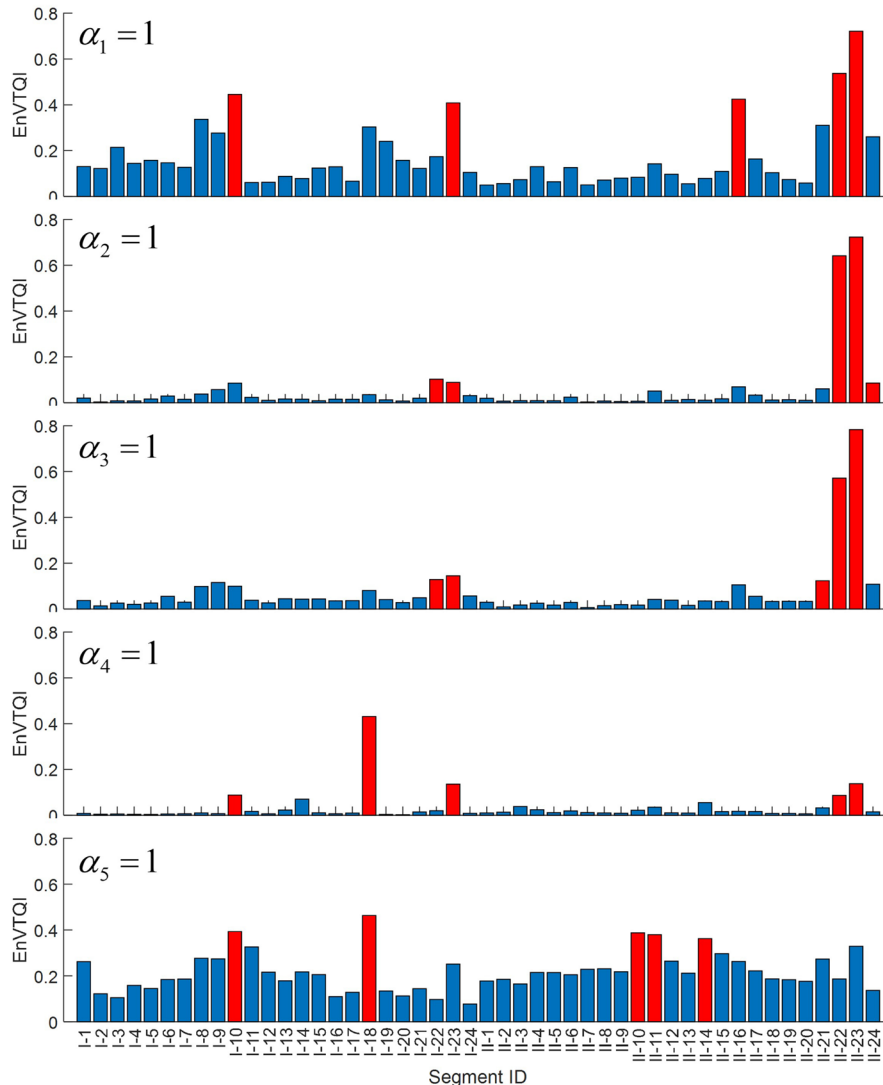

Figure 4.13: EnVTQI of the case study track segments in 2019 regarding different weight factors. Red bars indicate track segments with the worst 10% of all considered segments.

Table 4.4: The worst 10% track segments regarding three different weight configurations

Severity rank 1 to 5 from higher to lower severity	Segment and its EnVTQI					
	Equal weight		70% of the weight on substructure features		70% of the weight on ballast features	
1	II-23	0.539	II-23	0.646	II-23	0.386
2	II-22	0.405	II-22	0.505	I-18	0.355
3	I-18	0.263	I-23	0.161	II-22	0.271
4	I-10	0.222	I-18	0.160	I-10	0.231
5	I-23	0.206	I-10	0.157	I-23	0.200

4.4.4. EVOLUTION OF ENVTQI OVER TIME

Figure 4.14 shows historical longitudinal levels on a track that suggests a degradation pattern near the bridge from 2018 to 2021. The track quality in terms of $avg(SD_{LL})$, shown in Figure 4.15(b), continuously increased from 1.423 in 2018 to 2.742 in 2020 and then significantly dropped to 1.168 in 2021, meaning an improvement in track quality. This finding suggests that the major track maintenance activities were conducted between 2020 and 2021.
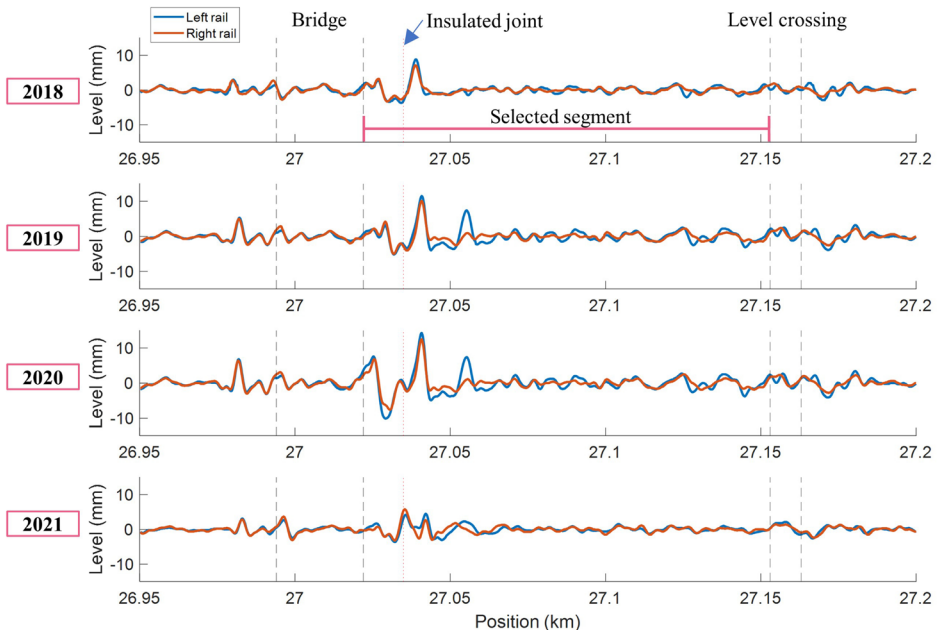
Figure 4.14: Evolution of longitudinal levels from 2018 to 2021.

Considering features from the available ABA signals measured in 2018, 2019, and 2021, drastic changes in SAWP can be observed near the bridge, as shown in Figure 4.15(a). Extracted features from $SAWP_S$ and $SAWP_B$ indicate the same trend as the longitudinal levels, where the feature values increase between 2018 and 2019 and later decrease in 2021, as shown in Figure 4.15(b). These changes over time resulted in the evolution of EnVTQI following a similar pattern. The EvTQI with equal weight factors for all inputs increased by 67.4% in 2019, showing worse track conditions than in 2018, and decreased by 57.4% in 2021, indicating better track conditions than in 2019.
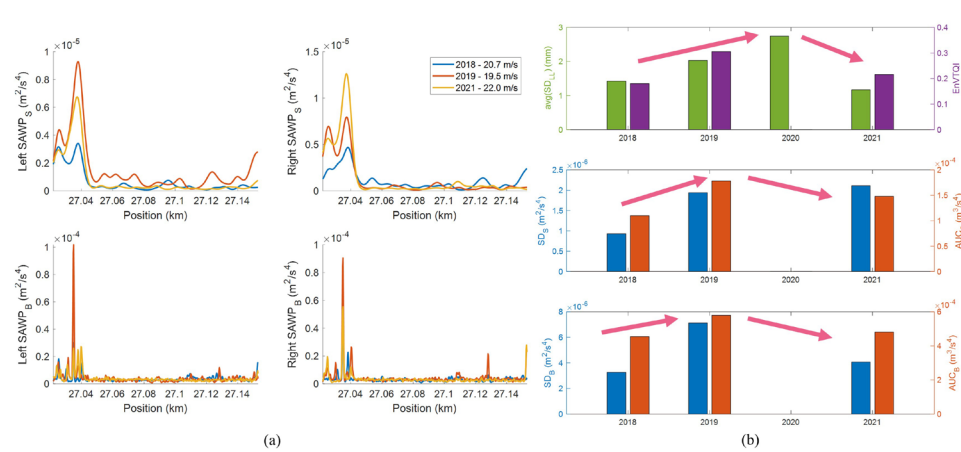
Figure 4.15: (a) $SAWP_S$ and $SAWP_B$ at the left and right rails from 3 different measurement years, (b) the evolution of EnVTQI and the corresponding features over time.

To support the abovementioned statement, the historical satellite images from 2018, 2019, and 2021, as shown in Figure 4.16, suggest evidence of track maintenance activities. Even though the exact types of track maintenance cannot be indicated, the changes in ballast appearance over time are due to new ballast placement, according to our track investigation in 2021. Differences in the satellite images between 2018 and 2019 indicate minor maintenance activities, especially near the bridge. Additionally, relatively major activities were conducted in 2021 since the widespread difference in ballast appearance between 2019 and 2021 can be observed, resulting in a significant improvement in track quality in 2021.

Figure 4.16: Historical satellite images of a considered segment
(source of satellite images: Google Earth).

4.5. CONCLUSIONS

A framework for designing an enhanced vertical track quality index, EnVTQI, is proposed. The proposed framework integrates features derived from longitudinal levels and ABA signals, in which two wavelengths of ABA signals are considered to identify track conditions at the substructure and ballast layers. In addition, this framework can be applied to railway networks with various measurement conditions, such as measurement speeds, because of the proposed approach to reducing the influence of speed variation.

The performance of EnVTQI is evaluated using measured datasets of the Dutch railway line by comparing EnVTQI with $avg(SD_{LL})$, an EN standard vertical TQI. The track condition of the study line is generally good. EnVTQI captures local changes in the condition of substructure and ballast layers, making it possible to perform better in indicating segments with poor track condition, including the effect of both deviations in track geometry and dynamic responses.

The proposed method to reduce the influence of variation in measurement speeds on ABA features is based on an empirical approach and allows the use of the EnVTQI considering train in normal operations.

5

CONCLUSIONS AND RECOMMENDATIONS

5.1. CONCLUSIONS

In this thesis, the main research question was formulated as follows.

"How can the track support condition be quantified using ABA signals and leverage this information to support maintenance decision-making?"

The three chapters of this thesis support the answer to this question. Characteristics of ABA signals under different track support conditions were investigated. Then, track support condition was quantified through ABA energy-based KPIs. The case studies in the Dutch, Swedish, and Norwegian railway lines indicate the capability to assess track support conditions using ABA signals in various track characteristics. Next, impact tests were performed to characterize the ABA responses, which provides a further understanding of the physical interpretation of ABA responses. Lastly, track support conditions quantified by ABA responses were leveraged to enhance the standard practice track condition assessment, which is valuable for infrastructure managers in supporting maintenance decision-making.

The findings of each chapter, corresponding to a particular sub-question, can be concluded as follows.

Sub-question 1: *What are the important characteristics of ABA signals, under different measurement conditions, regarding changes in track support condition?*

This sub-question is addressed in Chapter 2, which corresponds to the first half of the published journal paper [111]. The analyses of the ABA signals corresponding to track irregularities in the wavelength of 3 m to 25 m (or 0.04 m^{-1} to 0.33 m^{-1} in the spatial frequency) are conducted. Based on measured signals at the evaluated transition zones, the repeatability and consistency of the ABA responses are observed in the considered wavelength. Different ABA characteristics with respect to local changes can be indicated. Hence, these distributed characteristics pertain to each part of the transition zone and their health status. These findings suggest that the ABA measurement system is a promising technique for track support condition monitoring.

However, ABA responses vary when collected from different trains or with the same trains under different operational conditions, such as measurement speed. It is found that

ABA responses are speed-dependent; hence, higher measurement speed delivers stronger responses due to the higher excitation level. These variations in ABA responses must be taken into account during the interpretation of ABA responses for applications in track condition assessment.

Sub-question 2: *What method can be used to quantify the track support condition utilizing ABA signals?*

This sub-question is addressed in Chapter 2, which corresponds to the latter half of the published journal paper [111]. A framework for designing KPIs based on ABA signals is proposed for track support condition assessment at railway bridge transition zones. The proposed KPI methodology can be applied not only to the Dutch railway network, where the soils are very soft, but also to monitor other railway lines and other types of transition zones between soil and rigid structures.

We found that ABA energy-based KPIs allow the assessment of different degradation levels of transition zones from the large-scale level to the small-scale level, i.e., between different abutments of a particular bridge, between different tracks of a particular abutment, between different sides of a particular track, and between rails of a particular side. Furthermore, based on the case study, the highest degradation does not always occur at a specific abutment, track, side, or rail. In addition, the correlation between the KPIs from different measurement years and the track geometry-based quality index is found. However, locations where ABA indicates stronger responses, while track geometry does not show important variations, are observed.

Sub-question 3: *Can impact tests provide insights into the physical interpretability of the ABA signals?*

This sub-question is addressed in Chapter 3, which corresponds to the published journal paper [146]. Analysis of the interpretability of ABA responses is needed for better understanding and utilization of the ABA measurements. The vertical dynamic behavior of a railway bridge transition zone in a Swedish railway line is investigated with impact tests, including hammer tests and falling weight tests, as well as the trackside measurement techniques.

Impact tests provide information about important track characteristics, including track resonant frequencies and their corresponding magnitudes. We found that full track resonance shows variation along the transition zone, indicating changes in the ballast layer conditions. In addition, differences in track deflection characteristics along the transition zone can be found in ODSs from falling weight tests. This finding indicates different vertical dynamic responses between track segments outside and inside the bridge.

Next, ABA responses at the case study transition zone, at two spatial frequency ranges: 0.04 m^{-1} to 0.33 m^{-1} (prior knowledge) and 1.05 m^{-1} to 2.86 m^{-1} (corresponds to sleeper interval at 0.65 m including a range of uncertainty bandwidth) are analyzed. As expected, variations of ABA responses can be found at the transition zone. The highly deflected zone indicated by falling weight tests is at the same location indicated by ABA responses.

In addition, the ABA features in the spatial frequency range of 1.05 m^{-1} to 2.86 m^{-1} are found to be related to ballast layer conditions since a similar pattern can be observed between the ABA features and full track resonance features.

Sub-question 4: *How can ABA-based track support conditions be leveraged in supporting track maintenance decision-making?*

This sub-question is addressed in Chapter 4, which corresponds to the journal paper that is under review [149]. A framework to integrate ABA signals, which capture train-track interaction, and a track geometry parameter is proposed. In the proposed framework, the approach to reduce the influence of speed variation on ABA signals is included, allowing measured ABA signals from trains in normal operations to be utilized.

Features from ABA signals corresponding to two spatial frequency ranges: 0.04 m^{-1} to 0.33 m^{-1} (corresponds to substructure layer) and 1.25 m^{-1} to 2.50 m^{-1} (corresponds to sleeper interval at 0.60 m including a range of uncertainty bandwidth), and features from longitudinal level are extracted. Then, a new indicator, called EnVTQI (enhanced vertical track quality index), is determined by integrating the extracted features.

The performance of EnVTQI is evaluated using measured datasets of the Dutch railway line by comparing EnVTQI with $avg(SD_{LL})$, an EN standard vertical TQI. The track

condition of the study line is generally good. EnVTQI captures local changes in the condition of substructure and ballast layers, making it possible to perform better in indicating segments with poor track condition, including the effect of both deviations in track geometry and dynamic responses. In addition, the framework allows users to tune parameters to be matched with particular use cases, particularly to highlight the locations where conventional TQI does not indicate track quality problems.

5.2. Recommendations

5.2.1. Recommendations for future research

1. In Chapter 3, falling weight tests were conducted at only one impact location. In further works, additional extensive falling weight tests should be conducted to link its corresponding FRF features, which are expected to be related to substructure components, with ABA features in the range of 0.04 m^{-1} to 0.33 m^{-1}. The finding could support a statement that track irregularities in this frequency range are related to substructure component conditions.

2. Variations and uncertainty due to load and speed-dependent characteristics of ABA signals need further understanding since the railway track is non-linear. In Chapter 4, the method is proposed for reducing the influence of variation in measurement speeds on ABA features. However, it is based on an empirical approach. New methods in which knowledge of non-linear behaviors of a track is included, maybe via some combined physics and machine learning approach, should have more efficacy in reducing the effects of speed and load variation on ABA signals.

3. Analyzing the relationship between the ABA responses and other track inspection techniques, particularly from the field of soil dynamics, such as ground penetrating radar (GPR) and other possible in-situ measurements, can provide a better understanding and validation of the ABA responses concerning various aspects of the characteristics of track structure at different layers.

4. The findings of this study suggest that ABA signals can indicate differences in track support conditions. However, physical track parameters, such as stiffness and

damping, of the different layers of the track support have not been estimated in this work. Further development of a simulation model to validate ABA responses in the most lower part of the frequency responses is needed to address this issue.

5.2.2. RECOMMENDATIONS FOR RAILWAY INDUSTRY

1. CoSD, the overall track quality index according to EN 13848-6, was developed based on longitudinal level, alignment, gauge, and cross level. Those track geometry parameters correspond to the condition of railway tracks in both vertical and lateral directions. Therefore, an enhanced TQI derived from vertical, lateral, and longitudinal train-track interaction could be considered. The further developed TQI could provide a complete picture of track quality, especially for the segments located in curved tracks.

2. In order to make ABA measurements a source of information for track condition assessment, standardization is required. Further analysis with more case studies of track segments will cover the broader characteristics of railway track conditions. In addition, ABA signals from various configurations, such as different types of instrumented wagons, axle load, and weather and environmental conditions, require further analysis. The comprehensive analyses should make results interpreted from ABA signals more standardized and generic for infrastructure managers to apply for real-life applications.

6

APPENDIX A: ENVTQI CALCULATION TIME AND INFLUENCE OF SAWP RESOLUTION

In Chapter 4, the EnVTQI design allows users to resample ABA signals, which reduces the time required for EnVTQI calculations. Additionally, it allows for reporting SAWP, a derived product from ABA signals, at a lower spatial resolution to decrease data size. In this Appendix, we analyze the impact of ABA signal resampling on EnVTQI calculation time and the effect of low spatial resolution SAWP on EnVTQI results. The results indicate that three different resample rates (256 Hz, 512 Hz, and 1024 Hz) show insignificant differences in EnVTQI results. However, the 256 Hz resample rate has the shortest calculation time of 91.4 seconds. Regarding the low spatial resolution of SAWP, the reduction in resolution using the resampling approach shows less disturbance to EnVTQI than the wavelet decomposition approach. Nonetheless, it is important to note that the baseline spatial resolution of 0.25 m is appropriate. SAWP with a lower resolution than the baseline may result in information loss, particularly for local defects.

6.1. ENVTQI CALCULATION TIME

ABA signals have a high spatial resolution in the order of millimeters since they are measured with a high sampling rate of 25.6 kHz. As mentioned in Section 4.3, high spatial resolution is not essential for quantifying vertical track condition. The function of the EnVTQI design framework is to allow users to resample ABA signals to reduce calculation time. The characteristics of EnVTQI regarding different resampling rates of measured ABA signals are investigated in this subsection.

Three resampling rates of ABA signals, 256 Hz, 512 Hz, and 1024 Hz, are considered. The code for determining EnVTQI is developed in MATLAB 2021b and executed on a workstation with a 14 cores-CPU, Intel(R) Xenon(R) Gold 5120 2.20 Hz, and 64 GB of RAM. Then, the calculation time from reading measured ABA signals to determining EnVTQI with assigned equal weight factors for all 48 track segments is observed.
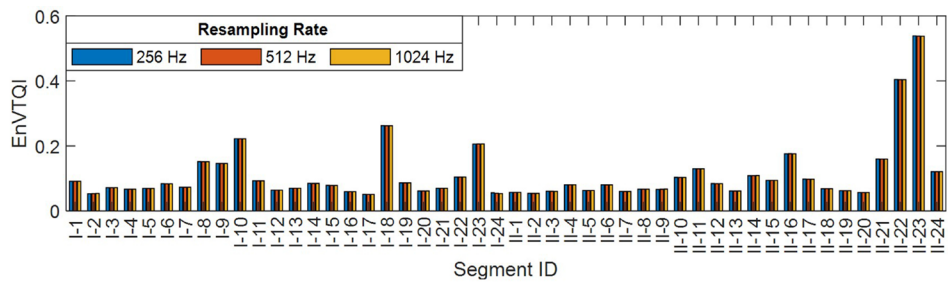
Figure 6.1: Comparison of EnVTQI from different resampling rates of measured ABA signals.

EnVTQI of 48 track segments regarding three different resampling rates are shown in Figure 6.1. Regarding the computational time, EnVTQI corresponds to a configuration with a 256 Hz resampling rate, and the baseline consumes 91.4 seconds. Meanwhile, EnVTQI, regarding a configuration with a 512 Hz resampling rate, consumes 116.6 seconds, which is 27.6% higher than the baseline. EnVTQI, corresponding to a configuration with a 1024 Hz resampling rate, consumes 177.7 seconds, 94.4% higher than the baseline. In addition, as shown in Figure 6.1, the EnVTQI of a particular track segment from three different resampling rates can be considered similar. The total percentage differences from a baseline configuration are 0.18% and 0.23%, in the case of 512 Hz and 1024 Hz resampling rates, respectively. These findings indicate that calculation time in determining EnVTQI can be

reduced by tuning the resampling rate of measured ABA signals. However, a resampling rate that is too low leads to a loss of information from ABA signals, as discussed in Section 4.3.1.1.

6.2. INFLUENCE OF SAWP SPATIAL RESOLUTION ON ENVTQI

Longitudinal level signals are reported with a spatial resolution of 0.25 m regarding a standard practice. Hence, we considered reporting SAWP of ABA signals with a similar 0.25 m spatial resolution. However, due to the framework for designing EnVTQI, reporting SAWP with a lower spatial resolution is possible, resulting in less data storage required. In this subsection, we investigated the influence of a low spatial resolution SAWP on the changes in EnVTQI as follows.

Two approaches for reducing SAWP spatial resolution are investigated. The first approach is wavelet decomposition, in which 'wavedec', a standard MATLAB function [150], is utilized. For the first iteration, the original SAWP is decomposed into two sets: approximation coefficient, containing low-frequency contents of the signal, and detail coefficient, containing high-frequency contents. The sample size of approximation and detail coefficients is reduced to half of the original signal, making a spatial resolution two times lower than the original signal. Then, in the next iteration, the approximation coefficient from the former iterations is decomposed using the same procedure as in [150]. According to the wavelet decomposition procedure, we consider approximation coefficients to represent SAWP after reducing spatial resolution since the shape of SAWP remains similar. We consider approximation coefficients from six iterations, in which a spatial resolution of SAWP reduces from 0.25 m (baseline) to approximately 16 m at the sixth iteration.

The second approach is to resample, in which 'resample', a standard MATLAB function [147], is considered. SAWP is resampled from a spatial resolution of 0.25 m, equivalent to 801 data points within 200 m, into a lower desired number of data points. Following wavelet decomposition, we determine that the spatial resolution of SAWP decreases two times for each iteration. Finally, six resampled SAWPs corresponding to a spatial resolution from 0.25 m to 16 m are considered.

6
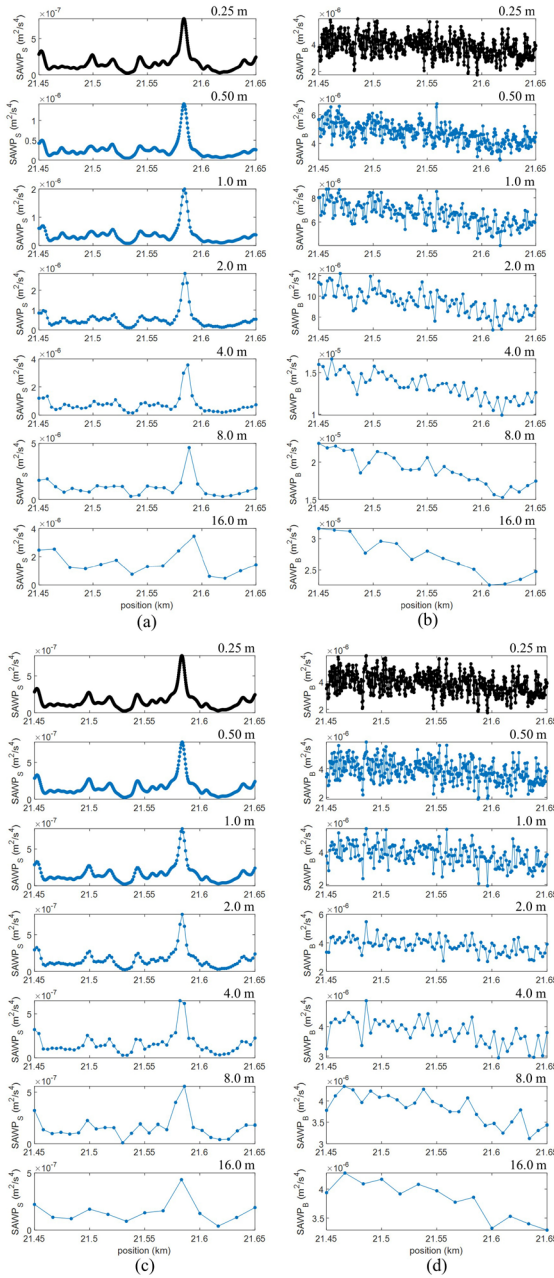
Figure 6.2: Comparison of SAWP$_S$ and SAWP$_B$ of segment I-1 between baseline and after spatial resolution reduction: (a) and (b) SAWP$_S$ and SAWP$_B$ from the wavelet decomposition approach; (c) and (d) SAWP$_S$ and SAWP$_B$ from the resampling approach. The value at the top right of each subplot represents an approximate spatial resolution of that case.

The characteristics of SAWP after reducing a spatial resolution based on the two mentioned approaches are analyzed. $SAWP_S$ and $SAWP_B$ of segment I-1 corresponding to the ABA signal from wheelset 1, left rail, from measurement round 1, are shown in Figure 6.2. The figure consists of a baseline SAWP with a spatial resolution of 0.25 m and their corresponding SAWPs after reducing a spatial resolution from two proposed approaches. It can be seen that the magnitude of SAWP is changed after reducing spatial resolution using wavelet decomposition. For example, in Figure 6.2(a), the magnitude of $SAWP_S$ increases from 7.8×10^{-7} m^2/s^4 in the baseline condition to 3.5×10^{-6} m^2/s^4 in the condition of 16 m of a spatial resolution. Meanwhile, in Figure 6.2(c), the resampling approach provides significantly less magnitude change from 7.8×10^{-7} m^2/s^4 in the baseline condition to 4.4×10^{-7} m^2/s^4 in the case of 16 m of a spatial resolution.

Then, ABA signals, with the influence of speed variation reduction from measurement round 1, are selected as considered examples. EnVTQI with assigned equal weight factors is calculated based on each pair of a combination between $SAWP_S$ and $SAWP_B$ from different spatial resolutions. In total, 36 EnVTQI values from each spatial resolution reduction approach at a particular track segment are in consideration. Figure 6.3(a) and (b) show examples of a comparison between EnVTQI from baseline $SAWP_S$ and $SAWP_B$, 0.25 m of a spatial resolution, and EnVTQI from $SAWP_S$ and $SAWP_B$ with 16 m of a spatial resolution, using wavelet decomposition and resampling approaches, respectively.

Reducing spatial resolution using the wavelet decomposition approach significantly disturbs the characteristics of SAWP. Even though SAWP in the lower spatial resolution follows the pattern of the baseline SAWP, the magnitude is changed significantly. Consequently, features corresponding to SAWP with reduced spatial resolution deviate from the baseline SAWP, making drastic differences in EnVTQI results, shown in Table 6.1, up to 633 % of total differences from the baseline EnVTQI. The resampling approach also disturbs the characteristics of a reduced spatial resolution SAWP. However, the level of deviation from the baseline SAWP is less than that of the wavelet decomposition approach. The maximum total difference of EnVTQI is 3.96 %, as shown in Table 6.2, which is significantly less than that from the wavelet decomposition approach. However, an inappropriate spatial resolution of SAWP, lower than the baseline, leads to a loss of

information, especially for local defects whose irregularity wavelength is shorter than a
reduced spatial resolution. For example, in Figure 6.3(b), differences between EnVTQI can
be noticed in segment I-18, in which strong peaks in $SAWP_B$ are found in Figure 4.9(a).

(a)

(b)
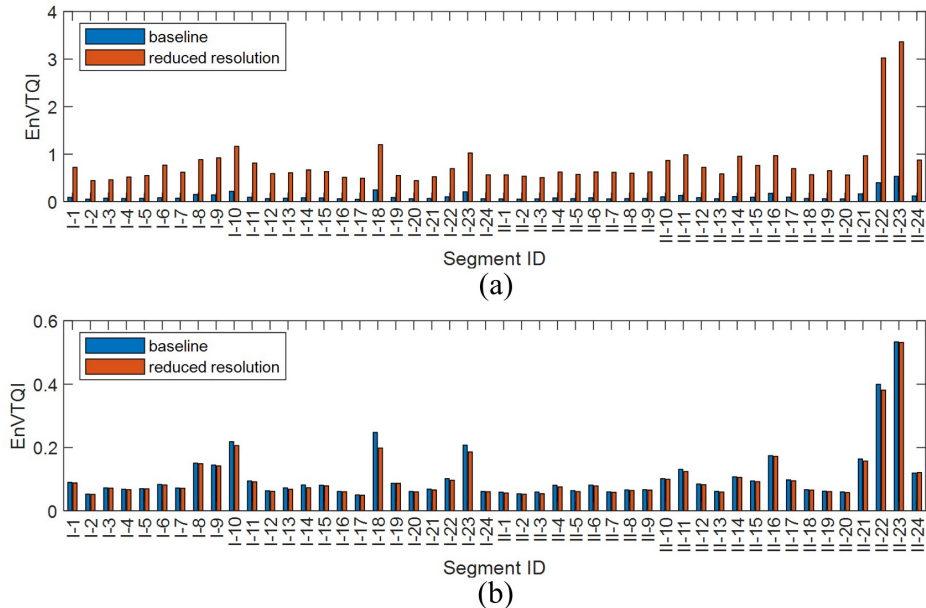
Figure 6.3: EnVTQI from SAWP$_S$ and SAWP$_B$ with 0.25 m spatial resolution and with a reduced
spatial resolution to 16 m: (a) spatial resolution reduction using a wavelet decomposition approach,
(b) spatial resolution reduction using a resampling approach.

Table 6.1: Total percentage differences between EnVTQI from SAWP with a 0.25 m of spatial
resolution and EnVTQI from SAWP with a reduced spatial resolution regarding the wavelet
decomposition approach

		Spatial resolution of $SAWP_B$ (m)					
		0.50	1.0	2.0	4.0	8.0	16.0
Spatial resolution of $SAWP_S$ (m)	0.50	36.4	74.1	125.0	198.0	301.2	447.6
	1.0	52.1	89.8	140.7	213.7	316.9	463.3
	2.0	74.5	112.2	163.1	236.1	339.3	485.7
	4.0	106.7	144.4	195.3	268.3	371.6	517.9
	8.0	152.9	190.6	241.5	314.5	417.7	564.1
	16.0	222.2	259.9	310.8	383.8	487.0	633.4

Table 6.2: Total percentage differences between EnVTQI from SAWP with a 0.25 m of spatial resolution and EnVTQI from SAWP with a reduced spatial resolution regarding the resampling approach

		Spatial resolution of $SAWP_B$ (m)					
		0.50	**1.0**	**2.0**	**4.0**	**8.0**	**16.0**
Spatial resolution of $SAWP_S$ (m)	**0.50**	0.13	0.47	1.48	2.37	3.03	3.52
	1.0	0.12	0.45	1.43	2.32	2.98	3.47
	2.0	0.15	0.45	1.37	2.24	2.89	3.38
	4.0	0.28	0.46	1.31	2.16	2.81	3.29
	8.0	0.45	0.65	1.41	2.22	2.87	3.35
	16.0	1.02	1.29	2.20	2.83	3.48	3.96

In addition, the total percentage difference of EnVTQI between the baseline configuration and SAWP with a reduced spatial resolution using the resampling approach is relatively low, even though a spatial resolution at 16 m is considered. That is possible because the track quality of this railway line can be considered in good condition. Hence, drastic differences in EnVTQI regarding low spatial resolution cannot be significantly pronounced. Therefore, working with a baseline spatial resolution at 0.25 m is recommended for determining EnVTQI. At this level of spatial resolution at 0.25 m, the SAWP of ABA signals provides information at the same level as longitudinal level signals. In addition, it offers affordable EnVTQI calculation time consumption while maintaining sufficient train-track interaction information.

6

7

APPENDIX B: MONITORING OF DUTCH, SWEDISH, AND NORWEGIAN TRANSITION ZONES

Railway transition zones connecting conventional embankments and rigid structures, such as bridges and tunnels, usually degrade much faster than other railway sections. Efficient health condition monitoring of transition zones is important for preventative track maintenance. In this chapter, a methodology for monitoring railway transition zones using acceleration measurements on multiple axle boxes (multi-ABA) of a passing train is presented. To showcase its capability, the measurements in the Netherlands, Sweden and Norway are analyzed and discussed. It is found that different bridges and transition zones exhibit unique characteristics including dominant wavelengths and energy distribution. Based on these unique characteristics, the geometry and support conditions at different locations of a transition zone can be evaluated. Higher train speed makes the characteristics more pronounced. The results demonstrate that the multi-ABA measurement has the potential to evaluate and thus monitor the health conditions of various transition zones.

7.1. Introduction

Railway transition zones are track segments connecting conventional embankments and other civil structures, such as bridges, tunnels, and culverts. Track conditions usually degrade much faster at transition zones than those at other locations due to significant variation in track support properties. For example, in the Netherlands, the maintenance frequency at transition zones can be more than two times higher than that at other track sections [38]. Such frequent maintenance is not only very costly but also largely reduces track availability. Therefore, effective monitoring of transition zones is important for preventative and efficient track maintenance.

In the literature, to monitor the health conditions of railway transition zones, trackside measurement techniques are commonly used. Coelho, et al. [47] measured the passenger train-induced dynamic responses of a typical Dutch transition zone linking a conventional track and a concrete culvert. The track settlements and pore water pressures were monitored over one year. Stark, et al. [33] reported an instrumentation program which included the measurements of wheel and tie loads, and the permanent and transient vertical displacements as a function of depth at three bridge approach sites in a high-speed line in the United States. Ribeiro, et al. [48] measured the dynamic behavior at a culvert transition zone in Portugal. The experimental work consisted of hammer test, dynamic tests under railway traffic and the corresponding dynamic responses of the train. More measurements on transition zones can be found in [67,72]. In general, the track-side measurements can capture many details of the transition zones, thus giving specific solutions to the problems. However, such techniques are expensive when multiple transition zones at the network level need to be monitored.

Alternatively, onboard measurement methods, such as axle box acceleration (ABA) measurements, have the potential to enable more efficient condition monitoring of transition zones. The ABA measurement method was developed to detect track defects, such as squats [105] and joint bolt tightness [114]. These defects are generally with short wavelengths. In the present work, the ABA measurement method is extended to be applied to transition zones with relatively longer wavelengths. However, since the design and construction of different transition zones vary significantly, it is challenging to develop a

robust method that is applicable to monitoring different transition zones. To achieve this, an in-depth understanding of ABA measurements at different transition zones is essential.

In this chapter, we present a methodology for monitoring transition zones of railway bridges using acceleration measurements on multiple axle boxes (multi-ABA) of a passing train. The measurements in the Netherlands, Sweden and Norway are presented as case studies to show the potential of multi-ABA for evaluating the health conditions of railway transition zones.

7.2. ABA MEASUREMENT SYSTEM AND DATA ANALYSIS METHOD

The ABA measurement system consists of accelerometers on multiple axle boxes, a GPS antenna and a tachometer, as shown in Figure 7.1. The GPS antenna is on the train roof to record the train's location. The tachometer records the train speed and also helps identify the train's position especially in mountainous areas. The sampling frequency of the accelerations is set to 25.6 kHz to acquire sufficient information over a broad range of train speeds. In the present work, focus is on the sleepers, ballast layer and substructures at the transition zones in low frequency range, usually below 200 Hz.

Figure 7.1: Multi-ABA measurement system (source of photos: TU Delft OpenCourseWare).

The responses at a transition zone are highly location-dependent. Therefore, the continuous wavelet transform (CWT) method is employed to analyze the axle box accelerations. In CWT, the convolutions of an acceleration are calculated with a group of scaled and shifted wavelet functions. The wavelet coefficient of the acceleration signal $a_{w,r}$ from wheel w and rail r at location x and wavelet scale s ($s>0$) is [105]:

$$CWT_{w,r}(x,s) = \sum_{n=0}^{N-1} a_{w,r}(n)\psi^*\left(\frac{(n-n')\delta_t}{s}\right)$$ Eq. 7.1

where ψ is the mother wavelet and the Morlet function is employed here. * denotes a complex conjugate and ψ^* is a family of wavelets derived from the mother wavelet by various translation and scaling steps. N is the number of points in the time series, $n = 0, 1,$ ..., N-1. n' is the continuous variable for the translation, δ_t is the time step.

With multiple-ABA measurements, the acceleration signal $a_{w,r}$ is obtained by averaging the ABAs from 4 wheelsets. In this way, the uncertainty is much less reduced [111]. The wavelet power spectrum (WPS) is defined as the square of the absolute wavelet coefficient:

$$WPS_{w,r}(x,s) = \left|CWT_{w,r}(x,s)\right|^2$$ Eq. 7.2

A scalogram is used to visualize the WPS as a function of position and wavelength. The wavelength is obtained from the measured frequency and the train speed.

7.3. Case studies

7.3.1. Measurements in the Netherlands

In the Netherlands, two measurement campaigns were conducted in 2019 between Dordrecht station and Lage Zwaluwe station. There are 9 bridges crossing over rivers and pavements between these two railway stations. More information can be found in the authors' previous work [111]. In the present work, the measurements at the transition zones of a typical bridge are introduced as shown in Figure 7.2.

The bridge is about 28 meters long carrying two ballasted tracks. One of the tracks, as shown with the dashed blue box in Figure 7.2(a), is selected because the two measurements on this track are under different train speeds. It can be seen in Figure 7.2(b) that, the ABA signals of the two measurements are generally quite similar in shape and trends, but the amplitudes are train speed dependent. The higher train speed results in the larger acceleration amplitude. The insulated joint can be identified.
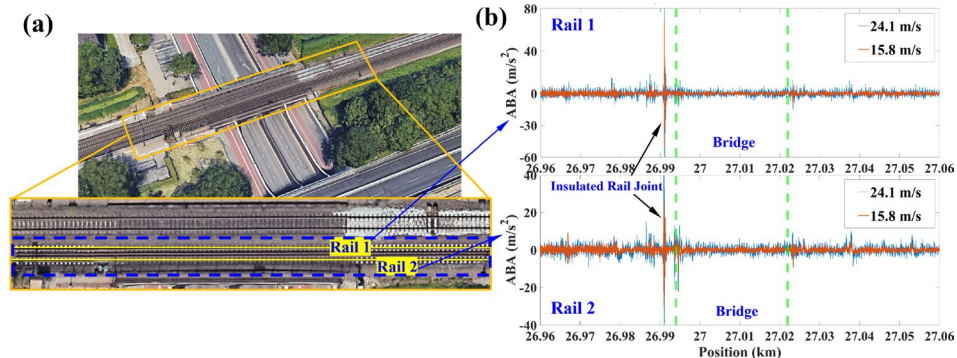
Figure 7.2: Aerial photos of the transition zones and time histories of ABA measurements (source of aerial photos: Google Earth).

Figure 7.3 shows the corresponding WPS of the ABA measurements on the two rails at the transition zones. In Figure 7.3, with wavelet analysis, the dominant wavelengths at the transition zones are visible at the high-energy areas. For example, the wavelength of about 0.6 m should be related to the sleeper interval. The sharp spike with broad short wavelength range is the impact induced by a local rail surface irregularity [104], such as an insulated rail joint in this case. The other strong responses with wavelengths longer than 1 m are probably related to the ballast layer and substructures.
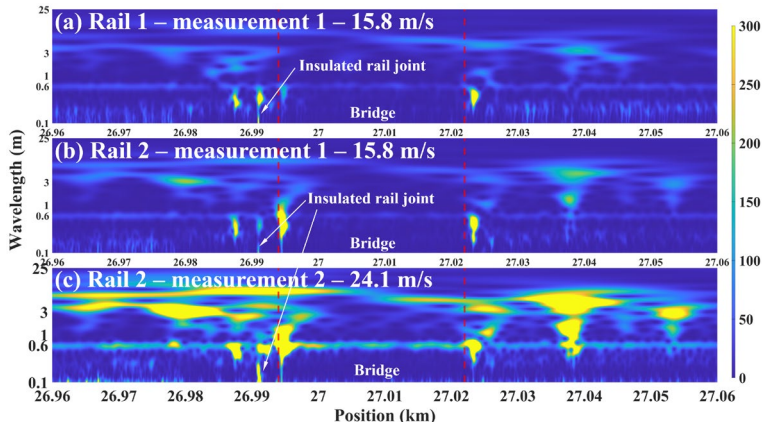
Figure 7.3: WPS of the ABA measurements.

It can be seen from Figure 7.3(a) and (b) that, even though at the same track, the WPS of the measurements at the two rails can be slightly different in terms of the wavelength

ranging from 1 to 25 m. It means that the ABA measurement is capable of identifying the slight difference of the supports at the two rails int terms of middle and long wavelength irregularities. With comparison in Figure 7.3(b) and (c), it shows more clearly that train speed only affects the amplitude rather than the wavelength contents.

7.3.2. MEASUREMENT IN SWEDEN

In Sweden, the ABA measurement was conducted in a mixed traffic line between Boden station and Murjek station. This railway line has only one ballasted track. As shown in Figure 7.4(a), there is a culvert, with the length of 8.15 m in total, including a 4.2 m deck and two approach slabs at the two sides, each with the length of about 2 m. There were cracks found at the culvert abutment, so two steel beams were installed to help support the deck.

(a)
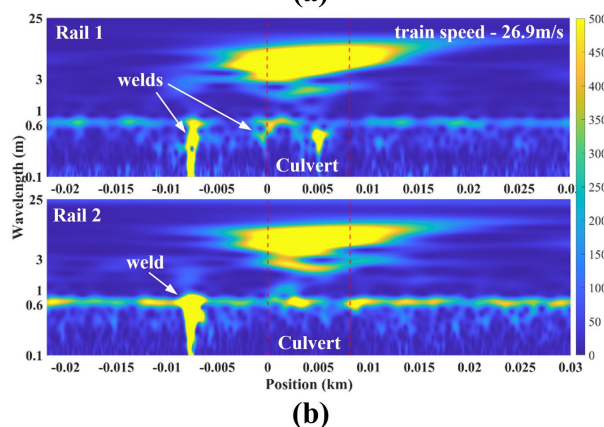
(b)

Figure 7.4: ABA measurement at a culvert in Sweden.

The WPS of the ABA measurement over this culvert and the transition zones is shown in Figure 7.4(b). It can be seen in Figure 7.4(b) that, the effects of the welds can be easily identified. The sleeper interval related patterns are obvious. One unique characteristic is that quite strong response on the culvert is found, as shown with the large high energy areas both at rail 1 and rail 2 in wavelength range from about 3 m to 10 m. This is probably because of the dynamic characteristics of the degraded culvert structure. The origin of the dynamic characteristics can be verified by in-track tests, such as hammer tests.

7.3.3. MEASUREMENT IN NORWAY

In Norway, there is a concrete bridge with the length of about 53 m between Sosterbekk station and Katterat station, as shown in Figure 7.5(a).

(a)

(b)
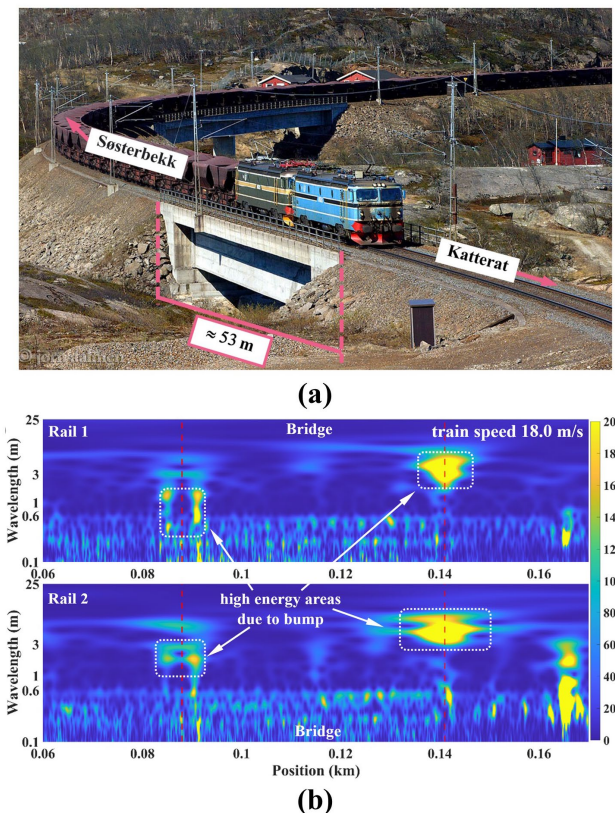
Figure 7.5: ABA measurement at a bridge in Norway
(source of aerial photos: https://www.arctictrains.com/Ofotbanen/i-DgW4F7N).

At the transition zones, there was differential settlement due to the large variation in track support stiffness. In Figure 7.5(b), at the abutments, as shown with the white dash box, high-energy areas with wavelengths about 1-10 m, are found due to the bumps caused by differential settlement. The sleeper interval-related patterns are still obvious but not so distinguishable from the patterns with shorter wavelengths, which is probably because of the short sleeper interval of 0.52 m, making the discrete rail support effect less pronounced.

7.4. CONCLUSIONS AND FUTURE WORK

In this chapter, using multi-ABA measurements for health condition monitoring of transition zones is introduced and showcased with measurements in the Netherlands, Sweden and Norway. It is found that different bridges and transition zones exhibit unique characteristics including dominant wavelengths and energy distribution. Based on these unique characteristics, the geometry and support conditions at different parts of a transition zone can be evaluated. Higher train speed makes the characteristics more pronounced. These results demonstrate that the multi-ABA measurement has the potential to evaluate the health conditions of different transition zones.

In the future, local dynamic tests and numerical studies can be conducted to further interpret the ABA measurement results thus to make the multi-ABA measurements more applicable for the health condition monitoring of railway transition zones.

BIBLIOGRAPHY

[1]   International Union of Railways (UIC), 2022 Global rail sustainability report, 2023.

[2]   N. Epicoco, M. Falagario, Decision support tools for developing sustainable transportation systems in the EU: a review of research needs, barriers, and trends, Research in Transportation Business & Management 43 (2022) 100819.

[3]   M. Dotoli, N. Epicoco, M. Falagario, C. Seatzu, B. Turchiano, A decision support system for optimizing operations at intermodal railroad terminals, IEEE Transactions on Systems, Man, and Cybernetics: Systems 47 (2017) 487–501.

[4]   International Union of Railways (UIC), Guidelines for the application of asset management in railway infrastructure organisations, 2010.

[5]   Platform of Rail Infrastructure Managers in Europe (PRIME), 2021 PRIME benchmarking report, 2021.

[6]   ProRail, Innovation call for dust-free tracks, Utrecht, 2022.

[7]   B. Indraratna, C. Rujikiatkamjorn, W. Salim, Advanced rail geotechnology–ballasted track, CRC press, 2023.

[8]   CEN, NEN-EN 13306:2019 - Maintenance - maintenance terminology, 2019.

[9]   CEN, NEN-EN 13848-5:2017 (E) - Railway applications - track - track geometry quality - part 5: geometric quality levels - plain line, switches and crossing, 2017.

[10]   B. Lichtberger, Track compendium, PMC Media House, 2011.

[11]   A. Lasisi, N. Attoh-Okine, Principal components analysis and track quality index: a machine learning approach, Transp Res Part C Emerg Technol 91 (2018) 230–248.

[12]   Z. Su, A. Jamshidi, A. Núñez, S. Baldi, B. De Schutter, Integrated condition-based track maintenance planning and crew scheduling of railway networks, Transportation Research Part C: Emerging Technologies 105 (2019) 359–384.

[13]   A. Núñez, A. Jamshidi, H. Wang, Pareto-based maintenance decisions for regional railways with uncertain weld conditions using the Hilbert spectrum of axle box acceleration, IEEE Transactions on Industrial Informatics 15 (2019) 1496–1507.

[14]   A. Jamshidi, S. Hajizadeh, Z. Su, M. Naeimi, A. Núñez, R. Dollevoet, B. De Schutter, Z. Li, A decision support approach for condition-based maintenance of rails based on big data analysis, Transportation Research Part C: Emerging Technologies 95 (2018) 185–206.

[15]   Z. Su, A. Jamshidi, A. Núñez, S. Baldi, B. De Schutter, Multi-level condition-based maintenance planning for railway infrastructures – a scenario-based chance-constrained approach, Transportation Research Part C: Emerging Technologies 84 (2017) 92–123.

[16] T.P. Carvalho, F.A.A.M.N. Soares, R. Vita, R. da P. Francisco, J.P. Basto, S.G.S. Alcalá, A systematic literature review of machine learning methods applied to predictive maintenance, Computers & Industrial Engineering 137 (2019) 106024.

[17] D. Li, J. Hyslip, T. Sussmann, S. Chrismer, Railway geotechnics, CRC Press, 2015.

[18] C. Esveld, Modern railway track, 2nd ed., MRT-productions, Zaltbommel, 2003.

[19] CEN, NEN-EN 13848-2:2020 (E) - Railway applications - track - track geometry quality - part 2: measuring systems - track recording vehicles, 2020.

[20] P. Wang, L. Wang, R. Chen, J. Xu, J. Xu, M. Gao, Overview and outlook on railway track stiffness measurement, Journal of Modern Transportation 24 (2016) 89–102.

[21] W. Powrie, A guide to track stiffness, University of Southampton Department of Civil & Enviromental Engineering, 2016.

[22] T. Dahlberg, Railway track settlements-a literature review, Report for the EU project SUPERTRACK - Linkoping University Sweden, 2003.

[23] C. Shen, R. Dollevoet, Z. Li, Fast and robust identification of railway track stiffness from simple field measurement, Mechanical Systems and Signal Processing 152 (2021) 107431.

[24] C. Shen, P. Zhang, R. Dollevoet, A. Zoeteman, Z. Li, Evaluating railway track stiffness using axle box accelerations: A digital twin approach, Mech Syst Signal Process 204 (2023) 110730.

[25] ProRail, Vervolgonderzoek naar stabiliteit spoordijken noodzakelijk, (2023). (accessed February 16, 2024).

[26] R. Sañudo, L. Dell'Olio, J.A. Casado, I.A. Carrascal, S. Diego, Track transitions in railways: a review, Construction and Building Materials 112 (2016) 140–157.

[27] A. Paixão, E. Fortunato, R. Calçada, Design and construction of backfills for railway track transition zones, Proceedings of the Institution of Mechanical Engineers, Part F: Journal of Rail and Rapid Transit 229 (2015) 58–70.

[28] A. Paixão, E. Fortunato, R. Calçada, A numerical study on the influence of backfill settlements in the train/track interaction at transition zones to railway bridges, Proceedings of the Institution of Mechanical Engineers, Part F: Journal of Rail and Rapid Transit 230 (2016) 866–878.

[29] J.Y. Zhu, D.J. Thompson, C.J.C. Jones, On the effect of unsupported sleepers on the dynamic behaviour of a railway track, Vehicle System Dynamics 49 (2011) 1389–1408.

[30] K.K. Ang, J. Dai, Response analysis of high-speed rail system accounting for abrupt change of foundation stiffness, Journal of Sound and Vibration 332 (2013) 2954–2970.

[31] Y. Bezin, S.D. Iwnicki, M. Cavalletti, E. de Vries, F. Shahzad, G. Evans, An investigation of sleeper voids using a flexible track model integrated with railway multi-body dynamics, Proceedings of the Institution of Mechanical Engineers, Part F: Journal of Rail and Rapid Transit 223 (2009) 597–607.

[32]   H. Wang, V. Markine, Dynamic behaviour of the track in transitions zones considering the differential settlement, Journal of Sound and Vibration 459 (2019) 114863.

[33]   T.D. Stark, S.T. Wilk, Root cause of differential movement at bridge transition zones, Proceedings of the Institution of Mechanical Engineers, Part F: Journal of Rail and Rapid Transit 230 (2016) 1257–1269.

[34]   C. Gallage, B. Dareeju, M. Dhanasekar, Track degradation a bridge transitions, in: K.P.P. Pathirana (Ed.), The 4th International Conference on Structural Engineering and Construction Management, Nethwin Printers (Pvt) Ltd, Sri Lanka, 2013: pp. 40–52.

[35]   S. Shao, D. Ji, Coupled discrete-finite element method for settlement analysis of transition zone between ballasted and ballastless track with polyurethane reinforcement based on computer aided technology, Journal of Physics: Conference Series 1574 (2020) 012007.

[36]   L. Auersch, Different types of continuous track irregularities as sources of train-induced ground vibration and the importance of the random variation of the track support, Applied Sciences 12 (2022) 1463.

[37]   S. Park, J.Y. Kim, J. Kim, S. Lee, K.-H. Cho, Analysis of dynamic characteristics of deformed concrete slab track on transition zone in high-speed train line according to train speeds, Applied Sciences 10 (2020) 7174.

[38]   P. Hölscher, P. Meijers, Literature study of knowledge and experience of transition zones, 2007.

[39]   Y. Shan, Y. Shu, S. Zhou, Finite-infinite element coupled analysis on the influence of material parameters on the dynamic properties of transition zones, Construction and Building Materials 148 (2017) 548–558.

[40]   A.B. Fărăgău, A. V. Metrikine, K.N. van Dalen, Transition radiation in a piecewise-linear and infinite one-dimensional structure–a Laplace transform method, Nonlinear Dynamics 98 (2019) 2435–2461.

[41]   H. Wang, V. Markine, Modelling of the long-term behaviour of transition zones: prediction of track settlement, Engineering Structures 156 (2018) 294–304.

[42]   Y. Shan, S. Zhou, H. Zhou, B. Wang, Z. Zhao, Y. Shu, Z. Yu, Iterative method for predicting uneven settlement caused by high-speed train loads in transition-zone subgrade, Transportation Research Record: Journal of the Transportation Research Board 2607 (2017) 7–14.

[43]   A. Paixão, J.N. Varandas, E. Fortunato, R. Calçada, Numerical simulations to improve the use of under sleeper pads at transition zones to railway bridges, Engineering Structures 164 (2018) 169–182.

[44]   I. Gallego Giner, A. López Pita, Numerical simulation of embankment—structure transition design, Proceedings of the Institution of Mechanical Engineers, Part F: Journal of Rail and Rapid Transit 223 (2009) 331–343.

[45]   J.N. Varandas, P. Hölscher, M.A.G. Silva, Dynamic behaviour of railway tracks on transitions zones, Computers & Structures 89 (2011) 1468–1479.

[46] Y. Shan, B. Albers, S.A. Savidis, Influence of different transition zones on the dynamic response of track–subgrade systems, Computers and Geotechnics 48 (2013) 21–28.

[47] B. Coelho, P. Hölscher, J. Priest, W. Powrie, F. Barends, An assessment of transition zone performance, Proceedings of the Institution of Mechanical Engineers, Part F: Journal of Rail and Rapid Transit 225 (2011) 129–139.

[48] C. Alves Ribeiro, R. Calçada, R. Delgado, Experimental assessment of the dynamic behaviour of the train-track system at a culvert transition zone, Engineering Structures 138 (2017) 215–228.

[49] Y. Çati, S. Gökçeli, Ö. Anil, C.S. Korkmaz, Experimental and numerical investigation of usp for optimization of transition zone of railway, Engineering Structures 209 (2020) 109971.

[50] J. Mottahed, J.A. Zakeri, S. Mohammadzadeh, A field investigation on the effects of using USPs in transition zone from ballasted track to bridges, International Journal of Civil Engineering 17 (2019) 1421–1431.

[51] J. Shi, M.P.N. Burrow, A.H. Chan, Y.J. Wang, Measurements and simulation of the dynamic responses of a bridge–embankment transition zone below a heavy haul railway line, Proceedings of the Institution of Mechanical Engineers, Part F: Journal of Rail and Rapid Transit 227 (2013) 254–268.

[52] H. Heydari-Noghabi, J. Zakeri, M. Esmaeili, J. Varandas, Field study using additional rails and an approach slab as a transition zone from slab track to the ballasted track, Proceedings of the Institution of Mechanical Engineers, Part F: Journal of Rail and Rapid Transit 232 (2018) 970–978.

[53] H. Boler, D. Mishra, E. Tutumluer, S. Chrismer, J.P. Hyslip, Stone blowing as a remedial measure to mitigate differential movement problems at railroad bridge approaches, Proceedings of the Institution of Mechanical Engineers, Part F: Journal of Rail and Rapid Transit 233 (2019) 63–72.

[54] A. Paixão, C. Alves Ribeiro, N. Pinto, E. Fortunato, R. Calçada, On the use of under sleeper pads in transition zones at railway underpasses: experimental field testing, Structure and Infrastructure Engineering 11 (2015) 112–128.

[55] C. Zhao, P. Wang, Q. Yi, D. Meng, Application of polyurethane polymer and assistant rails to settling the abnormal vehicle-track dynamic effects in transition zone between ballastless and ballasted track, Shock and Vibration 2015 (2015) 1–9.

[56] H. Heydari-Noghabi, J.N. Varandas, M. Esmaeili, J. Zakeri, Investigating the influence of auxiliary rails on dynamic behavior of railway transition zone by a 3D train-Track interaction model, Latin American Journal of Solids and Structures 14 (2017) 2000–2018.

[57] H. Wang, V. Markine, Corrective countermeasure for track transition zones in railways: adjustable fastener, Engineering Structures 169 (2018) 1–14.

[58] B. Indraratna, M. Babar Sajjad, T. Ngo, A. Gomes Correia, R. Kelly, Improved performance of ballasted tracks at transition zones: a review of experimental and modelling approaches, Transportation Geotechnics 21 (2019) 100260.

[59] W.-T. Hong, S.Y. Kim, S.J. Lee, J.-S. Lee, Strength and stiffness assessment of railway track substructures using crosshole-type dynamic cone penetrometer, Soil Dynamics and Earthquake Engineering 100 (2017) 88–97.

[60] Y.-H. Byun, J.H. Kim, J.-S. Lee, Cone penetrometer with a helical-type outer screw rod for evaluation of the subgrade condition, Journal of Transportation Engineering 139 (2013) 115–122.

[61] M.P.N. Burrow, A.H.C. Chan, A. Shein, Deflectometer-based analysis of ballasted railway tracks, Proceedings of the Institution of Civil Engineers - Geotechnical Engineering 160 (2007) 169–177.

[62] P. Haji Abdulrazagh, M.T. Hendry, Case study of use of falling weight deflectometer to investigate railway infrastructure constructed upon soft subgrades, Canadian Geotechnical Journal 53 (2016) 1991–2000.

[63] A.P. De Man, DYNATRACK: A survey of dynamic railway track properties and their quality, Delft University of Technology, 2002.

[64] V.J. Hodge, S. O'Keefe, M. Weeks, A. Moulds, Wireless sensor networks for condition monitoring in the railway industry: a survey, IEEE Transactions on Intelligent Transportation Systems 16 (2015) 1088–1106.

[65] D. Seneviratne, L. Ciani, M. Catelani, D. Galar, Smart maintenance and inspection of linear assets: an industry 4.0 approach, ACTA IMEKO 7 (2018) 50.

[66] M. Kans, D. Galar, A. Thaduri, Maintenance 4.0 in railway transportation industry, in: Lecture Notes in Mechanical Engineering, Springer International Publishing, Cham, 2016: pp. 317–331.

[67] R. Sañudo, I. Jardí, J.-C. Martínez, F.-J. Sánchez, M. Miranda, B. Alonso, L. Dell'Olio, J.-L. Moura, Monitoring track transition zones in railways, Sensors 22 (2021) 76.

[68] J.G. Rose, T.D. Stark, S.T. Wilk, M. Purcell, Design and monitoring of well-performing bridge transitions, in: 2015 Joint Rail Conference, American Society of Mechanical Engineers, 2015: p. V001T01A007.

[69] E. Tutumluer, T.D. Stark, D. Mishra, J.P. Hyslip, Investigation and mitigation of differential movement at railway transitions for US high speed passenger rail and joint passenger/freight corridors, in: 2012 Joint Rail Conference, American Society of Mechanical Engineers, 2012: pp. 75–84.

[70] D. Mishra, E. Tutumluer, H. Boler, J.P. Hyslip, T.R. Sussmann, Railroad track transitions with multidepth deflectometers and strain gauges, Transportation Research Record: Journal of the Transportation Research Board 2448 (2014) 105–114.

[71] H. Wang, M. Silvast, V. Markine, B. Wiljanen, Analysis of the dynamic wheel loads in railway transition zones considering the moisture condition of the ballast and subballast, Applied Sciences 7 (2017) 1208.

[72] H. Wang, V. Markine, X. Liu, Experimental analysis of railway track settlement in transition zones, Proceedings of the Institution of Mechanical Engineers, Part F: Journal of Rail and Rapid Transit 232 (2018) 1774–1789.

[73] E. Berggren, Railway track stiffness: dynamic measurements and evaluation for efficient maintenance, KTH Royal Institute of Technology, 2009.

[74] S. Farritor, Real-time measurement of track modulus from a moving car, 2006.

[75] S. Fallah Nafari, M. Gül, J.J.R. Cheng, Quantifying live bending moments in rail using train-mounted vertical track deflection measurements and track modulus estimations, Journal of Civil Structural Health Monitoring 7 (2017) 637–643.

[76] E.G. Berggren, A. Nissen, B.S. Paulsson, Track deflection and stiffness measurements from a track recording car, Proceedings of the Institution of Mechanical Engineers, Part F: Journal of Rail and Rapid Transit 228 (2014) 570–580.

[77] M. Hosseingholian, M. Froumentin, A. Robinet, Dynamic track modulus from measurement of track acceleration by portancemetre, in: 9th World Congress on Railway Research, 2011.

[78] X. Wei, F. Liu, L. Jia, Urban rail track condition monitoring based on in-service vehicle acceleration measurements, Measurement 80 (2016) 217–228.

[79] H. Tsunashima, R. Hirose, Condition monitoring of railway track from car-body vibration using time–frequency analysis, Vehicle System Dynamics 60 (2022) 1170–1187.

[80] P.F. Weston, C.S. Ling, C. Roberts, C.J. Goodman, P. Li, R.M. Goodall, Monitoring vertical track irregularity from in-service railway vehicles, Proceedings of the Institution of Mechanical Engineers, Part F: Journal of Rail and Rapid Transit 221 (2007) 75–88.

[81] P.F. Weston, C.S. Ling, C.J. Goodman, C. Roberts, P. Li, R.M. Goodall, Monitoring lateral track irregularity from in-service railway vehicles, Proceedings of the Institution of Mechanical Engineers, Part F: Journal of Rail and Rapid Transit 221 (2007) 89–100.

[82] I. La Paglia, M. Carnevale, R. Corradi, E. Di Gialleonardo, A. Facchinetti, S. Lisi, Condition monitoring of vertical track alignment by bogie acceleration measurements on commercial high-speed vehicles, Mech Syst Signal Process 186 (2023).

[83] J.S. Lee, S. Choi, S.-S. Kim, C. Park, Y.G. Kim, A mixed filtering approach for track condition monitoring using accelerometers on the axle box and bogie, IEEE Trans Instrum Meas 61 (2012) 749–758.

[84] S. Munoz, J. Ros, P. Urda, J.L. Escalona, Estimation of lateral track irregularity through Kalman filtering techniques, IEEE Access 9 (2021) 60010–60025.

[85] D. Cantero, B. Basu, Railway infrastructure damage detection using wavelet transformed acceleration response of traversing vehicle, Struct Control Health Monit 22 (2015) 62–70.

[86] G. Lederman, S. Chen, J.H. Garrett, J. Kovačević, H.Y. Noh, J. Bielak, Track monitoring from the dynamic response of a passing train: a sparse approach, Mech Syst Signal Process 90 (2017) 141–153.

[87]   G. Lederman, S. Chen, J. Garrett, J. Kovačević, H.Y. Noh, J. Bielak, Track-monitoring from the dynamic response of an operational train, Mech Syst Signal Process 87 (2017) 1–16.

[88]   A. Rodríguez, R. Sañudo, M. Miranda, A. Gómez, J. Benavente, Smartphones and tablets applications in railways, ride comfort and track quality. Transition zones analysis, Measurement 182 (2021) 109644.

[89]   CEN, NEN-EN 13848-1:2019 (E) - Railway applications - track - track geometry quality - part 1: characterization of track geometry, 2019.

[90]   CEN, NEN-EN 13848-6:2014 (E) - Railway applications - track - track geometry quality - part 6: characterization of track geometry quality, 2014.

[91]   J. Sadeghi, Development of railway track geometry indexes based on statistical distribution of geometry data, Journal of Transportation Engineering 136 (2010) 693–700.

[92]   M. Anderson, Strategic planning of track maintenance - state of the art, 2002.

[93]   R.-K. Liu, P. Xu, Z.-Z. Sun, C. Zou, Q.-X. Sun, Establishment of track quality index standard recommendations for Beijing metro, Discrete Dyn Nat Soc 2015 (2015) 1–9.

[94]   W. Ebersohn, Implementing a railway infrastructure maintenance system, in: Conference on Railway Engineering Proceedings: Engineering Innovation for a Competitive Edge, Central Queensland University, 1998: pp. 395–402.

[95]   Y.-J. Zhang, M. El-Sibaie, S. Lee, FRA track quality indices and distribution characteristics, in: AREMA Annual Conference, 2004.

[96]   T.-H. Yan, F. Corman, Assessing and extending track quality index for novel measurement techniques in railway systems, Transportation Research Record: Journal of the Transportation Research Board 2674 (2020) 24–36.

[97]   S. Offenbacher, J. Neuhold, P. Veit, M. Landgraf, Analyzing major track quality indices and introducing a universally applicable TQI, Applied Sciences 10 (2020) 8490.

[98]   F. Peng, Scheduling of track inspection and maintenance activities in railroad network, University of Illinois at Urbana-Champaign, 2011.

[99]   C. Hu, X. Liu, Modeling track geometry degradation using support vector machine technique, in: ASME/IEEE Joint Rail Conference, American Society of Mechanical Engineers, 2016: p. V001T01A011.

[100] A. Lasisi, N. Attoh-Okine, Hybrid rail track quality analysis using nonlinear dimension reduction technique with machine learning, Canadian Journal of Civil Engineering 48 (2021) 1713–1723.

[101] M. Movaghar, S. Mohammadzadeh, Intelligent index for railway track quality evaluation based on Bayesian approaches, Structure and Infrastructure Engineering 16 (2020) 968–986.

[102] D. Li, A. Meddah, K. Hass, S. Kalay, Relating track geometry to vehicle performance using neural network approach, Proc Inst Mech Eng F J Rail Rapid Transit 220 (2006) 273–281.

[103] L. Xu, W. Zhai, A novel model for determining the amplitude-wavelength limits of track irregularities accompanied by a reliability assessment in railway vehicle-track dynamics, Mech Syst Signal Process 86 (2017) 260–277.

[104] M. Molodova, Z. Li, R. Dollevoet, Axle box acceleration: measurement and simulation for detection of short track defects, Wear 271 (2011) 349–356.

[105] M. Molodova, Z. Li, A. Núñez, R. Dollevoet, Automatic detection of squats in railway infrastructure, IEEE Transactions on Intelligent Transportation Systems 15 (2014) 1980–1990.

[106] P. Salvador, V. Naranjo, R. Insa, P. Teixeira, Axlebox accelerations: their acquisition and time–frequency characterisation for railway track monitoring purposes, Measurement 82 (2016) 301–312.

[107] A. Chudzikiewicz, R. Bogacz, M. Kostrzewski, R. Konowrocki, Condition monitoring of railway track systems by using acceleration signals on wheelset axle-boxes, Transport 33 (2017) 555–566.

[108] B. An, P. Wang, J. Xu, R. Chen, D. Cui, Observation and simulation of axle box acceleration in the presence of rail weld in high-speed railway, Applied Sciences 7 (2017) 1259.

[109] H. Tanaka, A. Furukawa, Management method for large wheel loads and lateral forces using axle-box acceleration and track irregularity, Quarterly Report of RTRI 50 (2009) 116–122.

[110] Z. Li, M. Molodova, A. Núñez, R. Dollevoet, Improvements in axle box acceleration measurements for the detection of light squats in railway infrastructure, IEEE Transactions on Industrial Electronics 62 (2015) 4385–4397.

[111] S. Unsiwilai, L. Wang, A. Núñez, Z. Li, Multiple-axle box acceleration measurements at railway transition zones, Measurement 213 (2023) 112688.

[112] M. Molodova, M. Oregui, A. Núñez, Z. Li, R. Dollevoet, Health condition monitoring of insulated joints based on axle box acceleration measurements, Eng Struct 123 (2016) 225–235.

[113] Z. Wei, A. Núñez, Z. Li, R. Dollevoet, Evaluating degradation at railway crossings using axle box acceleration measurements, Sensors 17 (2017) 2236.

[114] M. Oregui, S. Li, A. Núñez, Z. Li, R. Carroll, R. Dollevoet, Monitoring bolt tightness of rail joints using axle box acceleration measurements, Structural Control and Health Monitoring 24 (2017) e1848.

[115] C. Ngamkhanong, K. Goto, S. Kaewunruen, Dynamic responses of railway ballasted track considering rail pad deterioration, Journal of Physics: Conference Series 1106 (2018) 012006.

[116] L. Auersch, Vehicle-track-soil interaction and train-induced ground vibration – theory and measurements in Germany, Switzerland and France, Journal of Physics: Conference Series 1264 (2019) 012034.

[117] S. Kaewunruen, A.M. Remennikov, Field trials for dynamic characteristics of railway track and its components using impact excitation technique, NDT & E International 40 (2007) 510–519.

[118] J.C.O. Nielsen, E.G. Berggren, A. Hammar, F. Jansson, R. Bolmsvik, Degradation of railway track geometry – correlation between track stiffness gradient and differential settlement, Proc Inst Mech Eng F J Rail Rapid Transit 234 (2020) 108–119.

[119] K. Chen, B. Lechner, DESTination RAIL – decision support tool for rail infrastructure managers: D2.4 report on assessment of track, 2017.

[120] C. Charoenwong, D.P. Connolly, P.K. Woodward, P. Galvín, P. Alves Costa, Analytical forecasting of long-term railway track settlement, Computers and Geotechnics 143 (2022) 104601.

[121] H. Wang, L. Chang, V. Markine, Structural Health Monitoring of Railway Transition Zones Using Satellite Radar Data, Sensors 18 (2018) 413.

[122] H. Wang, J. Berkers, N. van den Hurk, N.F. Layegh, Study of loaded versus unloaded measurements in railway track inspection, Measurement 169 (2021) 108556.

[123] Z. Li, M. Molodova, Method and instrumentation for detection of rail defects, in particular rail top defects, WO 2011019273 (A1), 2011.

[124] E. Arlaud, S. Costa D'Aguiar, E. Balmes, Receptance of railway tracks at low frequency: numerical and experimental approaches, Transportation Geotechnics 9 (2016) 1–16.

[125] L. Wang, P. Wang, K. Wei, R. Dollevoet, Z. Li, Ground vibration induced by high speed trains on an embankment with pile-board foundation: modelling and validation with in situ tests, Transportation Geotechnics 34 (2022) 100734.

[126] E.G. Berggren, A.M. Kaynia, B. Dehlbom, Identification of substructure properties of railway tracks by dynamic stiffness measurements and simulations, J Sound Vib 329 (2010) 3999–4016.

[127] C. Torrence, G.P. Compo, A practical guide to wavelet analysis, Bull Am Meteorol Soc 79 (1998) 61–78.

[128] D. Li, D. Davis, Transition of railroad bridge approaches, Journal of Geotechnical and Geoenvironmental Engineering 131 (2005) 1392–1398.

[129] M. Audley, J.D. Andrews, The effects of tamping on railway track geometry degradation, Proceedings of the Institution of Mechanical Engineers, Part F: Journal of Rail and Rapid Transit 227 (2013) 376–391.

[130] A. Paixão, E. Fortunato, R. Calçada, A contribution for integrated analysis of railway track performance at transition zones and other discontinuities, Construction and Building Materials 111 (2016) 699–709.

[131]   L. Auersch, Excitation of ground vibration due to the passage of trains over a track with trackbed irregularities and a varying support stiffness, Vehicle System Dynamics 53 (2015) 1–29.

[132]   L. Lazarević, D. Vučković, M. Vilotijević, Z. Popović, Application of seismic tomography for assessment of the railway substructure condition, Structural Health Monitoring 18 (2019) 792–805.

[133]   J. Náprstek, L. Frýba, Stochastic modelling of track and its substructure, Vehicle System Dynamics 24 (1995) 297–310.

[134]   M. Ma, M. Li, X. Qu, H. Zhang, Effect of passing metro trains on uncertainty of vibration source intensity: monitoring tests, Measurement 193 (2022) 110992.

[135]   M. Oregui, Z. Li, R. Dollevoet, Identification of characteristic frequencies of damaged railway tracks using field hammer test measurements, Mechanical Systems and Signal Processing 54–55 (2015) 224–242.

[136]   M. Oregui, M. Molodova, A. Núñez, R. Dollevoet, Z. Li, Experimental investigation into the condition of insulated rail joints by impact excitation, Experimental Mechanics 55 (2015) 1597–1612.

[137]   Z. Xiong, J. Liu, P. Wang, G. Liu, J. Xiao, S. Yu, Field dynamic performance testing and analysis of polyurethane track and ballasted track in a high-speed railway, Journal of Civil Structural Health Monitoring 11 (2021) 867–877.

[138]   M. Oregui, Z. Li, R. Dollevoet, An investigation into the modeling of railway fastening, International Journal of Mechanical Sciences 92 (2015) 1–11.

[139]   K. Knothe, Y. Wu, Receptance behaviour of railway track and subgrade, Archive of Applied Mechanics 68 (1998) 457–470.

[140]   Z. Wei, A. Boogaard, A. Núñez, Z. Li, R. Dollevoet, An integrated approach for characterizing the dynamic behavior of the wheel–rail interaction at crossings, IEEE Transactions on Instrumentation and Measurement 67 (2018) 2332–2344.

[141]   K. Knothe, S.L. Grassie, Modelling of railway track and vehicle/track interaction at high frequencies, Vehicle System Dynamics 22 (1993) 209–262.

[142]   B.J. Schwarz, M.H. Richardson, Introduction to operating deflection shapes, Citeseer, 1999.

[143]   A. López-Pita, P.F. Teixeira, C. Casas, L. Ubalde, F. Robusté, Evolution of track geometric quality in high-speed lines: ten years experience of the Madrid-Seville line, Proc Inst Mech Eng F J Rail Rapid Transit 221 (2007) 147–155.

[144]   M.J. Cano, P.M. Fernández, R.I. Franco, Measuring track vertical stiffness through dynamic monitoring, Proceedings of the Institution of Civil Engineers - Transport 169 (2016) 3–11.

[145]   ProRail, Instandhoudingsspecificatie - Spoor - Deel 1: Onderhoudswaarden, Interventiewaarden, Onmiddellijke actiewaarden, 2021.

[146] S. Unsiwilai, C. Shen, Y. Zeng, L. Wang, A. Núñez, Z. Li, Vertical dynamic measurements of a railway transition zone: a case study in Sweden, J Civ Struct Health Monit 14 (2024) 979–996.

[147] The MathWork Inc., resample, (2023). (accessed November 30, 2023).

[148] I. Soleimanmeigouni, A. Ahmadi, A. Nissen, X. Xiao, Prediction of railway track geometry defects: a case study, Structure and Infrastructure Engineering 16 (2020) 987–1001.

[149] S. Unsiwilai, W. Phusakulkajorn, C. Shen, A. Zoeteman, R. Dollevoet, A. Núñez, Z. Li, Enhanced vertical railway track quality index with dynamic responses from moving trains, (2024).

[150] The MathWork Inc., wavedec, (2023). (accessed November 30, 2023).

ACKNOWLEDGMENTS

My Ph.D. journey has been much like tasting a complex beer, with each phase offering a different flavor. It was sometimes smooth and rewarding, like a refreshing sip. Other times, it was bitter and challenging. Without the support of many people, this journey would not have been possible. I am deeply grateful for their encouragement and guidance. While I intend to thank everyone personally, I apologize for any omissions due to space constraints.

First and foremost, I would like to express my deep gratitude to my promotor, Prof. Dr. Zili Li. Meeting him in Thailand in February 2018 and sharing my interest in working with him was one of the most significant opportunities of my life. My Ph.D. journey officially began in September 2018, and since then, his guidance, suggestions, and unwavering support have been invaluable. Despite managing numerous projects, his tireless dedication to students and colleagues is admirable. He demonstrates the high standards of professionalism expected from a world-class professor and remains a constant source of inspiration.

Next, I would like to express my sincere gratitude to my co-promotor and daily supervisor, Assoc. Prof. Dr. Alfredo Núñez Vicencio. There were moments throughout the journey when I questioned my abilities and suitability for this degree. I can confidently say that this accomplishment would not have been possible without his scientific and emotional support. Our frequent communications, often extending beyond academia, revealed his kindness and inspired me to become more supportive. Moreover, he kindly involved me in educational and project-related activities, particularly Europe's Rail Flagship Project IAM4RAIL, providing invaluable experiences I will carry with me when I return to Thailand.

My sincere thanks go to the committee members: Prof. Dr. Rolf Dollevoet, Prof. Dr. Bart De Schutter, Prof. Dr. Doris Sáez Hueichapan, Prof. Dr. Igor Škrjanc, and Dr. Arjen Zoeteman for dedicating their time and effort to reviewing my dissertation. Their critical feedback has significantly enhanced the quality of this

DISCLAIMER

CURRICULUM VITAE

Siwarak Unsiwilai

Feb. 4, 1988	**Born in Khon Kaen, Thailand**

EDUCATION

Sep. 2018 – Jun. 2024	**Ph.D. Student**
	Section of Railway Engineering
	Delft University of Technology, Delft, The Netherlands
May 2010 – Oct. 2013	**Master of Engineering**
	Department of Civil Engineering
	Chulalongkorn University, Bangkok, Thailand
May 2006 – Mar. 2010	**Bachelor of Engineering**
	Department of Civil Engineering
	Chulalongkorn University, Bangkok, Thailand

EMPLOYMENT

Jun. 2024 – Present	**Postdoctoral Researcher**
	Section of Railway Engineering
	Delft University of Technology, Delft, The Netherlands
Nov. 2013 – Aug. 2018	**Researcher**
	Center of Excellence in Infrastructure Management
	Faculty of Engineering
	Chulalongkorn University, Bangkok, Thailand

LIST OF PUBLICATIONS

JOURNAL PAPERS

1. **S. Unsiwilai**, L. Wang, A. Núñez, Z. Li, Multiple-axle box acceleration measurements at railway transition zones, Measurement. 213 (2023) 112688.

2. **S. Unsiwilai**, C. Shen, Y. Zeng, L. Wang, A. Núñez, Z. Li, Vertical dynamic measurements of a railway transition zone: a case study in Sweden, J. Civ. Struct. Heal. Monit. (2024).

3. **S. Unsiwilai**, W. Phusakulkajorn, C. Shen, A. Zoeteman, R. Dollevoet, A. Núñez, Z. Li, Enhanced vertical railway track quality index with dynamic responses from moving trains. (2024). Under review.

4. W. Phusakulkajorn, **S. Unsiwilai**, L Chang, A. Núñez, Z. Li, A hybrid neural model approach for health assessment of railway transition zones with multiple data sources. (2024). Under review.

CONFERENCE PAPERS

1. L. Wang, **S. Unsiwilai**, Y. Zeng, C. Shen, J. Hendriks, J Moraal, A. Zoeteman, A. Núñez, R. Dollevoet, and Z. Li, Condition monitoring of railway transition zones using acceleration measurements on multiple axle boxes: Case studies in the Netherlands, Sweden, and Norway, in: the 10th Transport Research Arena Conference (TRA2024), 15-18 April 2024, Dublin, Ireland.

2. W. Phusakulkajorn, J. Hendriks, J. Moraal, C. Shen, Y. Zeng, **S. Unsiwilai**, B. Bogojevic, M. Asplund, A. Zoeteman, A. Núñez, R. Dollevoet, and Z. Li, Detection of Rail Surface Defects based on Axle Box Acceleration Measurements: A Measurement Campaign in Sweden, in: the 10th Transport Research Arena Conference (TRA2024), 15-18 April 2024, Dublin, Ireland.

3. L. Wang, C. Shen, **S. Unsiwilai**, W. Phusakulkajorn, Y. Zeng, J. Hendriks, J Moraal, A. Núñez, A. Zoeteman, R. Dollevoet, and Z. Li, Sleeper support condition monitoring using axle box acceleration measurement, in: the 3rd International Conference on Rail Transportation (ICRT2024), 7-9 August 2024, Shanghai, China.